WAVE ENERGY RESOURCE CHARACTERIZATION AND CLASSIFICATION FOR THE UNITED STATES
&
NUMERICAL SIMULATION OF COASTAL CIRCULATION NEAR POINT SAL, CALIFORNIA

A Dissertation
Presented to
The Academic Faculty

by

Seongho Ahn

In Partial Fulfillment
of the Requirements for the Degree
Doctor of Philosophy in the
School of Civil and Environmental Engineering

Georgia Institute of Technology

August 2019

WAVE ENERGY RESOURCE CHARACTERIZATION AND CLASSIFICATION FOR THE UNITED STATES
&
NUMERICAL SIMULATION OF COASTAL CIRCULATION NEAR POINT SAL, CALIFORNIA

Approved by:

Dr. Kevin A. Haas, Advisor
School of Civil and Environmental Engineering
Georgia Institute of Technology

Dr. Emanuele Di Lorenzo
School of Earth and Atmospheric Sciences
Georgia Institute of Technology

Dr. Hermann M. Fritz
School of Civil and Environmental Engineering
Georgia Institute of Technology

Dr. Vincent S. Neary
Water Power Technologies
Sandia National Laboratories

Dr. Donald R. Webster
School of Civil and Environmental Engineering
Georgia Institute of Technology

Date Approved: July 22, 2019

ACKNOWLEDGEMENTS

I would like to express my deepest gratitude to my advisor Dr. Kevin Haas, for providing me with research opportunities and his enlightening guidance throughout my time at Georgia Tech. I sincerely thank Dr. Hermann Fritz for educating me in coastal engineering and serving on my thesis committee. I would like to thank Dr. Donald Webster for educating me in fluid mechanics and serving on my thesis committee. I also wish to thank Dr. Di Lorenzo for enriching my knowledge in oceanography and serving on my thesis committee. I am grateful for the invaluable time Dr. Vincent Neary has invested in advising my wave energy research and serving on my thesis committee.

I want to thank Sandia National Laboratories and Office of Naval Research providing financial support and invaluable research feedback. I am deeply thankful for the support from my colleagues at water resource group from Georgia Tech: Tongtong Xu, Yibin Liu, Alexandra Muscalus, and Martin Jang and many others. I also want to thank all Korean friends and all the memories from Georgia Tech.

I want to thank my father (Jaein An), mother (Dongweol Seo), father in law (Byungsun Jo), mother in law (Sunyung Jung), sister in law (Ahra Jo), and brother in law (Daeseung Jo).

Last but most, I want to thank Ahreum and Hojin who mean more to me than anything in the world. Without their unconditional support and endless love, I would not be here.

TABLE OF CONTENTS

ACKNOWLEDGEMENTS iii

LIST OF TABLES vi

LIST OF FIGURES vii

SUMMARY xii

CHAPTER 1. INTRODUCTION 1
1.1 Wave energy resource 1
1.2 Coastal circulation 4

CHAPTER 2. LITERATURE REVIEW 7
2.1 Wave energy resource assessment 7
2.2 Wave energy resource characterization 10
2.3 Wave energy resource classification 13
2.4 Coastal circulation 15
2.5 Motivation for present study 22

CHAPTER 3. WAVE POWER 25
3.1 Wave data 25
3.2 Validation of data 27
3.3 Wave power calculation 32
3.3.1 Annual Available Energy (AAE) 36
3.4 Wave power along the US coastal waters 37

CHAPTER 4. WAVE ENERGY RESOURCE PARAMETERS 41
4.1 Frequency dependence 42
4.1.1 AAE-weighted period, $TAAE$ 42
4.1.2 AAE Spectral width, ϵAAE 44
4.2 Directional variability 45
4.2.1 Direction of the maximum directionally resolved AAE, αmax 46
4.2.2 AAE directionality coefficient, $d\alpha$ 48
4.3 Temporal variability 49
4.3.1 AAE long-term linear trend, $SAAE$ 50
4.3.2 Inter-annual variability, ti 53
4.3.3 Seasonal variability, ts 55
4.4 Summary 57

CHAPTER 5. WAVE ENERGY RESOURCE ASSESSMENTS AND CHARACTERISTICS 59
5.1 Delineating US wave energy regions 60
5.2 Regional wave energy resource characteristics 64
5.2.1 Region 1- Bering Sea 65

5.2.2 Region 2- Aleutian Trench and Gulf of Alaska 69
5.2.3 Region 3- Pacific Northwest Coast 71
5.2.4 Region 4- California Coast 73
5.2.5 Region 5- Hawaiian - northern coast 76
5.2.6 Region 6- Hawaiian - southern coast 79
5.2.7 Region 7- Gulf of Mexico - western & central coast 82
5.2.8 Region 8- Gulf of Mexico - eastern coast 84
5.2.9 Region 9- Atlantic - South & Mid coast 86
5.2.10 Region 10- Atlantic - North coast 89
5.2.11 Region 11- Puerto Rico 92
5.3 Summary 94

CHAPTER 6. WAVE ENERGY RESOURCE CLASSIFICATION 97
6.1 Definition of classes 98
6.1.1 Peak period band classes 98
6.1.2 Wave power classes 99
6.1.3 Wave power classification matrices 100
6.2 Wave power and period classes for US coastal waters 101
6.3 Classification systems for US coastal waters 106
6.4 Summary 110

CHAPTER 7. NUMERICAL SIMULATION OF COASTAL CIRCULATION 112
7.1 Method 112
7.1.1 Numerical model 114
7.1.2 Model validation 116
7.1.3 Coastal upwelling detection 117
7.2 Circulation near Pt. Sal during upwelling favorable conditions 121
7.2.1 Lagrangian transports 125
7.2.2 Surface currents and stratification 129
7.3 Circulation momentum analysis 132
7.3.1 Forcing mechanisms 132
7.3.2 Momentum balance 136
7.3.3 Dominant forcing mechanisms 142
7.4 Comparison with circulation in July 2017 144
7.5 Summary 148

CHAPTER 8. CONCLUSION 152

APPENDIX A. Conversion factors for wave energy calculation 158

REFERENCES 165

LIST OF TABLES

Table 2.1 IEC Wave Resource Parameters [3]. 11

Table 3.1 List of wave measurement buoys providing spectral records for the US coast 28

Table 3.2 Maximum acceptable error of key validation parameters for the reconnaissance class of a resource assessment project [3]. 29

Table 3.3 Validation results between the buoys and WWIII model data. 31

Table 5.1 Summary of key features for each energy region. 64

Table 5.2 Summary of the characteristics of the energetic wave systems at each region. Bold indicates the most energetic system. 96

Table 6.1 Definition of peak period and frequency band classes. 98

Table 6.2 Definition of power classes. 99

Table 6.3 Power classification matrix for US coastal waters. 101

Table 6.4 Percent contribution of classification system 1 (total wave power class). 109

Table 6.5 Percent contribution of classification system 2 (dominant partitioned wave power class). 109

Table 7.1 ROMS model configurations. The √ symbol means the model is performed. 114

Table 7.2 The mechanisms influencing the circulation near Pt. Sal during the selected period. Abbreviations indicate circulation (Cir.), Coriolis force (C), pressure gradient force (P), vertical mixing (V). The signs indicate directions of the circulation and each momentum term where “+/-” is toward north/south and onshore/offshore in alongshore and cross-shore direction, respectively. The color indentifies the forcing source (red), necessary condition (blue), and resultant circulation (black). 135

LIST OF FIGURES

Figure 2.1 Location of Point Sal. The color indicates water depth. 16

Figure 3.1 Geographic distribution of spectral partition data for the US coastal waters (77,346 sites). Colors indicate water depth (m). 26

Figure 3.2 Location of twenty-six buoys and its station number. Colors represent the water depth (m). 29

Figure 3.3 Sample calculation of wave power of the 30-year average for an example site (Hawaii, 22.7N 160.5W): (a) mean wave power, $\mathrm{J_m(T_b, \theta_b)}$. Color and the number represent wave power of the cell in kW/m. (b) wave power as a function of the peak period, $\mathrm{J_m(T_b)}$. (c) wave power as a function of wave direction, $\mathrm{J_m(\theta_b)}$. 36

Figure 3.4 Regional percent contribution of wave power: (a) Alaska, (b) West Coast, (c) Hawaii, (d) East Coast, (e) Gulf Coast. Percent contributions of the 30-year averaged wave power for sea states in all US coastal waters; (left) percent contribution of the wave energy in terms of peak period partition and wave direction having a resolution of 1s and 10o, respectively. Colors indicate contributions to the total energy in %, (middle) plot (left) in polar coordinates, (right) percent contribution of the wave energy in terms of AAE (left y-axis) and wave power (right y-axis) and peak period partition. The resolution of the AAE and wave power is 5 MWh/m and 0.57 kW/m, respectively. The red line indicates averaged wave power as a function of peak period partition. 39

Figure 3.5 Geographic distribution of total AAE in MWh/m. 40

Figure 4.1 Geographic distribution of the AAE-weighted period, $\mathrm{T_{AAE}}$ in seconds, Eq. (4.1). 43

Figure 4.2 Geographic distribution of AAE spectral width, $\mathrm{\epsilon_{AAE}}$ representing the standard deviation of $\mathrm{AAE(T_b)}$ normalized by the total AAE, Eq. (4.2). 44

Figure 4.3 Geographic distribution of the direction of the maximum directionally resolved AAE, $\mathrm{\alpha_{max}}$, Eq. (4.4). The color indicates the clockwise direction from the North including both upstream and downstream direction. 47

Figure 4.4 Geographic distribution of the AAE directionality coefficient, $\mathrm{d_\alpha}$, Eq. (4.5). 48

Figure 4.5 Geographic distribution of the long-term linear trends in AAE in percent per year. Eq. (4.6). Colors represent the $\mathrm{S_{AAE}}$ index. 52

Figure 4.6 The averaged inter-annual AAE (solid line) at sample regions, California Coast (blue), Northern Atlantic Coast (red), Central Gulf of Mexico (black), and linear trend (dash line) over the 30-year period. 52

Figure 4.7 Geographic distribution of the inter-annual variability of AAE, Eq. (4.7). Colors represent the $\mathrm{t_i}$ index. 54

Figure 4.8 Geographic distribution of the monthly variability of AAE. Eq. (4.8). Colors represent the $\mathrm{t_s}$ index. 56

Figure 5.1 Eleven energy regions along the US coastal waters. 61

Figure 5.2 Averaged parameters across all locations within each region. (a) Total AAE (left y-axis) and directionality coefficient, d_α (right y-axis). (b) AAE-weighted period, $\mathrm{T}_{\mathrm{AAE}}$, (left y-axis) and spectral width, ϵ_{AAE} (right y-axis). (c) Seasonal variability, t_s (left y-axis) and inter-annual variability, t_i (right y-axis). 63

Figure 5.3 [Region 1 - Bering Sea] Averaged joint distributions, $\mathrm{AAE}(\mathrm{T}_\mathrm{b}, \theta_\mathrm{b})$ (top, left), $\mathrm{AAE}(\mathrm{T}_\mathrm{b}, \mathrm{M})$ (top, right), $\mathrm{AAE}(\mathrm{M}, \theta_\mathrm{b})$ (bottom, left), and averaged marginal distributions, $\mathrm{AAE}(\mathrm{T}_\mathrm{b})$, $\mathrm{AAE}(\theta_\mathrm{b})$, $\mathrm{AAE}(\mathrm{M})$, with corresponding resource parameters, d_α (red line), t_s (green line), ϵ_{AAE} (blue line), and geographical distribution of the total AAE (bottom, right). Resolutions of T_b, θ_b, and M distributions are 1s, 20° clockwise from the true north and month, respectively. The numerals and colors in the joint and marginal distributions indicate the averaged AAE within particular wave systems, peak period, direction, and month. The arrows in the geographical distribution show energetic wave systems indicating the direction, peak period (numeral) and season (red: summer, blue: winter, grey: all year round) of each system. The arrow with a bold edge indicates the most energetic wave system. The average of total AAE and d_α, t_s, ϵ_{AAE} of the total AAE is also shown in the geographical distribution. 68

Figure 5.4 [Region 2 - Aleutian Trench and Gulf of Alaska] The detailed descriptions are identical to Figure 5.3. 69

Figure 5.5 [Region 3 - Pacific Northwest Coast] The detailed descriptions are identical to Figure 5.3. 73

Figure 5.6 [Region 4 - California Coast] The detailed descriptions are identical to Figure 5.3. 75

Figure 5.7 [Region 5 - Hawaiian - northern coast] The detailed descriptions are identical to Figure 5.3. 78

Figure 5.8 [Region 6 - Hawaiian - southern coast] The detailed descriptions are identical to Figure 5.3. 81

Figure 5.9 [Region 7 - Gulf of Mexico - western & central coast] The detailed descriptions are identical to Figure 5.3. 83

Figure 5.10 [Region 8 - Gulf of Mexico - eastern coast] The detailed descriptions are identical to Figure 5.3. 86

Figure 5.11 [Region 9 - Atlantic - South & Mid coast] The detailed descriptions are identical to Figure 5.3. 88

Figure 5.12 [Region 10 - Atlantic - North coast] The detailed descriptions are identical to Figure 5.3. 91

Figure 5.13 [Region 11 - Puerto Rico] The detailed descriptions are identical to Figure 5.3. 94

Figure 6.1 Example of splitting wave power distribution into different peak period bands for a particular location. 98

Figure 6.2 Definition of wave energy classes. The values correspond to Figure 6.1. 100

Figure 6.3 (a) Geographical distribution of the total wave power, (b) Power class based on the total wave power. 102

Figure 6.4 (left) Geographical distribution of wave power within each period band, (right) Geographical distribution of power classes based on wave power within each period: (a) band 1 constrained by period 0-7s, (b) band 2 constrained by period 7-10s, (c) band 3 constrained by period larger than 10s. 103

Figure 6.5 Total wave power scatter plots as a function of AAE-weighted period, T_{AAE} : (a) total US coastal waters, (b) Alaska Coast, (c) West Coast of US, (d) Hawaii Coast, (e) Gulf Coast, (f) East Coast of US. Dash line defines power classes and color indicate the dominant period band having the largest energy. 105

Figure 6.6 Geographical distribution of classification system 1. The face color indicates the class of total wave power and edge color indicates the class of predominant period band. 107

Figure 6.7 Geographical distribution of classification system 2. The face color indicates the class of partitioned wave power in the predominant peak period band and edge color indicates the class of predominant period band. 108

Figure 7.1 Grids used for simulations with three levels of successive one-way nesting from (a) L0 grid (dx = 3km), L1 grid (dx = 1km), (b) L2 grid (546X386, dx=600m), L3 grid (857X732, dx=120m), L4 grid (382X772, dx=40m). The color indicates the water depth. 113

Figure 7.2 Hourly averaged time series (GMT) of 46011 buoy records (black) and COAMPS model results (blue) interpolated to the buoy location during June- July 2015. NDBC 46011 buoy location is indicated with a yellow circle in Figure 7.1. 116

Figure 7.3 (a) Depth-averaged U-velocity (solid-line) and V-velocity (dash-line) from the ADCP measurement (black) and model (red). Vertical structures of temperature from a thermistor (b) and model (c). 117

Figure 7.4 Comparisons the two models, including wind stresses and excluding wind stresses, at 80% bathymetric-following depth on 15 July 2015, 05:30 (GMT): (a, d) Temperature and Salinity modeled with wind stresses, respectively. (b, e) Temperature and Salinity modeled without wind stresses, respectively. (e, f) Temperature and Salinity differences between the two models, respectively. The vectors in (a,b,d,e) are the current velocity at 80% bathymetric-following depth. 119

Figure 7.5 Time evolutions of the 15 sections-averaged $\Delta T_{0.8}$ (solid-line, left-axis) and $\Delta S_{0.8}$ (dash-line, right-axis) anomaly during June-July 2015. The $\Delta T_{0.8}$ and $\Delta S_{0.8}$ means temperature and salinity difference between the two models at 80% bathymetry-fallowing water depth, respectively. Vectors indicate wind records at NDBC 46011 buoy. Blue dash-line is a time of the selected coastal 120 upwelling. Boxes spanning 36 hours highlight the upwelling (blue) and relaxation (red) period.

Figure 7.6 SST (color) and depth-averaged current velocity (vector with a 2km interval) snapshot on 15 July 2015, 05:30 (GMT) from the 120m grid model. 122

Figure 7.7 Snapshots of the current velocity, temperature and salinity fields near Pt. Sal on 15 July 2015, 05:30 (GMT) from the 40m grid model: (a) SST and depth-averaged current velocity vectors. Section profiles at the north boundary (b), west boundary (c) and south boundary (d). In the section profiles, solid-line is the isothermal, dash-line is the isohaline and color indicates northward(positive)-velocity component in (b, d) and eastward(positive)-velocity component in (c), respectively. Vertical profiles at points A and B shown in (a) are described in Figure 7.8. 123

Figure 7.8 Vertical profiles of the current velocity, temperature, and salinity at the Point A (solid-line) and B (dash-line) on 15 July 2015, 05:30 (GMT) from the 40m grid model: (a) east-westward-velocity component, (b) north-south-velocity component, (c) Salinity, (d) Temperature. The locations of the points are shown in Figure 7.7. 124

Figure 7.9 Particle trajectories during the 2015 circulation (36 hours from 14 July, 15:30 to 16 July 03:30, GMT). (a) Locations of the 15 sections (red lines). The color indicates water depth. (b-q) The trajectories initiated at 80% bathymetry-fallowing depth along the 15 sections. Upwelling is marked with blue trajectories. 126

Figure 7.10 (a) Geographical distributions of particle trajectories shown in Figure 7.9. Upwelling is marked with yellow trajectories (blue in Figure 7.9). The color indicates 36 hours (trajectory period) averaged $\Delta T_{0.8}$ anomaly. (b) Geographical distributions of the initial (empty circles) and turning (filled circles) positions of the upwelling trajectories. The color indicates 36 hours averaged $\Delta S_{0.8}$ anomaly. 127

Figure 7.11 (a) 36 hours averaged SST (color) and surface current (white vector). The arrow boxes are different surface flow systems and the blue solid-line indicates SST fronts. The black dot indicates the turning position of the upwelled particles and the black dash-line indicates the boundary of the onshore transport near the bottom shown in Figure 10(b). (b-i) Two vertical temperature and density anomaly profiles at the beginning (black) and 24 hours later (red) of the particle tracking for four locations. 130

Figure 7.12 (a) cross-shore momentum terms, (b) alongshore momentum terms for the cross-section (1), section (2), and section (3) where (C) is Coriolis force, (A) is nonlinear advection, (P) is pressure gradient force, and (V) is vertical mixing. Colors indicate 24 hours averaged momentum terms during the 2015 circulation. 137

Figure 7.13 Dominant forcing mechanisms influencing the circulation during the selected period for three cross-sections (red) near the bottom (a) and surface (b) of the water column. Arrows indicate the direction of the alongshore and cross-shore circulation at each location and numerals in the arrows indicate the alongshore and cross-shore components of dominant forcing mechanisms at each location. The gray arrows in (b) indicate the lower surface flow. Note that the arrows are not scaled in magnitude or direction of the circulation. 144
Figure 7.14 Thirty six hour averaged SST (color) and surface current (white vector) during the 2017 circulation. Descriptions are identical to Figure 7.11(a). 145
Figure 7.15 Twenty four hours averaged momentum terms during the selected period on Jul 2017. (a) cross-shore momentum terms, (b) alongshore momentum terms for the cross-section (1), section (2), and section (3) where (C) is Coriolis force, (A) is nonlinear advection, (P) is pressure gradient force, and (V) is vertical mixing. 147
Figure 7.16 Dominant forcing mechanisms influencing the circulation during the selected period for three cross-sections (red) near the bottom (a) and surface (b) of the water column. The description is identical to Figure 7.13. 148

SUMMARY

This thesis contains two different topics: 1) Wave energy resource assessments, characterizations, and classifications for US coastal waters, 2) Numerical studies for three-dimensional circulation during coastal upwelling favorable winds on the inner shelf near Point Sal, California.

Ocean waves are a largely abundant and untapped renewable source of energy with limited environmental impact and high energy density. Although ocean waves have significant energy potential, the technology is in early stages of development due to high costs from lower conversion efficiencies as well as risks to operations, maintenance and survival. This study characterizes and classifies the wave energy resource by performing a comprehensive resource assessment of the wave energy for the US. The work for this portion includes three parts.

The first part focuses on describing the wave energy resource parameters or metrics for characterization, e.g., wave energy potential, dominant frequency, directional and temporal variability. Partitioned wave parameters generated from a 30-year WaveWatch III model hindcast are used to estimate the total wave energy potential as an annual available energy (AAE), which is a theoretical annual energy production per unit energy capture length without considering energy conversion efficiencies. The distribution of AAE by peak period, wave direction, month, and year are important attributes of the wave energy resource that can be quantified using simple summary metrics (indices), including spectral width, energy-weighted period, directionality coefficient, and direction of maximum directionally resolved AAE. These metrics are used to characterize long-term

AAE trends, including inter-annual and seasonal variability. These temporal attributes of the wave energy resource can be parameterized by simple indices as measures of the variability, or constancy, of the resource, which can affect the capacity factor and annual energy production of a wave energy generation project. Geographical distributions of the AAE and these seven resource parameters delineate distinct wave climates and wave energy resource regions within US coastal waters, which supports regional energy planning and project development.

The second part uses these parameters to delineate and describe eleven distinct US wave climates or wave energy resource regions based on the key attributes of the resource, wave energy potential, resource attributes, assessed from the part 1. In order to gain a high-level wave resource characteristics, marginal and joint energy distributions of the wave energy in terms of the peak period, wave direction and month, and corresponding resource parameters are provided. The frequency dependence, directional and temporal variability of the conditional wave energy resources at each region is characterized, e.g., the spectral width of the wave energy from a particular direction or month, directionality coefficient of the wave energy within a particular frequency or month. These assessments and characteristics of the conditional wave energy resources can contribute to WEC industries by providing the resource quality of all wave systems and recommending target wave systems for energy generation at each region. Detailed characteristics of energetic wave systems contributing to the total energy at each region are identified and described by linking global and local wind climates. Finally, representative characteristics of the wave energy resources for the eleven regions are summarized.

In the third part, wave energy resource classification systems for the US is developed based on wave power and its distribution with peak period. Energy resource classification systems are useful assessment tools that support energy planning and project development, e.g., siting and feasibility studies. They typically establish standard classes of power, a measure of the opportunity for energy resource capture. As the operating resonant period bandwidth of a wave energy converter (WEC) technology is an important design characteristic, the dominant period band containing the largest energy content is identified among three peak period band classes. The classification systems, comprised of four power classes and three peak period band classes, are based on the total wave power or the partitioned wave power in the dominant peak period band. This work establishes a framework for investigating the feasibility of a compatible wave climate (design load) conditions and WEC technology classification system to reduce design and manufacturing costs.

The circulation during coastal upwelling events near Pt. Sal, a 5km headland in southern California, is considered complex not only due to the complex bathymetry and coastline but a confluence of distinct alongshore currents, e.g., California Undercurrent, coastal jets, and upwelling plumes. The wind stresses and alongshore currents drive geostrophic flows and Ekman transport simultaneously and alongshore variabilities of coastline orientation and a promontory complicate the circulation by creating pressure gradients at the coast. In order to understand the coastal circulation around Pt. Sal, a numerical model, Regional Ocean Modeling System (ROMS) is used for simulations during upwelling favorable wind periods, June-July 2015 and July-September 2017. The coastal upwelling events on 15 July 2015 and 22 July 2017 are identified and three-

dimensional particle trajectories are calculated to analyze the circulation pattern on these periods. As a result, characteristics of the coastal circulation, circulation boundary, upwelling front, convergence/divergence, and stratification, are described. Basic driving forces influencing the circulation during the detected periods, e.g., alongshore/cross-shore wind stresses, California Undercurrent, coastal jet, upwelling plumes, and bathymetry are discussed. The circulation pattern is diagnosed by linking the forcing mechanisms with three-dimensional momentum balances at different locations. Finally, the dominant forcing mechanisms acting on the different regions are identified and two coastal upwelling circulations are compared.

CHAPTER 1.

INTRODUCTION

This dissertation consists of results from two different research projects. One is the study of wave energy resource classification system and the other one is the study of inner shelf dynamics. This study focuses on the primary goal of the projects, which is characterizing and classifying the wave energy resource for the US coasts and analyzing the coastal circulation at the inner shelf of Pt. Sal.

1.1 Wave energy resource

Ocean waves are an abundant and untapped renewable source of energy and wave power is considered a tremendous potential source with limited environmental impact and high energy density [1]. In the US, they make up approximately 80% of the ocean hydrokinetic energy resources (wave, ocean currents, and tidal currents) [2]. As the types and percentage of renewable energy contributions continue to expand within the global and US energy portfolio over the next thirty years, it is important to conduct comprehensive characterizations and assessments of renewable energy resources to realize the full potential of opportunities and challenges for energy generation [2]. Herein, we adopt the definitions of resource characterization and resource assessment given by [3]; resource characterization as the process of parameterizing and mapping the attributes of an energy resource using a set of resource parameters or metrics derived from resource climate data. Resource characterization enables resource assessment, defined as the appraisal or valuation of an energy resource (national, regional, or site) for the purpose of energy generation. Ocean energy resources, including wave energy, are defined at three different levels: the theoretical, technical and practical resource [4]. The theoretical resource is an estimate of the amount of energy that is present in the natural sea. The technical resource is the portion of this theoretical resource that can be captured by using a specified technology, and the practical resource is the portion of technical resource that can be utilized for generation of electricity, or some other energy demand application, after further reductions due to environmental, social, and economic constraints [5].

Although wave power has significant energy potential, wave energy converters (WEC) are at early stages of development. Most of the WECs tested to date have efficiencies well below 50%, and must address formidable risks to operations, maintenance and survival [6]. Comprehensive data on the various attributes of the theoretical wave energy, and of sufficient quality, is not broadly available to fully inform the development of WEC projects [7]. This data gap needs to be addressed to support greater penetration of wave power and WEC technologies into the global and US energy markets. The wave energy generation requires knowledge of the frequency-directional and temporal variability of the resource. There are unique attributes for wave energy pertinent to our ability to generate the energy that require knowledge of the distribution of power as a function of the peak period, direction and month. As wave energy converter (WEC) technologies optimize energy generation by resonating at the period of the incident waves, the gross wave energy potential should be constrained by technology operational periods, driving the optimal design size for a WEC [8], [9]. The energy generation by some WEC technologies may also be limited to a narrow band of wave directions, aligning normal to the predominant wave direction. In addition, the temporal variability of the wave energy is also a significant attribute influencing the consistency of the WEC energy output regarding a capacity factor, a ratio of actual energy produced to its rated full power over a specific time period [10]. For these reasons, descriptions of the distribution of the wave energy potential and resource attributes as a function of the peak period, direction and month are vitally important when assessing the characteristics of the constrained wave energy for WEC technologies that may operate in a specific frequency and direction bandwidth.

Energy resource and technology classification, e.g., wind energy resource and wind conditions (turbine) classification, has provided significant crosscutting benefits in renewable energy industries by codifying resource characterization and assessment, as well as the design and manufacturing of technologies [11]. The success of wind classification systems has motivated interest in developing similar classification systems for wave energy. The main parameter for energy resource classification is the available power, which can be converted to annual average energy production (AEP) and/or inform design attributes of the energy conversion technology, e.g., wind turbine diameter (area of the energy extraction plane), capacity factor, conversion efficiency, and number of units in the farm. For wave energy resources, classification centers on the wave power of the sea surface in kilowatts per meter (kW/m) of wave crest width. Wave power is one of six recommended parameters used to characterize and assess the magnitude and quality of a wave energy resource (IEC 2015) [3]. It has been estimated and mapped for the national resource assessment of the US wave energy resource (EPRI 2011), but power classes have not been defined and mapped to relate the magnitude of wave power to the scale of wave energy production opportunities and to show how these opportunities vary regionally among different US wave climates. There are also unique aspects to wave energy capture that require knowledge of the distribution of the wave power by peak period and direction. Knowledge of the dominant peak period is important for characterizing the performance of wave energy devices and guiding their design. For example, some wave energy converter (WEC) technologies, e. g., point absorbers, maximize energy capture by resonating at the same period as incident waves [8], [12]; therefore, classification systems need to identify the dominant peak period band containing the largest energy. This study aims to improve the wave energy resource assessments by characterizing the resource attributes and classifying the US coastal waters for their potential wave energy. This study investigates and maps the wave resource attributes parameterized by simple indices of the variability, or constancy, of the resource, which can affect the capacity factor and annual energy production of a wave energy generation project. Wave energy regions are delineated along the US coastal waters based on the wave energy resource attributes and detailed characteristics of energetic wave systems contributing to the total energy at each region are identified and described by linking global and local wind climates. Finally, the wave energy resource along the US coastal waters are classified by proposing resource classification systems.

1.2 Coastal circulation

This study focuses on the circulation in and around the inner shelf which is defined as the region where the surface and bottom turbulent boundary layers together occupy the entire water column [13], [14]. The inner shelf is an important pathway between the continental shelf and the surfzone and plays critical roles in coastal ecosystems by influencing the transport of heat, sediment, entrained gases, nutrients, pollutants, and biota.

The circulation during the coastal upwelling has been recognized as central issues on the inner shore regions for decades [15]. Ekman (1905) demonstrated that persistent alongshore winds transport the waters perpendicular to the direction of the wind stress [16]. Along the west coast of the US, Ekman transport in the surface boundary layer creates a cross-shore pressure gradient that forces an onshore flow in a bottom layer [17]. A wide range of processes including wind-driven transports, non-linear internal waves, wave breaking, heat, and sediment transports controls the inner shelf dynamics. Each process can affect the circulation here and relative importance of each process varies widely throughout the region. However, many questions regarding the mechanisms influencing the circulation still remain because of the variety of processes involved with difficulties in isolating the effect of each phenomenon [14].

This study focuses on the circulation near Pt. Sal, a 7 km coastal headland, located 50 km north of Pt. Conception and 3km south of Mussel Pt. in California. The shoreline orientation and the bathymetry adjacent to Pt. Sal abruptly varies in the along-coast direction. Due to the complex topography, the interaction between winds, submesoscale eddies, currents, mixing and surfzone processes generate complex three-dimensional circulations at Pt. Sal [18], [19]. Gan and Allen (2002) and Roughan et al. (2005) modeled the circulation near headlands and found that alongshore flows accelerated around the promontory created different pressure gradients, resulting in different circulation pattern around the promontories [20], [21]. In addition, because the inner shelf is generally characterized as the region where the Ekman surface and bottom boundary layers overlap [14], the typical idealized upwelling circulation may not occur near the Pt. Sal coast.

In order to better understand the circulation near Pt. Sal, a three-dimensional numerical study is conducted using a numerical model, the Regional Ocean Modeling System (ROMS), during upwelling favorable wind periods, June-July 2015 and July-September 2017. The purpose of this study is to characterize the circulation patterns and to identify the forcing mechanisms influencing the circulation during the upwelling events. In order to describe three-dimensional circulation, particle trajectories during the selected period are calculated and characteristics of the circulations are discussed by linking the currents and stratifications. To understand the structures of circulations near Pt. Sal, basic mechanisms directly influencing the circulations are discussed. Finally, the mechanisms are linked with the three-dimensional momentum balances and the dominant forcing mechanisms are identified.

CHAPTER 2.

LITERATURE REVIEW

The literature review is presented in four parts; 1) Wave energy resource assessments, 2) Wave energy resource characterizations, 3) Wave energy resource classifications for United States coastal waters, 4) Inner shelf coastal circulation near Point Sal.

2.1 Wave energy resource assessment

Wave climates are generally characterized by wave height, period, and averaged direction [22]. Although US wave climates have not been formally classified, regional trends are well documented. Along the Northeast Pacific and Bering Sea, the mean significant wave height exceeds 2.6m. Along the Gulf coast, it is generally below 1.2m. The Northwest Atlantic and Hawaii have moderate values ranging from 1.8m to 2.4m [23] where a 29 year global ocean surface gravity wave was simulated using a coupled atmosphere wave model using NOAA/GFDLs High-Resolution Atmosphere Model (HiRAM) and the WAVEWATCH III surface wave model where extensive evaluations of monthly mean significant wave height were validated with buoys and satellite altimeter measurements. Extreme wave heights, based on the 90th percentile of significant wave height, exceed 3.5m along the Northeast Pacific and Bering Sea, and are generally below 2.0m along the Gulf Coast. Hawaii has moderate values ranging from 3.0m to 3.5m. Extreme wave heights in the Northwest Atlantic vary over a large range from 1.5m to 3.7m [9]. Over the past two decades, there is mounting evidence that these wave climates are changing, particularly extremes, with a statistically consistent trend of increasing wave height on the order of millimeters per year along all US coastal waters except Hawaii [24].

Most estimates of theoretical wave energy resource are based on the gross wave power, including assessments for the entire US coastal waters [25], [26]. Global wave energy resource assessments have been reported at relatively coarse resolutions [27]–[29]. For the US, according to the Electric Power Research Institute and U.S Department of Energy [25], [30], the total theoretical wave energy resource along the US continental shelf to the notional 100m depth contour is estimated to be 1,851 TWh/year. The technical resource with at least 8 kW/m is 899 TWh/year, representing 22.2% of the 2012 US Annual Energy Production (AEP) and the maximum practical resource is 522 TWh/year, representing 12.9% of the 2012 US AEP. The theoretical resource in some regions of the US is substantial, with estimates at 502 TWh/year on the West coast (CA, OR, WA), 973 TWh/year in Alaska, 98 TWh/year in Hawaii representing over 100% of the regional 2012 AEP [31]. Theoretical wave energy resource assessments have also been reported for different regions of the US, including the West Coast [32]–[37], Hawaii [38], [39] and the East Coast [40]. The majority of the research has centered on the total wave energy potential including the temporal distribution and variability of the total wave energy potential.

The wave power per unit crest width transmitted by irregular waves, J is proportional to square of significant wave height, H_s and group velocity, C_g which is related with energy period, T_e through the dispersion equation. The T_e of a wave is often described in terms of spectral moments defined by a frequency variance density, $S(f)$.

Although global and national scale wave models internally compute the $S(f)$, generally only total bulk and partitioned bulk wave parameters are retained at each grid location in order to reduce storage requirements [41]. The wave parameters computed from the wave models often consist of significant wave height, H_s and ether peak period, T_p or mean period, T_m, while the T_e is hardly specified and must be computed from theoretical spectral functions with wave parameters when the wave spectrum is unknown[27]. In most previous research, T_e was computed using a relation derived from a theoretical spectral function in terms of the T_p[27], [29], [42]–[47]:

$$T_e = C\,T_p \tag{2.1}$$

where C is a coefficient between T_e and T_p, computed from the spectral moments of the theoretical spectral function and increasing towards unity with decreasing spectral width. For example, $C = 0.86$ for a Pierson-Moskowitz spectrum which is only used for fully developed sea and $C = 0.9$ for a standard JONSWAP spectrum with a peak enhancement factor of 3.3. Gunn and Williams selected the Pierson-Moskowitz spectrum and assumed $C = 0.86$ in quantifying global wave energy resource [29]. The wave energy assessment in Southern New England [42] and South China Sea [43] assumed $C = 1.0$. Most previous studies adopted more conservative assumption of $C = 0.9$ [27], [44]–[48]. A drawback of these approach is that the assumed C introduces some uncertainty into the resulting wave power computes due to complex sea state [27]. The Electric Power Research Institute(EPRI) used a modified Gamma spectrum having two variables relating to the spectral width parameter and spectral peakedness parameter [25]. The variables were calibrated for different 15 regions along the U.S coastal waters using 51 month hindcast data so as to reconstruct sea state spectra that would best fit the complete wave spectrum for that region. The wave power, J in kilowatts per unit wave crest length can be computed as

$$J = \frac{\rho g}{16} H^2 C_g(T_e, h) \tag{2.2}$$

$$C_g = \frac{2\pi}{k}\left(1 + \frac{2kh}{sinh(2kh)}\right)\frac{1}{T_e} \tag{2.3}$$

$$\omega^2 = \left(\frac{2\pi}{T_e}\right)^2 = gk\ tanh\ (kh) \tag{2.4}$$

where ρ is the sea water density (1,025 kg/m^3), k is wave number, h is water depth and ω is angular frequency.

2.2 Wave energy resource characterization

Assessment of wave energy generation requires knowledge of the frequency-directional and temporal variability of the resource. As WECs generally need to resonate with a frequency similar to the peak frequency of the incident waves to efficiently generate energy [8, 9], energy generation can be constrained to the dominant wave period band containing most of the energy. In addition, energy generation by some WEC technologies may be directionally constrained and limited to a narrow band of wave directions. The inter-annual and seasonal constancy of the wave energy is also a significant attribute affecting wave energy generation.

Table 2.1 lists the parameters proposed by the International Electrotechnical Commission (IEC) to characterize wave energy resources [3]. Annual average values of wave power among different wave sites, and different wave climates, are typically used to characterize, compare and assess opportunities, for energy generation. It is widely recognized that this measure of opportunity should be balanced with other resource parameters that characterize the quality of the energy resource, e.g., spectral width, directionality coefficient and the direction of the maximum power. The main attribute of an energy resource that characterizes the resource's potential opportunity for energy generation is the theoretical power. However, this metric, the omni-directional power, is limited because it does not provide information on the distribution of the wave energy by frequency or direction. The resource parameters, spectral width and directionality coefficient, are parameters intended to supplement this important information.

Table 2.1. IEC Wave Resource Parameters [3].

Parameter
Power, J
Sea state (H_s, T_e)
Spectral width, ϵ_0
Directionality coefficient, d
Direction of max power, θ_{Jmax}

Previous studies have adopted these parameters for characterizing regional wave climates [7], [37], [49]. Lenee-Bluhm et al [10] characterized wave energy resource of the US Pacific Northwest using spectral records from ten buoys. Garcia-Medina et al [11] characterized wave energy resource along the continental shelf contours in Oregon and southwest Washington, US using a 7-year hindcast from numerical models (WAVEWATCH III, SWAN). Dallman and Neary [7] characterized wave energy resource at eight US wave energy converter (WEC) test and potential deployment sites using SWAN hindcasts. Most of the previous studies focused mainly on regional characterizations with a limited location. Because the IEC parameters are calculated from a complete directional wave spectrum, national scale characterizations with long records of wave climates require an enormous volume of wave data.

Cornett [27] introduced indices for monthly and seasonal variability of the wave power density and mapped the variability indices over the global domain. Temporal variability of global wave energy assessment was studied at monthly, seasonal, inter-annual and long-term scales using a 60-year data set [50]. Monthly distributions of the global wave power density were computed using a 10-year Wavewatch III hindcast [28]. Long-term annual averages and monthly wave energy distributions were analyzed for California Coast using buoy data set of the Information Data Program (CDIP) and the National Data Buoy Center(NDBC) [32]. Temporal trends of the wave heights, wave periods and the wave power density for the Atlantic coast of the southeastern US are analyzed for a time scale of weeks using NDBC buoy data [40]. In addition to the temporal distributions of the wave energy potential, the wave energy potential in terms of wave period has been assessed. Separate estimates of the wave power density from the wind wave and swell were presented at the global domain using a 10 year Wave watch III hindcast [28]. The wave power density along the California Coast was quantified in terms of significant wave height and peak period in [32] using the data set of CDIP and NDBC and [33] using CDIP, NDBC and Comprehensive Ocean-Atmosphere Date Set (COADS).

The wave energy resource assessments for US coasts have been reported on different scales; Global [27]–[29], [50], entire US coast [51], [52], and regional studies [26], [32]–[40], [49]. The majority of the studies have centered on the total wave energy potential where [26]–[28], [32], [33], [35]–[40], [49], [50], [52] have discussed the temporal distribution and variability of the total wave energy. In addition to the temporal wave energy distribution, the wave energy potential in terms of wave period has been assessed [26], [28], [32], [33], [37], [49]. The wave energy resource parameters, spectra width, directionality coefficient, and temporal variability for the total wave energy potential have been discussed at limited sites and time [26], [37], [49].

2.3 Wave energy resource classification

Classification is the process of reducing descriptions of objects or phenomena to their essential attributes through key metrics, and then organizing them into like-groups. This process results in a common organizational framework, a classification scheme, which facilitates better understanding, knowledge and treatment of the study objects or phenomena of interest. Complex information is reduced to essential metrics. Classification schemes have been adopted by various energy technology industries, including those for selecting the appropriate class technology for given site resource conditions, whether it be the type (class) of conventional hydroturbine, e.g., a Pelton or Kaplan turbine [53], or the appropriate three-bladed horizontal axis wind turbine (HAWT), e.g., IEC Class IA or Class IIB turbine [3].

Conventional hydroturbine classes depend on a site's average flow discharge (a measure of kinetic energy) and average potential energy head; two opportunity metrics. Although there are obvious risks to conventional hydropower energy extraction due to floods and droughts (extremes), these do not influence turbine selection because they can usually be managed through head and flow controls. HAWT classes are selected based on the reference wind speed, which was recently revised by the IEC to represent an extreme 10-minute average wind speed occurring every 50-years on average, and the expected turbulence intensity at a site (IEC 2005). Previously, the reference wind speed represented the annual average value, but as this value is simply estimated as twenty-percent of the 50-year wind speed (IEC 2005) either wind speed can essentially be used as the basis for selecting the turbine class. As a result of this simple linear relationship between extreme wind speed and annual average, wind turbine classification can be interpreted as being driven by either an opportunity metric (annual average wind speed) or risk metric (extreme wind speed).

In both cases, site resource conditions are reduced to essential measures of opportunities and/or risks to energy extraction, where extraction opportunities are generally based on average site conditions, and risks are based on extreme conditions that can compromise the operation or survival of the technology. They have been invaluable to developers and utilities for identifying commercially viable sites, to designers for selecting the appropriate technology class for a site and determining the appropriate O&M strategy. These classification systems have also allowed turbine manufacturers to mass produce turbines of several dominant classes that fall within the predominant ranges of resource conditions rather than designing and fabricating customized turbines for each site, which would be prohibitively expensive.

A preliminary wave energy resource and WEC classification scheme recently presented by Cruz (2015) delineated three wave energy resource (WEC) classes (classes I to III, increasing in energy content) based on plots of mean significant wave height and mean peak period for over three-thousand wave sites in the United Kingdom and Ireland

[54]. As mean significant wave height and wave energy density, generally increase with mean peak period, the classes represent sites with increasing energy content from the lowest class (I), having the lowest mean peak period band, to the highest class (III) having the highest period band. Preliminary WEC classes were proposed for specific WEC archetype subclasses, e.g., two subclasses of a point absorber, based on the root-mean-squared power-take-off (PTO) force derived from the extreme 75th percentile significant wave height for each wave energy resource class. As WEC classification was the main thrust of this study, metrics used for energy resource classification included only the mean significant wave height and mean peak period, which combined define a mean sea state from which other useful energy resource statistics, e.g., mean wave power density, can be derived. The wave energy classes have not been defined and mapped to relate the magnitude of wave power to the scale of wave energy production opportunities and to show how these opportunities vary regionally among different US wave climates.

2.4 Coastal circulation

The coastal circulation during the upwelling favorable wind period is largely influenced by interactions between the wind stresses, current systems, and complex topography. Predominant equatorward winds along the California Coast in summer force an offshore Ekman transport of surface layer waters and the compensating onshore flow at the bottom layer. Intensive observations and numerical studies on the California Coast show the presence of a southward coastal jet generally bringing cold waters near the surface, and a poleward undercurrent bringing warm waters near the bottom during the summer [55]–[57]. In the surface layer, upwelled cold waters generally joined the southward coastal jet [55], [58], [59]. In addition, the Pt. Sal is located at the southern boundary of an upwelling shadow zone (SLO bay Figure 2.1) where trapped warm waters interact with cold upwelling jets and pass through the nearshore of Pt Sal. [60]–[62]. The alongshore variabilities of coastline orientations and a promontory of bathymetry complicate the circulations by influencing pressure gradients at the coast [20], [21]. Therefore, the coastal circulation at Pt. Sal is a combination of the multiple responses derived from the alongshore/cross-shore wind stresses, current systems, and complex coastline and bathymetry. For example, Huyer (1983) discussed that temporal and spatial variations of the cross-shore circulation at the California Coast during summer can be found because the upwelling is not sufficient to overcome the downward isopycnal slopes associated with the poleward current [55]. The literature review mainly focuses on forcing mechanisms driving the circulation including alongshore and cross-shore wind, current systems, surface wave, stratification, and complex coastline and bathymetry.

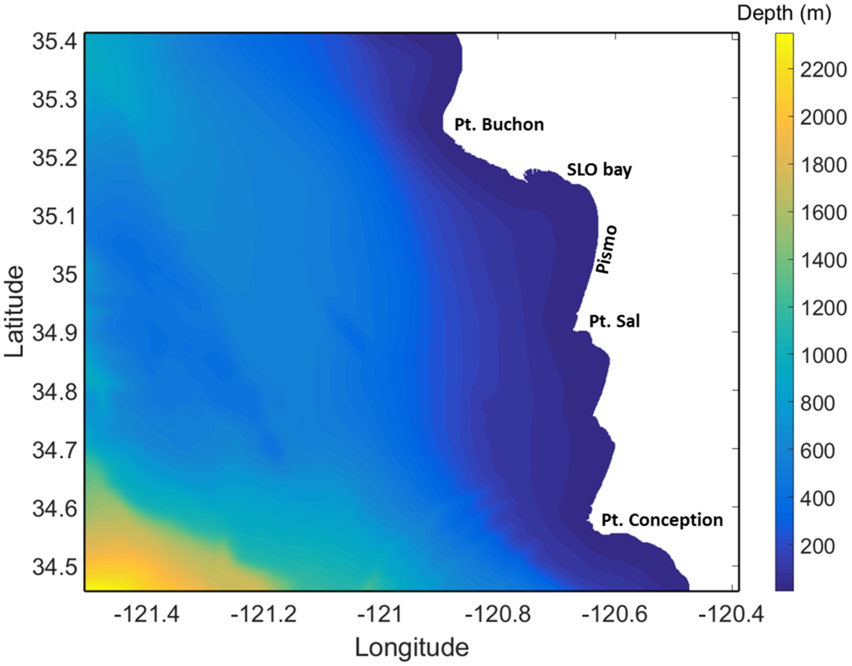

Figure 2.1. Location of Point Sal. The color indicates water depth.

Wind stress transmission is often an important process for inner shelf circulations. Ekman estimated the net transport resulting from a surface wind stress for a linear coastline and general assumptions about the flow including a steady, linear, alongshore uniform wind driven circulation [16]. In deep water, uniform and steady wind stresses drive volume transports in a surface boundary layer (the Ekman layer) where the wind stress balances the Coriolis force. These results can be obtained by integrating the momentum balance over the surface layer and the cross and along-shelf momentum equations are

$$-\rho_o f v = -\frac{\partial P}{\partial x} + \frac{\partial \tau^x}{\partial z} \tag{2.5}$$

$$-\rho_o f u = \frac{\partial \tau^y}{\partial z} \tag{2.6}$$

The transport is $|\tau|/\rho_o f$ and confined to the surface boundary layer (Ekman layer, $\delta_E = \sqrt{2Af}$) where τ is wind stress, ρ_o is a reference seawater density, f is Coriolis frequency, A is a constant eddy viscosity, and P is a pressure. The x and y are horizontal coordinates, u and v are horizontal velocities. The direction of the wind driven transport is 90 degrees to the right of the wind stress in the Northern Hemisphere.

Given the simple eddy-viscosity profile, Ekman derived analytical solutions for the inner shelf transport driven by the along-shelf wind stress for an unstratified shelf [16]. The along-shelf uniform wind over the along-shelf uniform unstratified water column forces onshore or offshore flow in the surface boundary layer and a compensating return flow in the bottom boundary layer. In the interior region between the surface and bottom boundary layers is a geostrophic along-shelf flow, balanced by cross-shelf pressure gradient. The bottom stress generated from the along-shelf flow drives the off shore or onshore flow in the bottom boundary layer that compensates for the flow in the surface boundary layer. When the wind forces an offshore surface flow, the compensating flow at the bottom transports water that is cooler and more nutrient laden than the nearshore and this process is referred as an upwelling. The reversed process is referred as a downwelling.

For the upwelling, on the middle shelf where the interior region exists, offshore transports at the surface boundary layer and compensating onshore flow at the bottom boundary layer are equal to the Ekman transport in the deep water [63]. In the very near coast, there is less cross-shore transport due to the non-rotating flow which is the downwind. The region between the two where the water depth is shallower than the boundary layer the cross-shore transport tends to linearly decrease with decreasing water depth. In the inner shelf where the surface and bottom Ekman layers cannot fully develop due to the shallower water depth, wind-driven surface and bottom boundary layers overlap and the transport decreases as the water depth decrease [64]. Several observations of decreased Ekman transport in shallow water have demonstrated that along-shelf winds have a limited role in driving cross-shelf circulation [14], [64].

Numerical models and observations on the continental shelf indicate that the along-shelf wind is not very efficient at driving cross-shore flow on the inner shelf [17], [63]–[65]. Ekman (1905) indicates that the cross-shelf winds over the inner shelf can transport the water column in the downwind direction leading directly to upwelling or downwelling with a sea level set down or setup [16]. The cross-shore wind stress contributes to mixing the water column before the Coriolis acceleration affects the water column, and as a result, the cross-shelf wind stress is a substantial force in the cross-shore circulation. According to an idealized numerical simulation over the uniform along-shelf, onshore wind stress makes the surface waters pile up at the coast and the pressure gradient generates an offshore flow below the onshore flow [65], [66]. The circulation is reversed with offshore wind. Fewings et al. (2008) observed that the cross-shore wind stress is more significant at driving cross-shore circulation in the unstratified water column than along-shore wind stress using wintertime measurements at a particular site [67]. It also indicates the cross-shore wind driven cross-shore transport increases linearly with increasing water depth. However, in deep water, the cross-shore wind stress is balanced by the Coriolis acceleration and there is no cross-shore wind driven cross-shore transport in the surface boundary layer [67].

A baroclinic alongshore pressure gradient derived from remotely forced coastal trapped waves, sea level setup by coastal winds or density gradients [68] can drive a poleward California undercurrent [69], [70]. The southward coastal jets along Pismo beach (Figure 2.1) plays different roles in the circulation at the nearshore region by influencing the pressure gradient and Coriolis force. In addition, the southward cold upwelling plume adjacent to the Pt. Buchon (Figure 2.1) also create the alongshore pressure gradient and forces offshore geostrophic flows by balancing the Coriolis force at the surface.

Surface waves force various inner shelf mechanisms generating cross-shelf transport and other circulation [71]–[74]. Physically, surface waves transport water onshore through a Stokes drift which is a particle transport correlated with wave height and the orbital velocity. The velocity of the particle in the Lagrangian reference frame is relatively larger at the top than at the bottom. The net displacement of the water particle generates onshore volume transport. The Stokes drift velocity in a Lagrangian reference frame can be estimated using linear wave theory. In the along-shelf uniform flow, a net cross-shelf transport is zero everywhere and there should be an offshore flow below the surface waves, referred to as undertow. Theoretically, the offshore Eulerian return flow is equal in magnitude to the onshore Stokes drift at all depths with weak vertical mixing, resulting in no cross-shelf exchange [75]–[77]. With strong vertical mixing, however, the spatial inhomogeneity of the surface waves cause mismatches in the vertical structure of the onshore Stokes flow and offshore Eulerian flow. These fluctuations can induce cross-shore transport [67], [78]. Therefore the structure of the wave driven cross-shelf transport depends on the vertical mixing strength. Observations found that surface wave driven return flows had a significant effect on the cross-shelf transport in the inner shelf, although the transport was mainly driven by the cross-shelf wind stress. Especially, the cross-shelf transport can be governed by surface wave forces in water depths less than 15 m [67]. If the waves propagate towards the coast at an angle, the wave bottom stress generated by the bottom friction causes near bottom wave streaming in the direction of wave propagation [76], [79]. A study shows that the bottom wave streaming can produce a non-negligible impact on the cross-shore transport over the inner shelf [80].

Stratification can play an important role in the inner shelf region and interact with the wind and wave forcing significantly influencing cross-shelf transport [11]. Stratification is generally expected to suppress vertical mixing by thinning the surface and bottom boundary layers and narrowing the overlap between the two. The inner shelf width and location related with the thicknesses of the boundary layer vary in space and time depending on the strength of the stratification as well as the wind and wave forcing. The effect of the stratification on the inner shelf circulation response to along-shelf wind forcing is correlated with the dynamical relationships of the stratification, vertical mixing, and cross-shelf circulation [17], [65]. For downwelling-favorable winds over a stratified shelf, two regions which are separated by a downwelling front are formed. An unstratified inner shelf region is formed by interactions between the onshore flow in the surface boundary layer and vertical mixing and cross-shelf circulation in this region is very weak [14]. The downwelling front on a stratified shelf isolates the inner shelf from the cross-shelf circulation. For upwelling-favorable winds over a stratified shelf, the inner shelf region with weaker stratification is also separated by an upwelling front. In contrast to the downwelling case, however, cross-shelf circulation and stratification is maintained onshore of the upwelling due to the dense water drawn from deeper depths along the sloping bottom [14]. The response of a stratified water column to cross-shelf wind forcing is similar to the unstratified water because the downwind transport is confined to the surface boundary layer where the density is well mixed in both [61]. Due to the well-mixed surface layer with less advective buoyancy fluxes, there is no obvious asymmetry in the stratified response to onshore and offshore winds. The onshore flow driven by the along-shelf bottom stress in a bottom boundary layer promotes stronger stratification near the bottom by transporting the dense water. On the other hand, offshore flow in the bottom boundary layer leads to a thicker layer and weaker stratification.

Coastline geometry is another major influence on the coastal circulations. *Gan and Allen* (2002) modeled the circulation near the prominent headlands of Pt. Arena and Pt. Reyes [20]. It found that upwelling favorable alongshore flows accelerated as the currents flowed around the large promontories. The accelerated flows created a momentum balance, such that northward pressure gradients set up north of the headland and southward pressure gradients set up south of the headland. The northward pressure gradients were balanced by southward nonlinear advection. The southward pressure gradients in the lee of the headland were balanced by the geostrophic onshore flow. This onshore flow enhanced the upwelling in the lee of headlands, where cooler water is typically observed. The Pt. Sal, a 7-km headland located 50 km north of Pt. Conception on the central California Coast (Figure 2.1), is ideal for studying the flow structure around smaller promontories. North of Pt. Sal, the coastline is primarily oriented 15°T for 15 km. At the headland, the coast turns east-west for 2 km, before becoming north-south again.

2.5 Motivation for present study

Wave energy resource characterization and classification for the United States

There are specific aspects of wave energy pertinent to our ability to capture the energy that requires knowledge of the distribution of power density as a function of the peak period, direction and month. As wave energy converter (WEC) technologies need to resonate at the same period as incident waves to efficiently capture energy [69, 70], energy capture is generally constrained to the dominant wave period band containing most of the energy. In addition, energy capture by some WEC technologies may be limited to a narrow band of wave directions. The inter-annual and seasonal constancy of the wave energy resource is also a significant attribute affecting the available energy. However, the majority of the research has centered on the total wave energy potential or temporal distributions and variability of the total wave energy potential. It focused mainly on regional characterizations with a limited location. Because the IEC parameters are calculated from a complete directional wave spectrum, national scale characterizations with long records of wave climates require an enormous volume of wave data. The joint frequency-direction-time resolved wave energy and corresponding resource attributes have not been extensively assessed and characterized for the US coastal waters.

The success of HAWT classification, in particular, has motivated the recent development of a similar classification systems for wave energy resources and WEC technologies; and the various manifestations of classification schemes developed for HAWTs over the last few decades provide valuable analogues guiding the development of wave energy classification systems. Given importance of the period dependence of the WEC technologies, classification needs to identify the dominant peak period band of the wave containing the largest energy content. This dominant peak period band drives the selection of a WECs operating period bandwidth and the WECs optimal design size. The systematic organization, reduction and codification of wave energy resource attributes within a population of potential wave sites, i.e., wave energy resource classification, is the capstone of any regional resource assessment. If well designed, a classification scheme composed of several to a dozen different resource classes, can provide a common language and cross-cutting guidance for a wave energy industry composed of different stakeholders, e.g., regional energy planners, utilities, technology developers, designers, and standards organizations.

Numerical simulation of coastal circulation near Point Sal, California

Previous studies have often discussed the upwelling circulation along the California Coast by explaining the upwelling plumes with the surface temperature, salinity, nutrients changes, or offshore Ekman transport [56], [58], [81], [82]. The cross-sections or point profiles during the upwelling favorable winds are often used to describe consequences of the upwelling circulations in the Eulerian point of view [58], [62], [81]. Along the along-shelf uniform topography, the upwelling circulation is generally well described by those cross-section and point profiles [83]. However, these approaches may not be enough to describe the circulation on complex bathymetry because coastal upwelling fronts and the edge of the upwelling jets are often indistinguishable [55], [59]. In the presence of the strong alongshore currents over the along-shelf varying topography, however, the upwelling circulations significantly vary over the along-shelf thus require the three-dimensional analysis with time evolutions. In addition, the coastal circulation at Pt. Sal is a combination of the multiple responses derived from the alongshore/cross-shore wind stresses, and complex coastline and bathymetry.

CHAPTER 3.

WAVE POWER

In this chapter, the theoretical wave power (kW/m) and AAE (MWh/m), partitioned by peak period, direction, and time (month, year), are calculated from outputs of a thirty-year spectral wave climate model hindcast (WaveWatch III) for US coastal waters.

3.1 Wave data

The wave resource statistics derived using the phase II 30-year hindcast from the 3rd generation (3G) spectral wave, WaveWatch III® (WWIII) [9]. These hindcasts have been developed by the National Oceanographic Partnership Program (NOPP) project. WAVEWATCH III solves a random phase spectral action density balance equation for wavenumber-direction spectra. The assumption of this equation is that properties of the water depth and current, as well as the wave field itself, vary on time and space scales that are much larger than the variation scales of a single wave. Phase 1 used the current operational WAVEWATCH III model (v3.14) using a wind field from a long-term reanalysis, Climate Forecast System Reanalysis (CFSR) [84]. Phase 2 used the WAVEWATCH III model (v5.08) using bias-corrected CFSR winds [85], [86].

Buoy measurements cannot provide enough sites with adequate spatial coverage to develop a resource classification scheme, and most buoys lack a sufficient period of record to adequately characterize these resource statistics. Three types of model results are archived from the model with a spatial resolution of 4 arc-minutes: (a) complete directional wave spectra at limited grid points, (b) bulk wave parameters at each grid point and (c) spectral partitioned wave parameters at each grid point. Due to the limitation of complete directional wave spectra data (1,951 sites) and importance of peak period dependence of WEC technologies, the hourly spectral partitioned data spanning thirty years from 1980 to 2009 for 77,346 sites are used in this study. Although frequency-directional wave spectra are internally computed from the model, data at limited grid points are retained due to storage requirements. The locations of these sites and their water depths are shown in Figure 3.1. The water depths for all sites in this study are classified as intermediate or deep with normalized peak frequencies: $f_p > 0.05\sqrt{g/h}$. The shallow depth sites are excluded from the study due to the limitation of the WWIII wind-wave models that cannot compute the complicated wave interactions for near-shore sites [27].

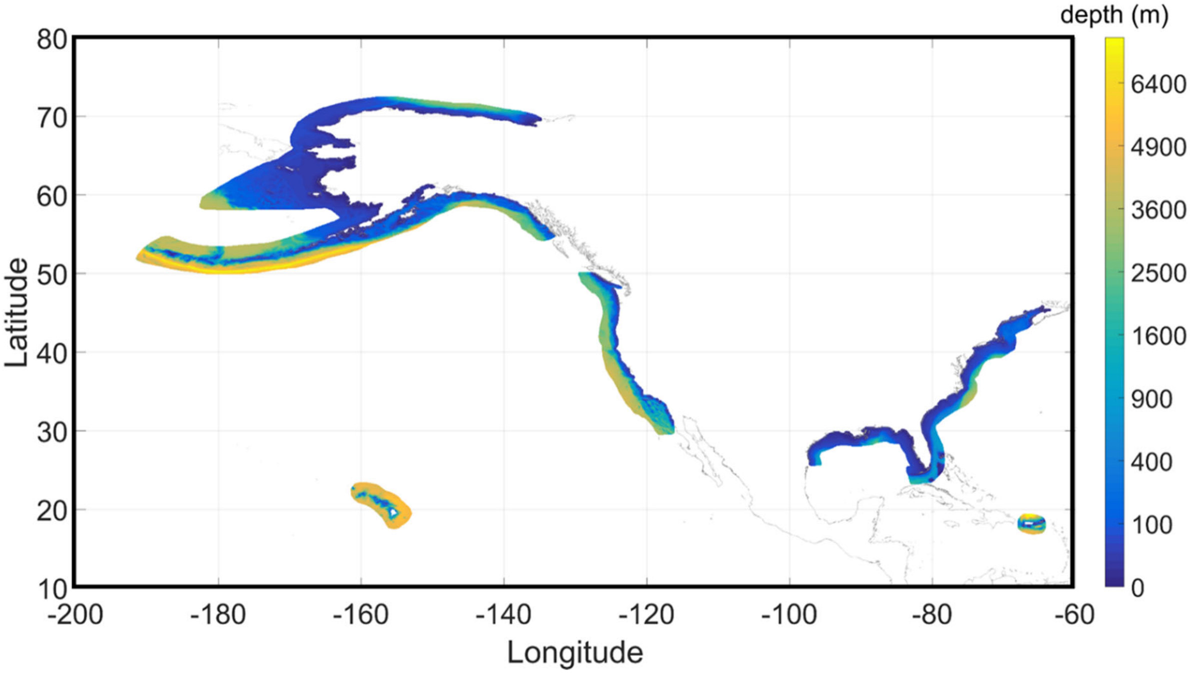

Figure 3.1. Geographic distribution of spectral partition data for the US coastal waters (77,346 sites). Colors indicate water depth (m).

According to WWIII user manual, a complete directional wave spectrum is divided into partitions representing energy from sub-peaks within the spectrum. These partitions are derived using an algorithm initially developed for watershed identification [87], [88]. Wind seas are identified using a wave age criterion such that partition peaks fall within a bounded region. All wind sea partitions from a given input spectrum are combined and assigned to the first partition. All remaining partitions are considered as swell. WWIII provides quantitative parameters of individual spectral partitions, e.g., wave height, peak period, mean direction, wind-sea fraction, and the number of partitions.

3.2 Validation of data

The hindcast is validated with point wave measurements at twenty-six buoy sites obtained from the website of the National Data Buoy Center (NDBC, www.ndbc.noaa.gov) which had at least 14 years of recorded spectrum data for the US coastal waters and at least 7 years for 3 locations. The complete directional wave spectra of the hindcast are extracted from the grid points where the location and water depth are close to the corresponding buoy stations, and are compared to the non-directional wave spectra of buoy measurements. The geographic distribution of these buoys is shown in Figure 3.2. Information on these buoys is summarized in Table 3.1.

This validation is carried out using the methodology recommended by the IEC standard: TS 62600-101 [3]. According to the class of resource assessment referred from the IEC standard, WWIII hindcast data can be applied to a reconnaissance resource assessment class. Table 3.2 specifies the maximum acceptable weighted mean systematic and random errors for key validation parameters of the reconnaissance class. The systematic error is defined as the bias, while the random error is defined as the standard deviation of the errors [3].

Table 3.1. List of wave measurement buoys providing spectral records for the US coasts

Station	Lat.(°)	Long.(°)	Depth(m)	Data Interval
41013	33.4	-77.7	24	2003-2009
42001	25.9	-89.7	3365	1996-2009
42002	26.1	-93.8	3130	1996-2009
42003	26.0	-85.6	3300	1996-2009
42007	30.1	-88.8	15	1997-2009
42019	27.9	-95.4	82	1996-2009
42020	27.0	-96.7	80	1996-2009
42035	29.2	-94.4	16	1996-2009
42036	28.5	-84.5	50	1996-2009
42039	28.7	-86.0	274	1996-2009
42040	29.2	-88.2	164	1996-2009
44014	36.6	-74.8	48	1996-2009
44025	40.3	-73.2	41	1996-2009
46011	35.0	-121.0	464	1996-2009
46015	42.8	-124.8	420	2002-2009
46025	33.7	-119.1	905	1996-2009
46026	37.8	-122.8	53	1996-2009
46027	41.9	-124.4	46	1996-2009
46028	35.7	-121.9	1104	1996-2009
46029	46.2	-124.5	144	1996-2009
46041	47.4	-124.7	114	1996-2009
46042	36.8	-122.5	2098	1996-2009
46050	44.7	-124.5	137	1996-2009
46053	34.3	-119.9	427	1996-2009
46066	52.8	-155.0	4545	2000-2009
51001	24.4	-162.1	4869	1996-2009

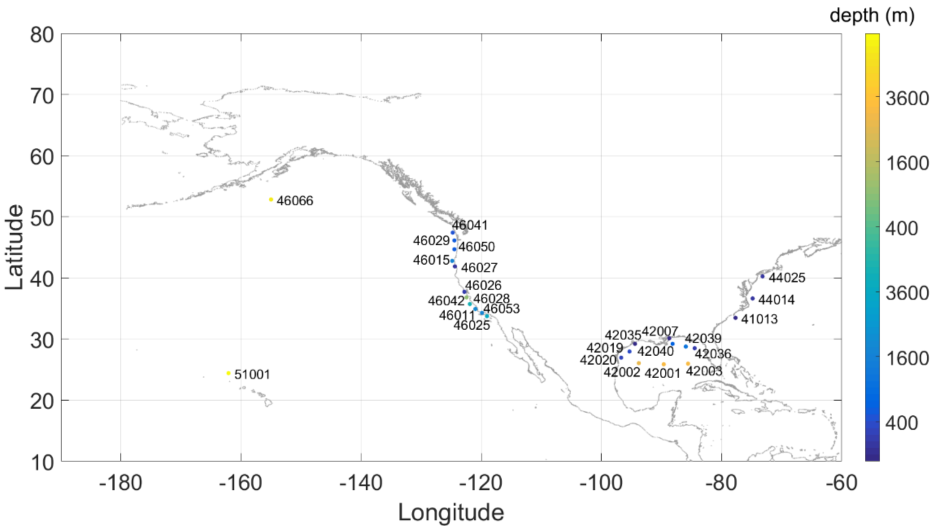

Figure 3.2. Location of twenty-six buoys and its station number. Colors represent the water depth (m).

Table 3.2. Maximum acceptable error of key validation parameters for the reconnaissance class of a resource assessment project [3].

Error	Parameters	Maximum acceptable error
Systematic error, $\boldsymbol{b}(\boldsymbol{e_p})$	Significant wave height, H_{m0}	10%
	Energy period, T_e	10%
	Non-directional wave power, J	25%
Random error, $\boldsymbol{\sigma}(\boldsymbol{e_p})$	Significant wave height, H_{m0}	15%
	Energy period, T_e	15%
	Non-directional wave power, J	35%

The validation is based on constructing non-directional $H_{m0} - T_e$ scatter table representing proportional frequency of occurrence, f_{ij} of different waves over the duration of the measurements [3]. The H_{m0} cells have a width of 0.5m and T_e cells have a width of 1.0s. The error, e_p between the buoy and hindcast data are allocated to scatter table cells based on the corresponding measured H_{m0} and T_e. Then the errors are normalized and separated into a systematic error, $\mu_{ij}(e_p)$ and a random error, $\sigma_{ij}(e_p)$. Also, weighting factors, w_{ij} are calculated for each cell by the product of f_{ij} and non-directional wave power, J_{ij}.

$$w_{ij} = J_{ij} f_{ij} \tag{3.1}$$

The weighting factor shall be normalized such that its sum is unity, as:

$$\widehat{w}_{ij} = \frac{w_{ij}}{\sum_{i,j} w_{ij}} \tag{3.2}$$

Finally, the weighted mean systematic error, $b(e_p)$ and random error, $\sigma(e_p)$ are calculated as following equations where p is characteristic parameter $p \in [J, H_{mo}, T_e]$.

$$b(e_p) = \sum_{i,j} \widehat{w}_{ij}\, \mu_{i,j} \qquad \sigma(e_p) = \sum_{i,j} \widehat{w}_{ij}\, \sigma_{i,j} \tag{3.3}$$

The validation results are summarized in Table 3.3. Overall, the systematic errors and random errors satisfy the minimum validation requirements shown in Table 3.2, except for a few stations which are highlighted in bold type. By inspecting the systematic errors, it is found that the values of H_{m0} and J from the WWIII appear to be generally underestimated. The relatively large underestimations are mainly observed at the buoys located in the nearshore Gulf Coast. This underestimation is probably due to limitations of WWIII modeling wave interactions for near-shore sites [27]. Excluding the stations located in the nearshore along the Gulf Coast and southern California Coast, H_{m0} weighted systematic errors range from -10% to -4%, T_e weighted systematic errors range from -10%

to 3% and J weighted systematic errors range from -20% to 0%. H_{m0} weighted random errors range from 11% to 15%, T_e weighted random errors range from 7% to 8% and J weighted random errors range from 26% to 35%. Note that the buoy measurements near the Alaska coast, Hawaiian coast, and Puerto Rico coast are sparse; therefore, the model data and resulting analysis for these regions have increased uncertainty due to the limited validations.

Table 3.3. Validation results between the buoys and WWIII model data.

Station	Systematic error, $b(e_p)$			Random error, $\sigma(e_p)$		
	H_{m0}	T_e	J	H_{m0}	T_e	J
41013	-7	-4	-15	13	8	30
42001	-4	-6	-9	14	8	35
42002	-8	-7	-18	14	8	29
42003	-9	-10	-21	15	9	31
42007	-28	-17	-55	15	8	23
42019	-11	-10	-26	13	7	26
42020	-15	-8	-31	13	7	24
42035	-17	-13	-38	14	7	25
42036	-14	-8	-29	15	8	33
42039	-14	-9	-29	15	8	31
42040	-11	-7	-23	16	8	34
44014	-4	-6	-11	14	8	30
44025	-8	-4	-14	14	8	32
46011	-6	2	-5	12	7	29
46015	-6	2	-8	12	7	27
46025	-15	0	-24	17	13	34
46026	-10	4	-11	11	7	26
46027	-8	3	-14	13	7	29
46028	-8	3	-11	12	7	26
46029	-5	2	-4	11	6	27
46041	-1	3	0	13	6	30
46042	-5	3	-4	11	6	27
46050	-7	1	-11	12	6	26
46053	-20	2	-31	16	11	33
46066	-4	0	-4	11	7	27
51001	-7	0	-11	12	8	30

3.3 Wave power calculation

The wave power in kilowatts per unit wave crest length transmitted by irregular waves is described as

$$J = \sum_{i} \rho g C_{g,i} S_i \Delta f_i \tag{3.4}$$

where ρ is the sea water density (1,025 kg/m^3), $C_{g,i}$ is the group velocity at the ith frequency and $S_i \Delta f_i$ is the total variance at frequency f_i. To calculate the wave power using the wave parameters, an equivalent equation which is considered by IEC standard and Cornett [3], [27] is used as

$$J \approx \frac{\rho g}{16} H^2 C_g(T_e, h) \tag{3.5}$$

where H is significant wave height, $C_g(T_e, h)$ is the group velocity of waves with energy period T_e in water depth h.

$$C_g = \frac{2\pi}{k}\left(1 + \frac{2kh}{sinh(2kh)}\right)\frac{1}{T_e} \tag{3.6}$$

Where T_e is energy period which is defined in terms of spectral moments. The wave number k, depth h and energy period T_e are related through the dispersion equation:

$$\omega^2 = \left(\frac{2\pi}{T_e}\right)^2 = gk\ tanh\ (kh) \tag{3.7}$$

where ω is the angular frequency. The energy period can be applied to Eq. (3.6, 3.7) by assuming that all of the variances of the wave is propagated at the group velocity associated with the energy period.

T_e is defined in terms of spectral moments that are derived from frequency wave spectra as $T_e = \int S(f) f^{-1} df / \int S(f) df$. Therefore, reconstructions of the wave spectra from all individual partitions are needed. To reduce the extensive computations required for this reconstruction, an alternative method for computing T_e is to use conversion factors between peak period and energy period, $T_e = C\, T_p$. The conversion factor, C , is analytically derived by integrating a parameterized wave spectrum, $S(f)$, which is a function of T_p. The parameterized wave spectrum depends on the wave system which is conventionally sorted into wind-sea or swell. For wind-sea and swell, a Pierson-Moskowitz spectrum and a Gaussian spectrum are used as the parameterized wave spectrum, respectively. Although a JONSWAP spectrum is more widely used to parameterize the wind-sea, the Pierson-Moskowitz is adopted in this study to minimize an overestimation of T_e (see Appendix A). Based on a combining algorithm of all wind-sea peaks [41], [89], the largest peak of the wind-sea absorbs energy of the other wind-sea peaks. Therefore, the energy shifted to lower frequencies contributes to overestimating the energy. Similarly, a peak enhancement of the JONSWAP spectrum also shifts the energy towards the peak frequency, resulting in a longer energy period. In addition, the peak enhancement factor of the JONSWAP spectrum could be achieved by model fitting for each of the directional spectra [25]. Alternatively, one could apply empirical formulae [90], but this approach is prone to large errors. In this study, C=0.858 for wind-sea and C=1.0 for swell is used to estimate T_e. A detailed derivation and validation of the conversion factors is presented in Appendix A.

As a base measure of primary wave energy resource, wave power in kW/m is computed from each hourly partition data. The partitioned wave power, J_n in kilowatts per unit wave crest length in meters transmitted by irregular waves are described as

$$J_n = \frac{\rho g}{16} {H_n}^2 C_{g\_n} \tag{3.8}$$

where H_i is partition significant wave height, C_{g_n} is the partition group velocity defined as

$$C_{g\_n} = \frac{2\pi}{k_n}\left(1 + \frac{2k_n h}{sinh(2k_n h)}\right)\frac{1}{T_{e\_n}} \tag{3.9}$$

and T_{e_n} is the energy period of the partition. The partition wave number k_n, depth h and T_{e_n} are related through the dispersion equation.

$$\omega_n{}^2 = \left(\frac{2\pi}{T_{e\_i}}\right)^2 = gk\ tanh\ (k_n h) \tag{3.10}$$

The ω_n is the partition angular frequency.

In order to assess not only the total wave power itself but also the characteristics of the wave energy, monthly and inter-annual distributions of the partitioned wave power are quantified in terms of wave direction bins (T_b, resolution of 10° clockwise from true North) and peak period bins (θ_b , resolution of 1s). The 30-year averaged wave power,

$J_m(T_b, \theta_b, M, Y)$ is computed as the summation of J_n pairs in the cell (T_b, θ_b, M, Y) divided by the number of hours in 30-year (T_{30year}) as

$$J_m(T_b, \theta_b, M, Y) = \sum_{1}^{N} J_n \Big/ T_{30year} \tag{3.11}$$

where N is the number of J_n pairs in the cell (T_b, θ_b, M, Y).

While the complete wave spectrum indicates variances of waves, the $J_m(T_b, \theta_b, M, Y)$ represents the theoretical power of wave systems within a particular wave direction and frequency. An advantage of using the $J_m(T_b, \theta_b, M, Y)$ instead of the complete wave spectrum is that the spectral partitioned data isolates and defines a particular wave train within an irregular wave field. It is significantly important to characterize the frequency, directional and temporal attributes of wave energy resource as an irregular wave is a superposition of multiple regular wave systems and a device might only be able to resonate with a portion of the overall wave spectrum.

An example of a location off the coast of Hawaii is shown in Figure 3.3(a) represents mean wave power, $J_m(T_b, \theta_b)$, in terms of peak period partition and wave direction in degrees clockwise from true North. Interestingly, this wave power distribution has two separate peaks occurring at around 8 seconds and 14 seconds, a unique feature of the Hawaiian wave climate. As shown in Figure 3.3(b-c), the maximum wave power occurs at a peak period of 14 seconds and a wave direction of 310°.

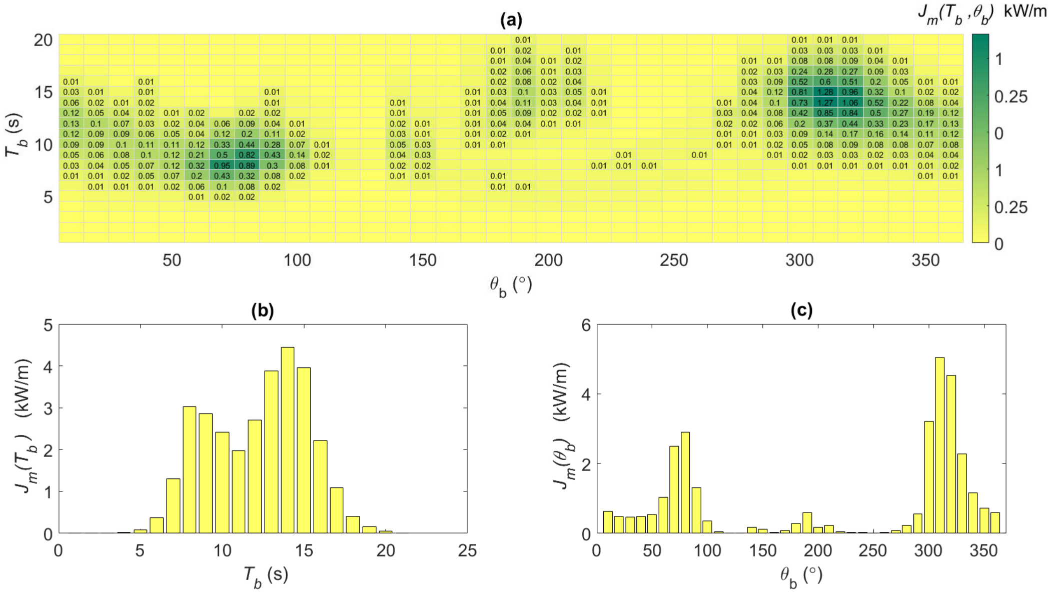

Figure 3.3. Sample calculation of wave power of the 30-year average for an example site (Hawaii, 22.7N 160.5W): (a) mean wave power, $J_m(T_b, \theta_b)$. Color and the number represent wave power of the cell in kW/m. (b) wave power as a function of the peak period, $J_m(T_b)$. (c) wave power as a function of wave direction, $J_m(\theta_b)$.

3.3.1 Annual Available Energy (AAE)

The AAE is the analogous to annual energy production (AEP) per unit crest length assuming all the energy resource is converted. It can be thought of as the theoretical available wave energy resource for a given location. The AAE, as a function of the peak period and wave direction, is calculated as

$$AAE(T_b, \theta_b, M, Y) = T_{year} \cdot J_m(T_b, \theta_b, M, Y) \tag{3.12}$$

where T_{year} is the number of hours in a year taken to be 8,766 hours. The AAE as a function of any parameters, e.g., $AAE(T_b)$, $AAE(\theta_b, M)$, is taken as the summation over the other parameters. The 30-year averaged total AAE is simply sum of all components.

Alternatively, the mean annual wave power is calculated as the AAE divided by the number of hours in a year.

3.4 Wave power along the US coastal waters

For reasons mentioned above, descriptions of the distribution of the wave power over peak period and direction are useful when characterizing attributes of the wave energy resource for WEC technologies that may operate in a specific frequency and direction bandwidth. In Figure 3.4, the distribution of the percent contribution of total energy is given in joint plots of peak period and direction (in orthogonal and polar coordinates), and over peak period only. The merged $J_m(T_b, \theta_b)$ is calculated by adding corresponding elements of each $J_m(T_b, \theta_b)$ matrix for five U.S. wave climate regions, divided by the total sum of merged $J_m(T_b, \theta_b)$. The colors indicate the percent contributions of the averaged $J_m(T_b, \theta_b)$(left and middle) and $J_m(T_b)$(right) of all sites located in the particular region to their averaged total wave power. The dark green color represents the waves with a large contribution to the total energy. A red line indicates the averaged $J_m(T_b)$ of all sites located in the particular region.

These plots illustrate unique characteristics and interesting regional trends among the different US wave climates. Not only do they indicate how much potential wave energy resource is found in a given region, but also the source or origin of this wave energy (hotspots) in terms of peak period (frequency) and direction. These are key characteristics that inform the design of an individual WEC device, with natural resonance driven by the dominant peak period, and the orientation of the WEC farm to optimize energy capture.

For the Alaska coastal region, the most energetic sea states come from the southwest direction and are within the peak period partition ranging from 10 to 14s. For the West Coast, the sea states from the northwest direction at peak periods ranging from 13 to 14s contribute most to the total energy. With most of the energy transferred by the long period swell, WEC devices in these regions will tend to have long operational periods to achieve natural resonance for optimal energy absorption. As the waves in these regions are directionally focused, the complexities and costs of weathervaning directionally-dependent WEC devices, e.g., attenuators, and even omnidirectional WEC farms, are significantly reduced. As previously mentioned, the energy distribution of the Hawaii coastal region has two separate peaks, around a peak period of 9s from the east and 14s from the northwest. WEC devices, therefore, may be designed to have a broadband response and weathervaning capabilities, or possibly two different narrowband WEC devices would be deployed, one to capture the energy in the short period swell band coming from easterly waves, and the other the long period swell coming from north-westerlies. Figure 3.4(d) indicates that short period swells contain the most energy for the East Coast. For the Gulf Coast, seas from the southeast direction having partition peak periods 6-7s, which correspond to local wind seas, contain the most energy. Therefore, the operational period of WEC devices for these regions would be relatively small compared to the West Coast. Further, because of the large range of peak directions for the energy content, weathervaning directionally dependent WEC devices, and associated costs would be greater. The most energetic sites are mainly located in the Alaska, Hawaii and the West Coast, with peak periods falling in the swell range (10-14s); although Hawaii also has a significant peak in the average wave power that corresponds to short period swell (7-10s).

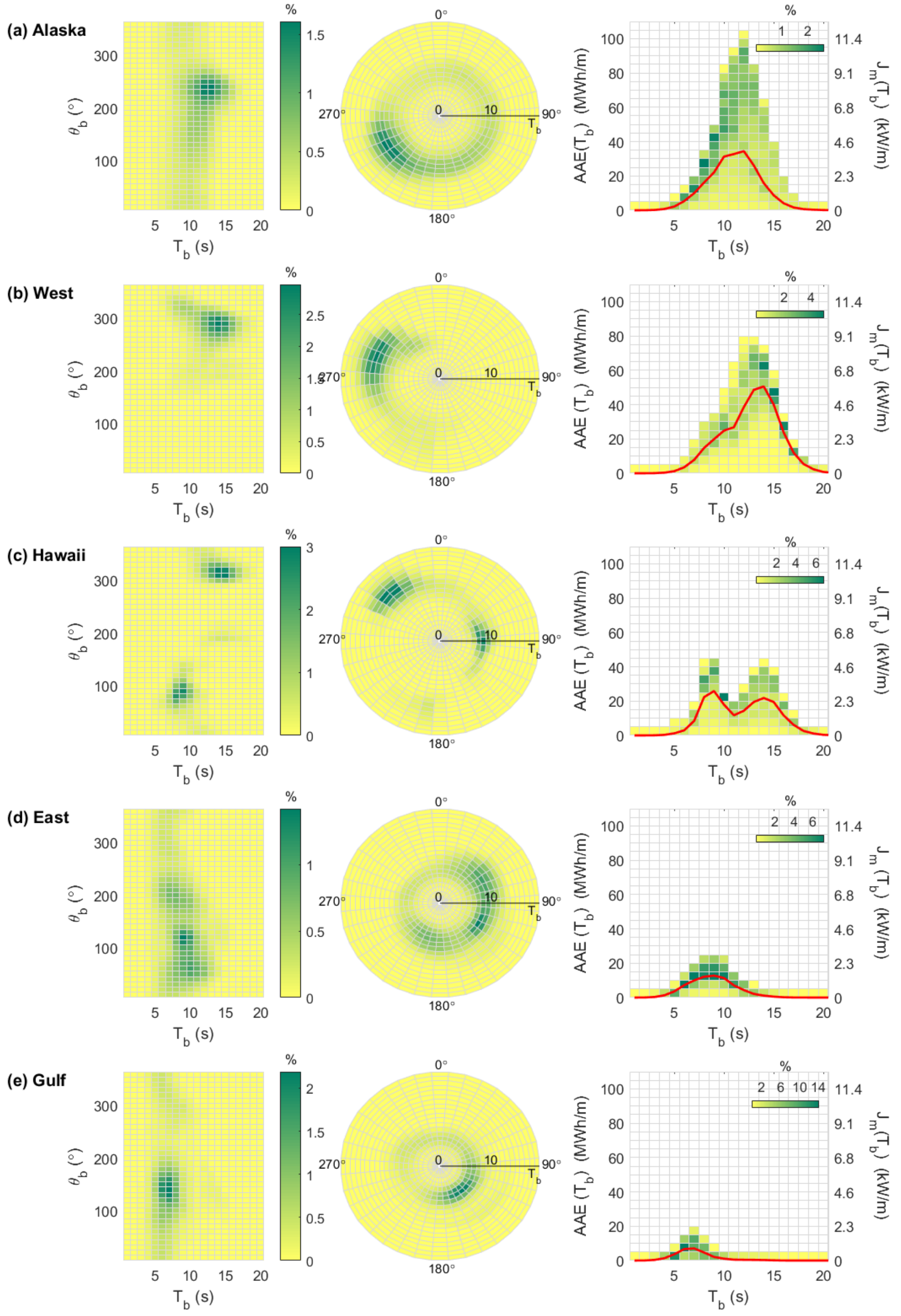

Figure 3.4. Regional percent contribution of wave power: (a) Alaska, (b) West Coast, (c) Hawaii, (d) East Coast, (e) Gulf Coast. Percent contributions of the 30-year averaged wave power for sea states in all US coastal waters; (left) percent contribution of the wave energy in terms of peak period partition and wave direction having a resolution of 1s and 10°, respectively. Colors indicate contributions to the total energy in %, (middle) plot (left) in polar coordinates, (right) percent contribution of the wave energy in terms of AAE (left y-axis) and wave power (right y-axis) and peak period partition. The resolution of the AAE

and wave power is 5 MWh/m and 0.57 kW/m, respectively. The red line indicates averaged wave power as a function of peak period partition.

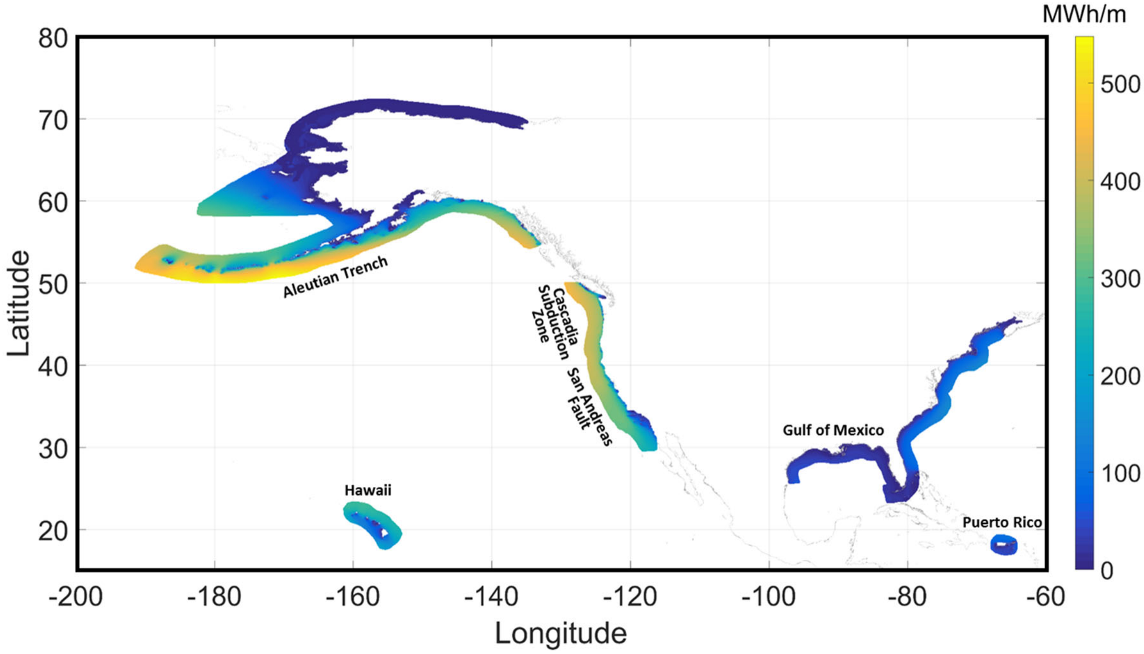

Figure 3.5. Geographic distribution of total AAE in MWh/m.

The geographical distribution of the total AAE is shown in Figure 3.5. The wave energy distribution is generally consistent with results from previous studies [26], [51]. As expected, the wave energy offshore is more energetic than nearshore. The largest energy, with AAE densities exceeding 400 MWh/m, is found along the Cascadia Subduction Zone located at Pacific Northwest Coast and along the Aleutian Trench. The California Coast near the San Andreas Fault has moderate energy compared to the Pacific Northwest Coast, on the order of 300 MWh/m. Hawaii has slightly lower energy potential compared to the West Coast, on the order of 200 MWh/m. The wave energy potential at the East Coast and Atlantic Ocean side of Puerto Rico is typically below 100 MWh/m. The smallest energy, with AAE below 50 MWh/m, along the US coastal waters except for arctic Alaska is found the Gulf of Mexico and Caribbean Sea side of Puerto Rico.

CHAPTER 4.

WAVE ENERGY RESOURCE PARAMETERS

In this chapter, alternative parameters, which are analogous to the IEC parameters, are proposed to characterize US wave energy resources by using spectral partitioned bulk wave data. Using the partitioned wave power, AAE spectral width, AAE-weighted period, AAE directionality coefficient, and direction of maximum directionally resolved AAE are calculated for the US coastal waters. The advantage of using the partition data to compute these parameters is that it better resolves the frequency and directional dependence of the wave energy resource using these alternative parameters. The physical meanings of the parameters are identical or similar to the IEC parameters because the full wave spectrum and partitioned wave power both represent energy distributions in terms of wave frequency and direction. However, these parameters require significantly less data compared to the IEC parameters facilitating our ability to characterize and map opportunities and constraints of wave energy resources for the entire US. In addition, an individual spectrum is represented by multiple realizations of each parameter, providing better resolution of the components of the sea state, such as individual parameters for swell and wind seas. In addition, we evaluate long-term AAE trends, and monthly and inter-annual variability using several parameters that quantify the temporal variability of the wave energy. Computing the temporal variability of the wave energy allows WEC developers to identify sites where the energy is more uniformly distributed throughout the year, as opposed to sites where the energy distribution follows more distinct seasonal trends. The geographical distributions of these resource metrics are provided and key features of each attribute are discussed.

4.1 Frequency dependence

As the wave energy generation can be maximized by resonating at the same period as incident waves, wave energy potential can be constrained by the technology's operational period bandwidth. Therefore, the frequency dependence of the wave energy is vitally important and a period band containing the largest energy content should be identified. In this study, two parameters, AAE-weighted period and AAE spectral width are computed to describe the frequency dependence of the wave energy. These parameters play a large role in driving selection of a WEC's operating period bandwidth and the WEC's optimal design size.

4.1.1 AAE-weighted period, T_{AAE}

Because of the importance of the frequency dependence for WECs, the AAE-weighted period, T_{AAE} indicating the period bandwidth containing the largest energy are computed. The energy-weighted period is weighted by the AAE, while the energy period, T_e used in IEC standard indicates the variance-weighted mean period.

$$T_{AAE} = \frac{\sum T_b \cdot AAE(T_b)}{AAE} \tag{4.1}$$

The geographical distribution of the AAE-weighted period and the AAE spectral width is shown in Figure 4.1. The spatial distribution of the AAE-weighted period is similar to the distribution of the total AAE and reveals distinct regional trends. Generally, long period swells ranging from 10 to 14s contain the largest energy for the Pacific Ocean Coast and intermediate period swell ranging from 8 to 10s contain the largest energy for the Atlantic Ocean Coast. For the Gulf of Mexico Coast, relatively short period wave systems, less than 8s, have the largest energy. These period regimes roughly correspond to long period swell, relatively short period swell, and local wind seas. The California coast has the largest T_{AAE} among the US coastal waters, requiring WECs deployed here to be commensurately the largest to achieve resonance and maximize energy generation.

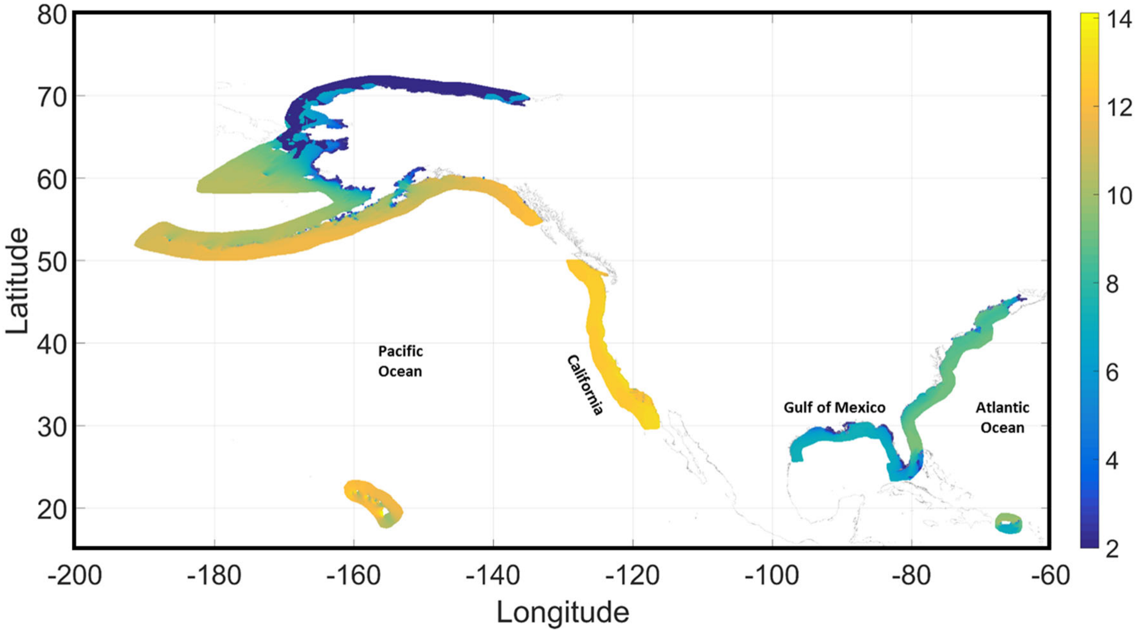

Figure 4.1. Geographic distribution of the AAE-weighted period, T_{AAE} in seconds, Eq. (4.1).

4.1.2 *AAE Spectral width, ϵ_{AAE}*

The spectral width recommended by IEC standard characterizes the relative frequency spreading of the energy spectrum which is measured by the standard deviation of the frequency variance density, normalized by the energy period [3]. Using the definition of the spectral width, relative spreading of the AAE along the peak period is calculated as the standard deviation of $AAE(T_b)$, normalized by the AAE-weighted period. A small value indicates a narrow frequency spread.

$$\epsilon_{AAE} = \sqrt{\frac{\sum {T_b}^2 \cdot AAE(T_b)}{AAE} - {T_{AAE}}^2} \Big/ T_{AAE} \tag{4.2}$$

The geographical distribution of the AAE spectral width is shown in Figure 4.2.

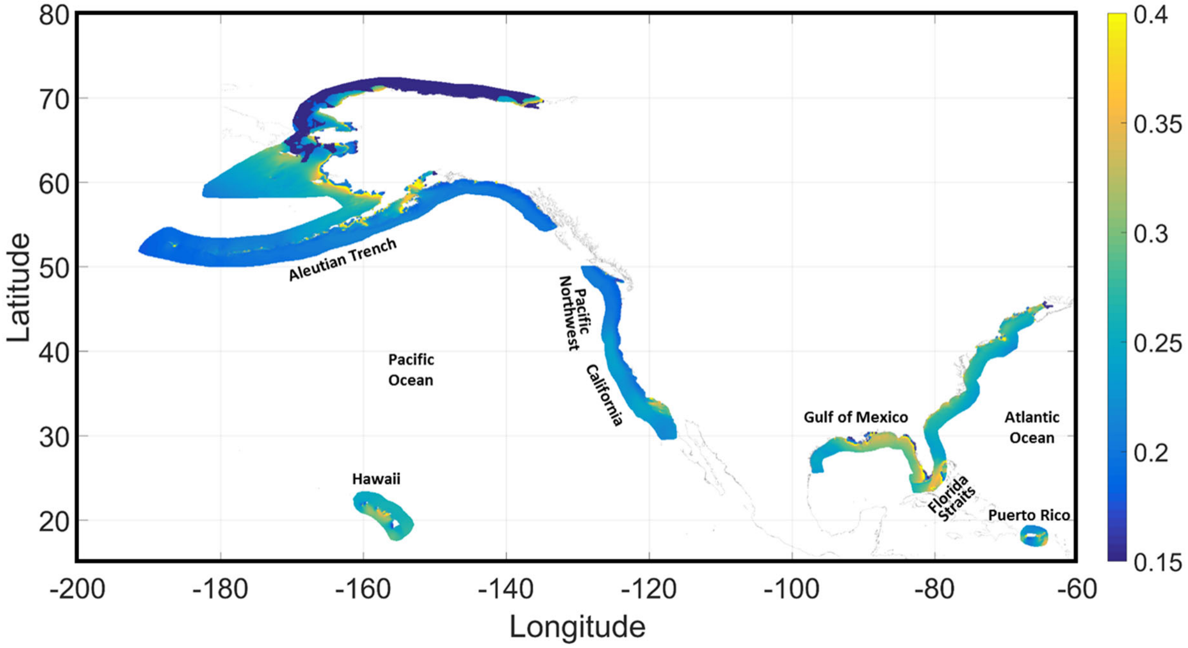

Figure 4.2. Geographic distribution of AAE spectral width, ϵ_{AAE} representing the standard deviation of $AAE(T_b)$ normalized by the total AAE, Eq. (4.2).

As shown in Figure 4.2, the distribution of the frequency spreading index, the AAE spectral width varies from 0.15~0.4 along the US coastal waters; the east coast of the Gulf of Mexico and Florida Straits have the largest values exceeding 0.3. The Pacific Ocean Coast generally has a narrow spectral width compared to the Atlantic Ocean Coast, except the Hawaiian Coast where the energy is distributed into two separate frequency peaks and has a relatively large spectral spreading [91]. Along the Hawaiian Coast, a narrow WEC operating frequency bandwidth may constrain the ability to generate a large amount of energy contained in the other peak. Notably, the Puerto Rico Coast has a relatively narrow AAE spectral width compare to the other portions of the Atlantic Coast. For the West Coast, the Pacific Northwest has a more narrow AAE spectral width compared to California. The narrow AAE spectral width along the Pacific Northwest Coast and the Alaska Trench permits an opportunity to reduce costs of wave energy generation by operating in a narrow period bandwidth.

4.2 Directional variability

As many WECs can only generate the energy contained within a narrow band of wave directions by aligning normal to the predominant wave direction, the directional variability of the wave energy may also be important. Therefore, the directional spread and the direction containing the largest energy need to be characterized. In order to characterize the directional variability, the directionally resolved $AAE(\alpha)$ passing through a vertical plane with normal vector in direction α, is calculated by adding each component of the $AAE(\theta)$ resolved in direction α. The parameter α has a resolution of $10°$ ranging from $0°$ to $180°$ clockwise from true North.

$$AAE(\alpha) = \sum AAE(\theta_b)|cos(\alpha - \theta_b)| \tag{4.3}$$

$AAE(\alpha)$ is similar to the directionally resolved wave power recommended from IEC standard. While the IEC parameter resolves only the positive-valued component [3], the term, $|cos(\alpha - \theta_b)|$, ensures that wave energy with positive and negative components in the direction of resolution contribute to $AAE(\alpha)$.

4.2.1 Direction of the maximum directionally resolved AAE, α_{max}

The maximum value of $AAE(\alpha)$, $max[AAE(\alpha)]$, represents the maximum directionally resolved AAE. For a WEC technology with a fixed orientation, the direction corresponding to the $max[AAE(\alpha)]$ is a measure of the characteristic direction that generates maximum energy. It is similar to the direction of maximum directionally resolved wave power, θ_{Jmax} [3].

$$\alpha_{max} = \alpha|_{max[AAE(\alpha)]} \tag{4.4}$$

While the AAE-weighted period describe the dominant frequency of the wave energy, the direction of maximum directionally resolved, AAE(α_{max}), characterize the dominant directions. The geographical distribution of the direction of maximum directionally resolved AAE is shown in Figure 4.3. In the Pacific Ocean Coast, the α_{max} are roughly consistent with directions of global wind climate, westerlies which are prevailing winds from the west toward the east in the latitudes between 30 and 60 degrees.

In the Gulf of Alaska, the α_{max} are consistent with directions of storms generated by the lower pressure systems that intensify in winter [92]. On the other hand, the α_{max} at the Atlantic Ocean Coast are similar to local wind directions. These different sources of the wave energy at the two coastal regions contribute the distinct frequency dependence, e.g., long period waves dominant in the Pacific Ocean Coast and short period waves dominant in the Atlantic Ocean Coast. The α_{max} can be used to determine the predominant wave-facing orientation of WECs, e.g., WECs facing west along the Pacific Northwest Coast and northwest along the California Coast.

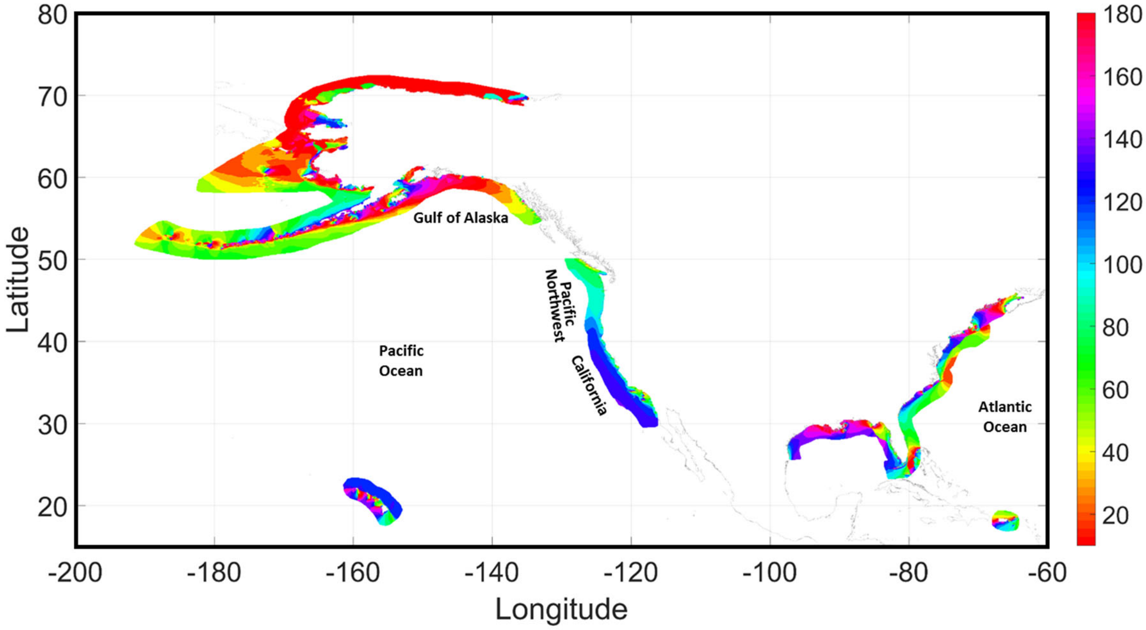

Figure 4.3. Geographic distribution of the direction of the maximum directionally resolved AAE, α_{max}, Eq. (4.4). The color indicates the clockwise direction from the North including both upstream and downstream direction.

4.2.2 *AAE directionality coefficient,* d_α

As a characteristic measure of directional spreading of wave power, IEC recommends the directionality coefficient d, the ratio of the maximum directionally resolved wave power to the total wave power. Using this definition, the ratio of the maximum directionally resolved AAE to the total AAE is calculated as

$$d_\alpha = \frac{\max[AAE(\alpha)]}{AAE} \tag{4.5}$$

A large d_α represents a narrow directional spread.

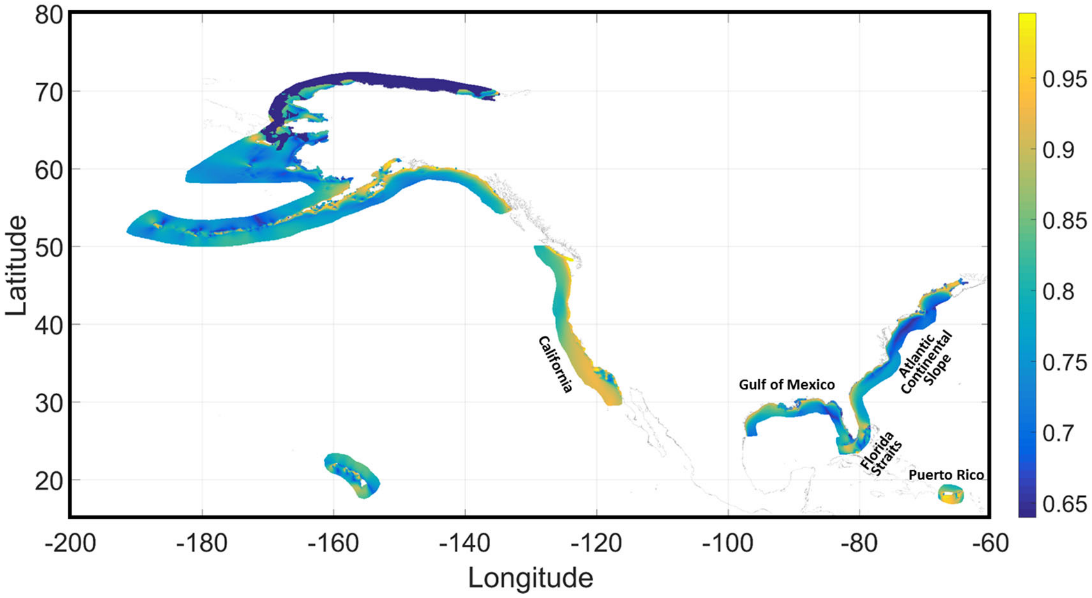

Figure 4.4. Geographic distribution of the AAE directionality coefficient, d_α, Eq. (4.5).

The geographical distribution of the AAE directionality coefficient, d_α, is shown in Figure 4.4. Unlike the AAE, where the waves in the offshore region have higher values than in the nearshore, the waves in the nearshore generally tend to have higher values of the d_α than those offshore. This result is consistent with wave refraction where the waves tend to become more shore normal as they approach the shore. Overall, the d_α along the nearshore is generally above 0.9. Further offshore the value ranges from 0.7 to 0.9 except off the California Coast and the Caribbean Sea side of Puerto Rico, where wave systems have a narrow directional spread and relatively high coefficients exceeding 0.9 are observed. As the waves in these regions are directionally focused, the complexities and costs of weathervaning directionally-dependent WECs, e.g., attenuators, and even omnidirectional WEC farms, can be reduced. Unusually, the waves in the nearshore have a smaller coefficient than in the offshore along the Atlantic Continental Slope and eastern Gulf of Mexico (Florida Shelter). This happens when the alongshore directed waves generated by local winds propagate over the steep slope which is perpendicular to the wave rays. The wave climates along the California Coast and the Caribbean Sea shore of Puerto Rico having the narrow directional spread are very attractive resource attributes for non-weathervaning directionally dependent WECs. Whereas, directionally independent WECs, e.g., point absorbers, or weathervaning directionally dependent WECs may be required at the northern Atlantic Coast to generate the wave energy from multiple directions.

4.3 Temporal variability

Another important factor to characterize the wave energy is the temporal variability for different time scales. Computing the temporal variability of the wave energy allows WEC developers to identify sites where the energy is spread more broadly throughout the year, a desirable resource attribute, as opposed to sites where the energy is concentrated within a particular season or year. As the WEC technologies advance, higher capacity factor, a ratio of actual energy produced to its rated full power over a specific time period [10], may be expected. The capacity factor is typically a function of the temporal variability of the wave energy resource and their strength [93]. The temporal variability index has been proposed using different time scales; daily, monthly, seasonally and inter-annually [27], [28], [50]. In this study, inter-annual variability, and seasonal variability, as well as a long-term trend of the wave energy, are calculated.

4.3.1 AAE long-term linear trend, S_{AAE}

In order to distinguish long-term trends AAE, a percent linear trends of $AAE(Y)$, the linear trends of $AAE(Y)$ normalized by the total AAE over the 30-year period, are calculated using a linear regression: $AAE(Y) = S_1 Y + S_2 + \varepsilon$. The regression coefficient, S_1 $(MWh/m \cdot year)$ is a slope of the linear trend of $AAE(Y)$ and the percent linear trends of $AAE(Y)$, S_{AAE} $(\%/year)$, is S_1 normalized by the total AAE.

$$S_{AAE} = \frac{S_1}{AAE} \times 100\% \tag{4.6}$$

S_2 and ε is an intercept and disturbance term, respectively.

In order to distinguish long-term regional trends AAE, the percent linear trends of AAE over the 30-year period are presented in Figure 4.5. This analysis shows that wave energy, as characterized by AAE, changed gradually over this period of record; decreasing by 0.25 to 1.0% per year over the majority of the US Coastal waters in the Pacific Ocean, and ± 0.5%/year along most of the East Coast. More pronounced rates of change are observed in northern segments along the Alaska Coast, the southern coast of California, and southern coastline segments of Puerto Rico and Hawaii, where wave energy decreased by over 1.0%/year; and northern segments along the Alaska Coast and the Gulf of Mexico where it increased by over 1.0%/year. Note that the percent linear trend is the percent change per year based on the 30-year averaged AAE. For example, the +1.0%/year means 1.0% of 30-year averaged AAE linearly increases over the 30-year period.

To illustrate the percent linear trends of AAE shown in Figure 4.5, the averaged inter-annual AAE at three sample areas and corresponding linear trends are plotted in Figure 4.6. In the sample area at California Coast, the inter-annual AAE is gradually decreased and the linear trend shows approximately 33 AAE drops over the 30 years. The percent linear trend in this area is -0.6%/year based on Eq. (4.6), which is comparable to the decrease in mean significant wave heights found by Young et al. [24]. Reguero at al. [50] found that a southward shifted and intensified Pacific jet stream generates waves from east to west at North Pacific and decreases the wave power that reaches the west coast of the US. According to Reguero et al. [94], mean wave power from 1985 to 2008 had been decreased approximately 1%/year at the North Pacific because contributions of swells from other ocean sub-basins are decreased. In the sample area at Northern Atlantic coast and Central Gulf of Mexico, the linear trend of inter-annual AAE increases by 6 MWh/year and 9 MWh/year over the 30 year period indicating +0.3%/year and +1.0%/year, respectively. These results are comparable to the 0.5% and 1.2% increase per year in the mean wave power founded by Reguero at al. [94]. The oceanic warming in the different basins increases global mean wave energy through the influence of sea surface temperature on wind patterns except the North Pacific [24], [50], [94].

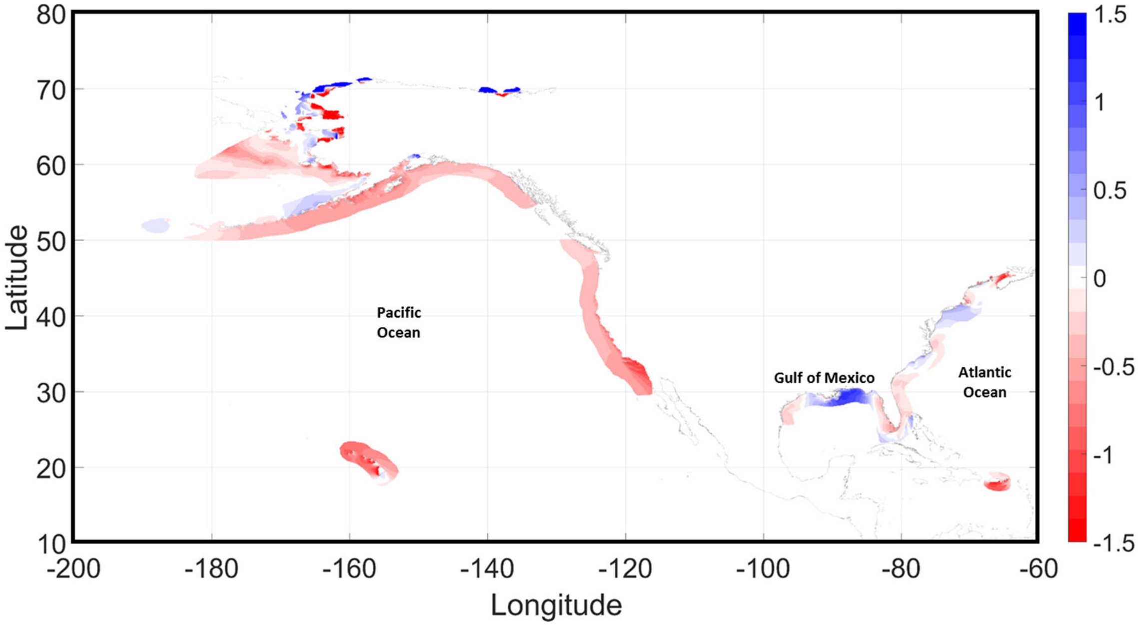

Figure 4.5. Geographic distribution of the long-term linear trends in AAE in percent per year. Eq. (4.6). Colors represent the S_{AAE} index.

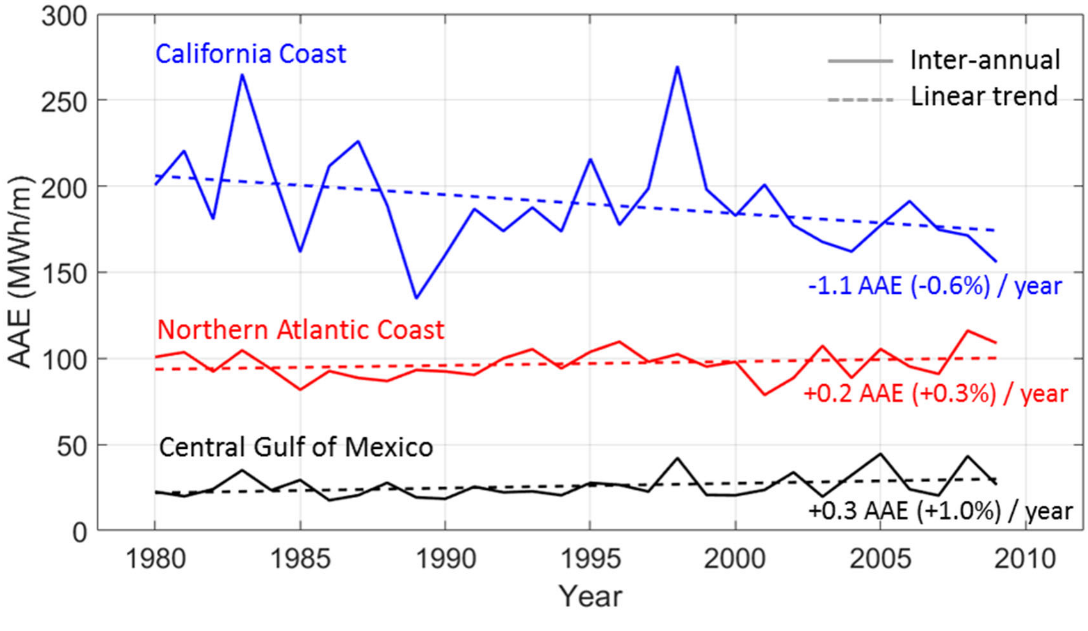

Figure 4.6. The averaged inter-annual AAE (solid line) at sample regions, California Coast (blue), Northern Atlantic Coast (red), Central Gulf of Mexico (black), and linear trend (dash line) over the 30-year period.

4.3.2 Inter-annual variability, t_i

In order to examine inter-annual variation driven by effects of global oscillations, e.g., El Niño, La Niña, the coefficient of variation [16,26] is calculated from the detrended $AAE(Y)$. To take into account the actual cyclical variations of the inter-annual wave energy, the linear trend of the $AAE(Y)$ is removed and the inter-annual variability is calculated as a standard deviation of the detrended $AAE(Y)$, divided by the 30-year mean AAE.

$$t_i = \frac{\sigma[AAE(Y) - (S_1 Y + S_2)]}{AAE} \times 100\ \% \tag{4.7}$$

Where σ denotes the standard deviation and $(S_1 Y + S_2)$ is the linear trend of $AAE(Y)$. A large t_i indicates that the wave energy has significant variability inter-annually.

The geographical distribution of the inter-annual variability of the AAE, t_i, is shown in Figure 4.7 as the coefficient of variation of the detrended AAE over the 30-year period. The t_i can represent the irregular inter-annual fluctuations of the wave energy driven by the El Niño Southern Oscillation (ENSO), which provides a steady source of baroclinic instability leading to convective energy. The largest oscillations, exceeding 25%, occur at the Bering Sea below the Alaskan Arctic region and the central-eastern Gulf of Mexico. Inter-annual variabilities of air, ocean and ice parameters at the Bering Sea has a strong cross-correlation with the southern correlation index (SOI), an index of ENSO [95]. The stronger influence of the subtropical jet stream generated by typical ENSO events impacts for the Southeast US, especially along the Gulf of Mexico coastline [96]. The southern California Coast (Channel Islands of California) and mid-Atlantic Coast (Cape Hatteras) have t_i above 15%. The Hawaiian Coast and northern Atlantic Coast have relatively small inter-annual variabilities among the US coastal waters below 10%.

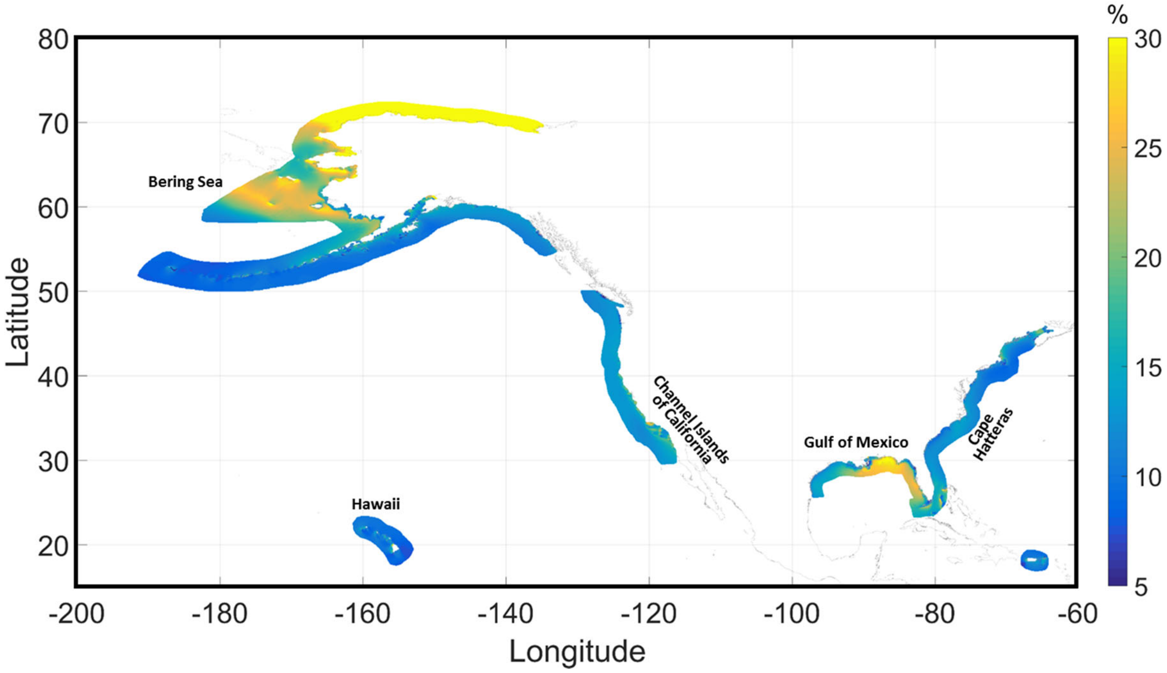

Figure 4.7. Geographic distribution of the inter-annual variability of AAE, Eq. (4.7). Colors represent the t_i index.

The inter-annual variability of wave energy climates should be considered in conjunction with predictions of the energy generation, WEC operation plans, and energy storage for long-term energy projects. The t_i directly results in different capacity factor, which measures how much average electricity a WEC device generates for project period relative to the electricity it can produce at the rated power during the same period [97]. Because the central-eastern Gulf of Mexico having a remarkably large t_i may have different wave energy climates depending on an inter-annual cycle, this region may be appropriate for relatively short term projects targeting energetic periods in the cycle to enhance the capacity factor. Long term projects are feasible with weathervaning frequency-independent WECs in this region, but it is not recommended due to the high operational and maintenance costs and low capacity factor. Due to the constancy of the inter-annual wave energy resource at Hawaiian Coast, a high capacity factor can be expected by optimizing the rated full power of a WEC device.

4.3.3 Seasonal variability, t_s

The seasonal variability, t_s indicates the maximum range of monthly mean energy relative to the annual mean energy [27].

$$t_s = \frac{[J_m(M) \cdot T_{30year}/T_{month}]_{max} - [J_m(M) \cdot T_{30year}/T_{month}]_{min}}{J_m} \tag{4.8}$$

Where $J_m(M)$ is the portion of 30-year averaged wave power in terms of month, and T_{month} is the number of hours in a particular month for 30-years. The $J_m(M) \cdot T_{30year}/T_{month}$ is the monthly mean wave power, thereby the first term in the numerator represents the mean wave power of the most energetic month and the second term is the mean wave power of the least energetic month. A large t_s indicates that the wave energy has significant variability throughout the year.

The geographical distribution of the seasonal variability (t_s) is shown in Figure 4.8. The Pacific Coast generally has a large value of seasonal variation compared to the Atlantic Coast and the Gulf of Mexico. In the nearshore arctic regions, the t_s is significantly large due to the effects of intermittent ice coverage. The largest t_s outside the arctic regions, on the order of 1.5, generally occur in Pacific Northwest Coast, the southern coast of Alaska and the northern coast of Hawaii, which means that the maximum range in monthly mean available energy is 1.5 times greater than AAE in these regions. The eastern Gulf of Mexico (Florida Shelters) also has a large value due to the extreme events. The California Coast has a relatively small monthly variation compared to the Pacific Northwest Coast, on the order of 1.0. Although the wave energy potential at the Pacific Northwest Coast is larger, the California Coast may offer better opportunities with its relatively more reliable and steady supply.

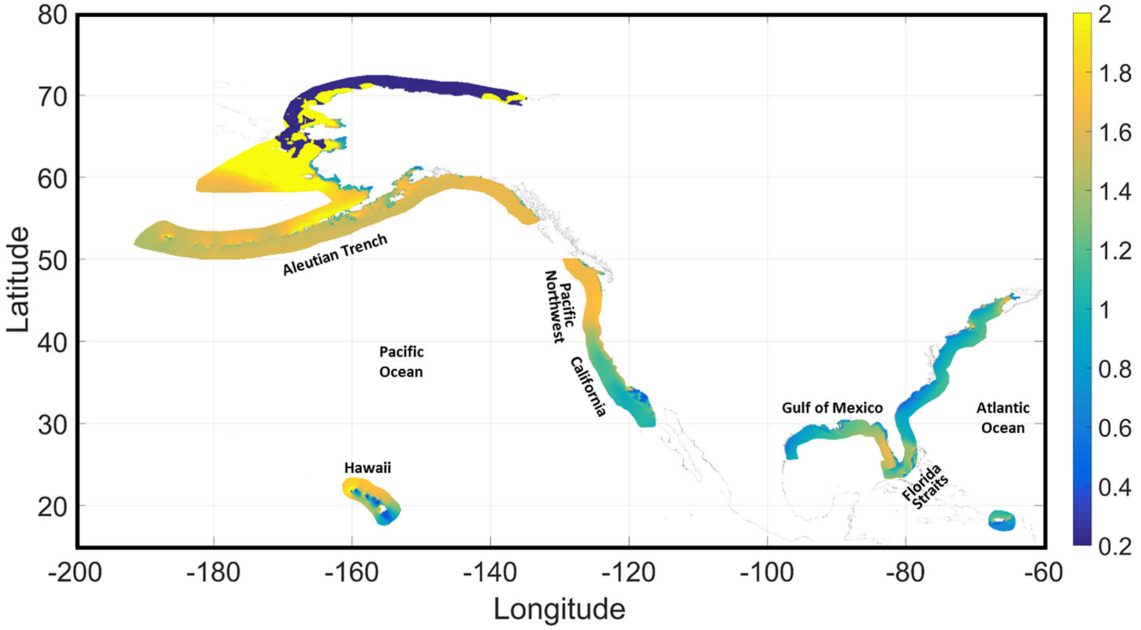

Figure 4.8. Geographic distribution of the monthly variability of AAE. Eq. (4.8). Colors represent the t_s index.

The t_s parameter can also be used as a measure to assess the annual average capacity factor or seasonal capacity factors [93]. The California Coast and Atlantic Coast, where the t_s is relatively small, may have large annual capacity factors and small variations of monthly capacity factors. On the other hand, the Pacific Northwest Coast and Hawaiian

Coast have relatively large fluctuations of seasonal capacity factors and it may require a capacity adjustable WEC technology to increase the capacity factor. As shown in Figure 4.7 and Figure 4.8, because the t_i and t_s tend to inversely proportional to each other in the Pacific Ocean, WEC projects need to optimize a WEC design depending on the project scale and period.

4.4 Summary

The wave energy resource within US coastal waters is characterized based on the wave energy potential, AAE, using spectral partitioned data generated from a 30-year WaveWatch III spectral wave model hindcast. Recognizing the importance of the frequency-directional dependence of WECs for maximizing energy generation, the AAE is calculated as a function of the peak period and wave direction. The frequency dependence and directional variability of the wave energy resources are characterized by describing the AAE-weighted period, AAE spectral width, direction of maximum directionally resolved AAE, and AAE directionality coefficient as well as the total energy potential. The AAE spectral width and AAE directionality coefficient represent the frequency and directional spreading of the AAE. The AAE-weighted period and direction of maximum directionally resolved AAE indicate the frequency and direction containing the largest energy. The temporal variability, inter-annual and seasonal (monthly) variations of wave energy, including the long-term linear trends, are also evaluated to characterize the constancy of the resource, which affects the capacity factor of a WEC project.

US wave energy climates having the greatest opportunities and least risks for energy generation exhibit high AAE and directionality coefficient as well as low spectral width and temporal variability. The Pacific Northwest Coast may be the most attractive region among the US coastal waters with the largest AAE, second largest directionality coefficient and smallest spectral width, on the order of 350MWh/m, 0.9 and 0.2, respectively. This means that the majority of the total wave energy in this region can be absorbed in a particular WEC operating period and direction. Although the California Coast has relatively small AAE compared to the Pacific Northwest Coast, on the order of 200 MWh/m, it is also a desirable region because of the largest directionality coefficient and relatively small seasonal variability. For utility-scale wave energy projects, these are highly promising regions especially when sites are close to population centers and industrial facilities. The promising wave energy resource attributes could lead to potentially lower costs of energy. Although the northern Hawaiian coast has considerable AAE, the actual wave energy generation in this region may be limited due to the relatively low resource qualities, e.g., a broad directional and frequency spreading. Although the wave energy potential for the Atlantic coast is relatively small compared to the Pacific Ocean coast, these regions may still be feasible for small-scale projects with relatively low temporal variabilities. The Caribbean shore of the Puerto Rico Coast, while having relatively less energy potential, has low frequency and directional spreading and low inter-annual and monthly variations, which, along with high energy costs, improves the opportunities and viability of wave energy projects.

CHAPTER 5.

WAVE ENERGY RESOURCE ASSESSMENTS AND CHARACTERISTICS

Wave energy regions are delineated along the US coastal waters based on the wave energy resource attributes, total wave energy potential, and corresponding resource parameters obtained from the Chapter 4, e.g., annual available energy (AAE), AAE directionality coefficient, AAE-weighted period, AAE spectral width, inter-annual and seasonal variability. The regional wave energy potential (AAE) is quantified by providing averaged marginal distributions of the wave energy in terms of the peak period, direction and month. In addition, secondary parameters which are used to assess the quality of the resource, such as spectral width, directional spread, seasonal variability of the joint wave energy distributions are characterized for each region. While the wave energy resource characteristics described in Chapter 4 are based on the same parameters, e.g., spectral width or directionality coefficient of the total wave energy resource, this chapter describes the regional characteristics of the joint distributions for these attributes, which are necessary to meet needs of WEC technologies. These more detailed assessments and characteristics of the wave energy resources allow WEC industries to select target wave systems for energy generations and WEC designs by providing the resource quality of all wave systems at each region. Finally, the portion of the energetic wave systems contributing to the total wave energy for each region is identified and characterized by providing the joint energy distributions and linking to the wind climatology [98], [99].

5.1 Delineating US wave energy regions

In order to discriminate the regional trend in wave energy resources, the six parameters discussed in Chapter 4, total annual available energy (AAE), AAE directionality coefficient (d_α), AAE-weighted period (T_{AAE}), AAE spectral width (ϵ), monthly variability (MV) and inter-annual variability $(COV)$are used to broadly delineate energy regions among the US coastal waters. As described in Chapter 4, the parameters are computed using the validated phase II 30-year hindcast from the 3rd generation (3G) spectral wave, WaveWatch III®(WWIII) having a spatial resolution of 4 arc minute [9]. The AAE is the annual available energy in MWh/m, analogous to annual energy production (AEP) without considering the energy conversion process. The directionality coefficient is a characteristic measure of directional spreading of AAE, the ratio of the maximum directionally resolved AAE to the total AAE. The AAE-weighted period is analogous to the energy period (T_e), the variance-weighted period of the frequency variance density spectrum. The spectral width characterizes the relative spreading of the energy along the frequency wave spectrum which is measured by the standard deviation of the frequency variance density, normalized by the energy period. The monthly variability indicates the maximum range of monthly mean energy relative to the yearly mean value. The inter-annual variability indicates global long-term oscillations of the AAE. The data are constrained by water depth ranging from 20m to 500m and 30-year averaged parameters along the confined coastal regions are considered to delineate the US coastal waters.

The US coastal waters are roughly distinguished in seven areas based on different oceans; northern and southern Alaska, the west coast, northern and southern Hawaiian coast, Gulf of Mexico, east coast and Puerto Rico. In this study, the west coast, Gulf of mexico, and east coast are divided into two sub-areas and the total eleven regions are delineated and shown in Figure 5.1. Note that the northern Arctic coast of Alaska has not been included due to the uncertainties of modeling with the frequent ice coverage. The energy regions for the west coast (R3 and R4), Gulf of mexico (R7 and R8), and east coast (R9 and R10) are divided based on maximizing the discontinuities in averaged AAE. For example, the averaged AAE are calculated for R3 and R4 regions by changing the boundary between the R3 and R4. The boundary resulting in the largest discrepancy in averaged AAE is determined. Each region has distinct values of averaged parameters as shown in Figure 5.2. The discrepancies of other averaged resource parameters shown in Figure 5.2 result from the delineation.

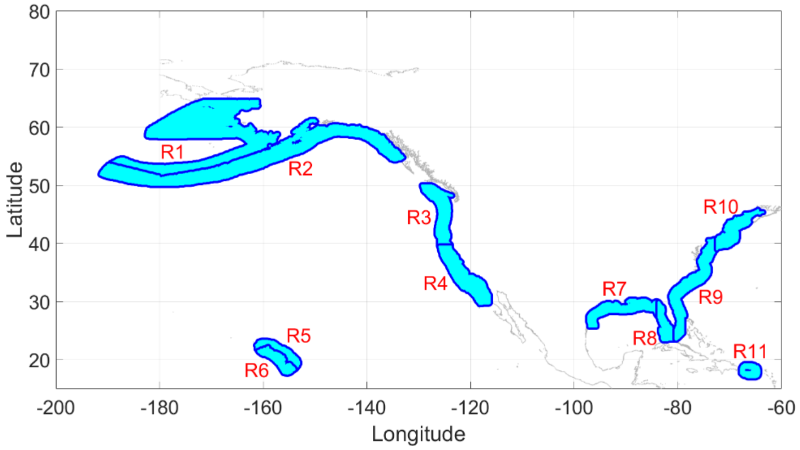

Figure 5.1. Eleven energy regions along the US coastal waters.

The Alaska coast, neglecting the arctic area, is divided into two regions: R1, near the Bering Sea where the intermittent ice coverage form in winter and the waves generated by Polar Easterlies and westerlies. R2, on the Pacific Ocean along the Aleutian Trench and Gulf of Alaska where the waves are generated by the westerlies. As seen in Figure 5.2, R1 has relatively less energy with large spectral width and high temporal variability compared to R2. Strong inter-annual variability in R1 is driven by the El Niño Southern Oscillation (ENSO) [95]. The west coast, the most energetic with largest AAE-weighted period among the US region, is also further divided into two regions differentiated by bathymetry and wind climates: R3, the Pacific Northwest Coast along the Cascadia subduction zone. R4, California Coast near the San Andreas Fault. R3 generally has more energy but high seasonal variability compared to R4. These two regions have different local wind trends and the discontinuity in the bathymetry formed by the two different geologies affect the wave climate, which will be discussed further in Chapter 5.2. The Hawaiian coast is also divided into two regions: R5 is on the northern side and R6 is on the southern side. R6 has trade winds from the Southern Hemisphere generating a portion of the swell. The most energetic sites for the Hawaiian coast are mainly located in R5 with relatively narrow spectral width and large seasonal variability compared to R6. In the Gulf of Mexico where the AAE and AAE-weighted period are smallest here among the US coast, the eastern Gulf of Mexico coast (West Florida Shelf) is defined as R8 and western and central Gulf of Mexico coasts are defined as R7. The wave energy potential in R8 is less than R7 because of the sheltering effect of Florida. R7 and R8 have largest inter-annual variabilities for the US coast due to the effects of the subtropical jet stream generated by typical ENSO events [96] and has a large seasonal variability due to extreme tropical cyclone events. The east coast is also divided into two regions and the boundary lies on the Hudson Canyon, the largest known ocean canyon off the east coast of the US, and one of the largest submarine canyon in the world: R9, below the canyon along the Mid-South Atlantic and Strait of Florida. R10, above the canyon along the North-Atlantic. Although the resource attributes in these regions are similar to each other, their local wind trends lead to different wave energy climate and will be discussed further in Chapter 5.2. Finally, R11 is defined along the Puerto Rico coast. This region is not divided into northern and southern sides because the wave energy for the southern side is relatively small. Interestingly, the wave systems in R11 have narrow directional spread and low inter-annual and seasonal variations. Detailed descriptions on the total AAE and corresponding attributes over the US coast are provided in Chapter 4. The key features of each region are summarized in Table 5.1.

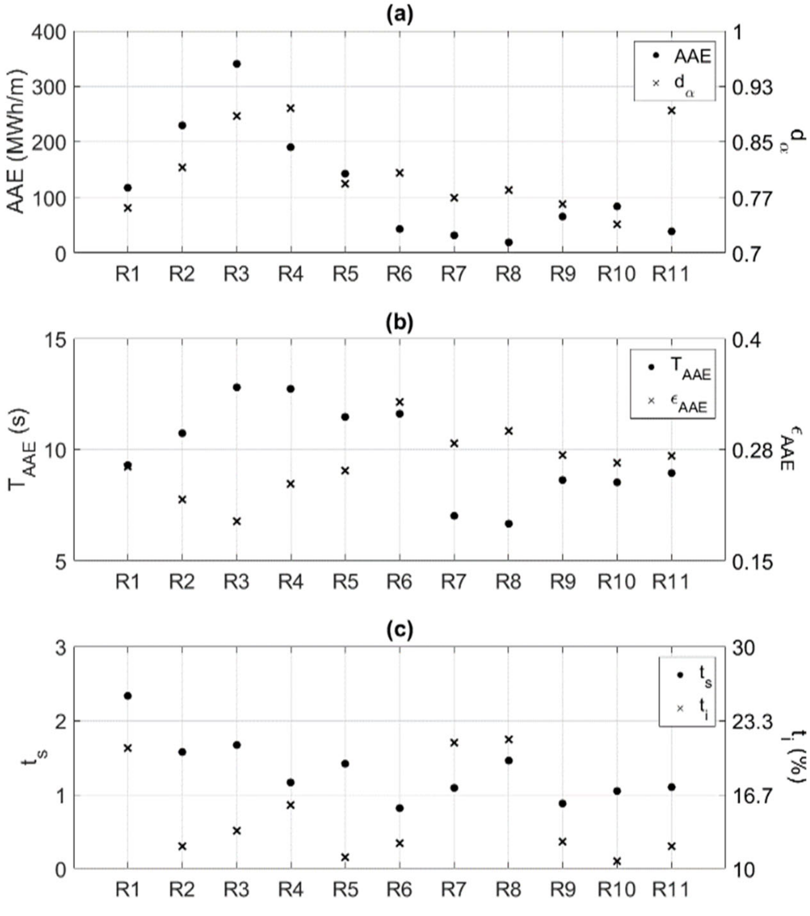

Figure 5.2. Averaged parameters across all locations within each region. (a) Total AAE (left y-axis) and directionality coefficient, d_α (right y-axis). (b) AAE-weighted period, T_{AAE}, (left y-axis) and spectral width, ϵ_{AAE} (right y-axis). (c) Seasonal variability, t_s (left y-axis) and inter-annual variability, t_i (right y-axis).

Table 5.1. Summary of key features for each energy region.

Region	Key Features
R1: Bering Sea	Ice covers, Polar Easterlies, Westerlies, ENSO effects
R2: Aleutian Trench, Gulf of Alaska	Westerlies, Storm
R3: Pacific Northwest Coast	Cascadia subduction zone, Westerlies
R4: California Coast	San Andreas Fault, Westerlies winds
R5: Hawaiian - Northern coast	Westerlies, Trade winds from Northern Hemisphere
R6: Hawaiian - Southern coast	Westerlies, Trade winds from both hemispheres
R7: Gulf of Mexico- Western,Central	Shelf, Tropical cyclones, ENSO effects
R8: Gulf of Mexico - Eastern	Florida Shelf, Tropical cyclones, ENSO effects
R9: Atlantic - South & Mid	Atlantic Continental Slope, Trade winds
R10:Atlantic - North	Trade winds from Horse Latitude
R11:Puerto Rico	Trade winds

5.2 Regional wave energy resource characteristics

Given the importance of period, directional, and temporal variabilities on the operation of WEC technologies, descriptions of the wave energy potential, AAE, and other resource parameters as a function of the peak period, direction, and month are useful. In order to gain unique wave energy resource characteristics, regional joint distributions giving the wave energy potentialities for any subset of the parameters conditional on particular values of the remaining parameters are presented in Figure 5.3 - Figure 5.13.

The $AAE(T_b, \theta_b, M)$ calculated in Chapter 4 for all the locations within a region are averaged together to create the averaged regional joint distributions. For example, the joint distribution as a function of period and direction bins is found by summing across all months using $AAE(T_b, \theta_b) = \sum_M AAE(T_b, \theta_b, M)$. This distribution is found in the top left panel of Figure 5.3. Similarly, the joint distribution for AAE as a function of month and direction is shown in the bottom left and the joint distribution as a function of month and period is shown in the top right panel. The three averaged marginal distributions, $AAE(T_b)$, $AAE(\theta_b)$ and $AAE(M)$ are shown in the middle of Figure 5.3. Note that a grand sum of each marginal or joint distribution is the total AAE within each region. These results illustrate how much wave energy potential is found for each sea state (AAE as a function of peak period and direction) as a function of the monthly temporal variation along with all interdependencies. The parameters which serve as resource variability indices for each site, $d_\alpha(T_b)$, $MV(T_b)$, $\epsilon_{AAE}(\theta_b)$, $MV(\theta_b)$, $d_\alpha(M)$, and $\epsilon_{AAE}(M)$ are calculated by applying the method described in Chapter 4 but using the marginal distributions, $AAE(T_B)$, $AAE(\theta_b)$, and $AAE(M)$. For example, $d_\alpha(T_b)$ is the directionality coefficient as a function of the peak period indicating the directional spreading of the wave energy within the particular period bands. In addition, the sources of the energetic wave systems are described by linking the local and global wind climatology, Scatterometer Climatology of Ocean Winds (SCOW) based on 10 years of QuikSCAT scatterometer data [98], [99]. Detailed descriptions of Figure 5.3 - Figure 5.13 are provided in Figure 5.3 caption.

5.2.1 Region 1- Bering Sea

The wave resource characteristics for the Bering Sea Coast are illustrated in Figure 5.3. As seen on the geographic map, the energetic sites in this region are mainly located along the Aleutian Islands and the offshore Bering Sea, on the order of 200 MWh/m. The inshore region of the Bering Sea has less energy, with the total AAE below 50 MWh/m, due to the intermittent ice coverage during winter. The overall seasonal variability is largest here (2.33) among the eleven regions. The overall directionality coefficient is relatively small (0.76) due to the multiple wave systems generated by the Polar Easterlies, Westerlies, and local wind.

Looking at the joint distributions together, during the summer months, the waves are generally local wind-sea (5-7s) mainly come from NNW to SE (340 to140^{o}). Short period swells (8-10s) are generated from all wave directions in fall and early winter. Long period swells (>11s) mainly come from SW (210-250^{o}) in fall and early winter. The three marginal distributions show that the short period swell (8-10s), the waves from SW (210-250^{o}), and early winter months contain the most energy. The t_s and d_α (green and red in $AAE(T_b)$) increase with increasing peak period and the most energetic period band, short period swell (8-10s), has moderate d_α and t_s, on the order of 0.7 and 2.5, respectively. The ϵ_{AAE} (blue in $AAE(\theta_b)$) is consistent for all wave directions, on the order of 0.2. The t_s (green in $AAE(\theta_b)$) is relatively small within the energetic wave directions and large for the other directions, on the order of 2.0. The d_α (red in $AAE(M)$) is consistent for all months, on the order of 0.7. The ϵ_{AAE} (blue in $AAE(M)$) is relatively small in summer and fall, on the order of 0.2.

This region can be divided into two areas: the west coast of Alaska where the latitude is larger than 55 and Northern side of the Aleutian Islands. The distinct wave systems are summarized and identified in the geographic map using arrow marks. The west coast of Alaska has three wave systems; the most energetic wave system (11-13s) coming from SW (210-240^{o}) in early winter, the wave system (8-9s) coming from SE (120-150^{o}) in early winter, the wave system (8-9s) coming from NNE (10-40^{o}) in early winter. The northern side of the Aleutian Islands has two wave systems: the most energetic wave system (11-13s) coming from W (260-290^{o}) in early winter, the wave system (9-10s) coming from NNE (20-50^{o}) in early winter. The energetic wave systems in this region are driven by westerlies prevailing winds from the west toward the east in the marginal sea of the Pacific in early winter. Inside the Bering Sea, local strong winds (Polar Easterlies), which are sources of the relatively short period waves, generally blow from the N and NE in winter.

This data can be used to evaluate the influence of the resource characteristics on WEC design. The large directional spreading of the wave systems may require an omnidirectional WEC technology for the waves from multiple directions to increase the capacity factor, potentially leading to an increase in the cost of energy in this region. For this region, targeting the omnidirectional WEC technologies with an idealized operating period of 9-10s would maximize the energy generation. The directionally dependent WEC technologies need to face SW with an idealized operating period of 12s. In addition, wave systems from SW have the smallest t_s in this region and facing SW would maximize the capacity factor of WEC devices.

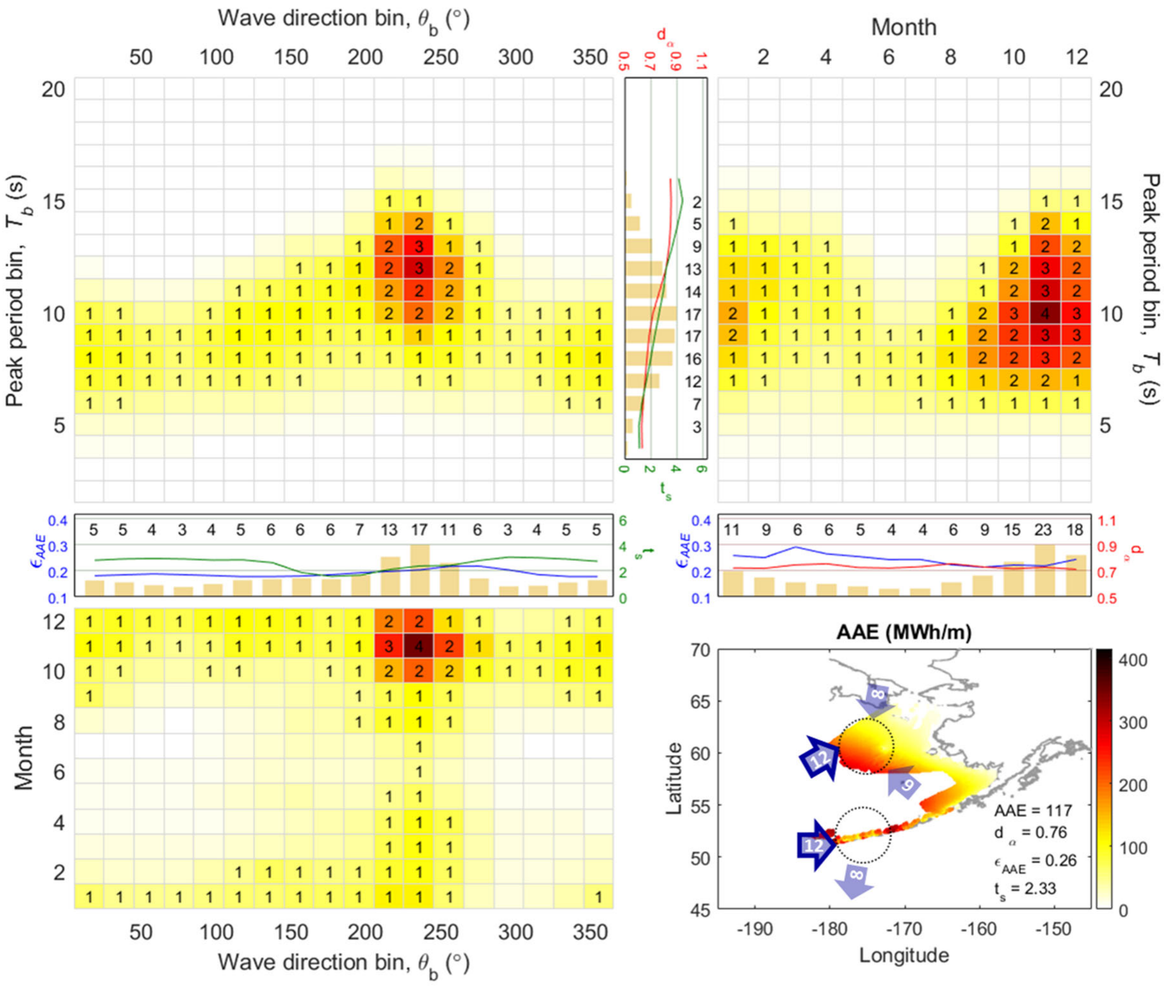

Figure 5.3. [Region 1 - Bering Sea] Averaged joint distributions, $AAE(T_b, \theta_b)$(top, left), $AAE(T_b, M)$(top, right), $AAE(M, \theta_b)$(bottom, left), and averaged marginal distributions, $AAE(T_b)$, $AAE(\theta_b)$, $AAE(M)$, with corresponding resource parameters, d_α(red line), t_s (green line), ϵ_{AAE}(blue line), and geographical distribution of the total AAE (bottom, right). Resolutions of T_b, θ_b, and M distributions are 1s, 20° clockwise from the true north and month, respectively. The numerals and colors in the joint and marginal distributions indicate the averaged AAE within particular wave systems, peak period, direction, and month. The arrows in the geographical distribution show energetic wave systems indicating the direction, peak period (numeral) and season (red: summer, blue: winter, grey: all year round) of each system. The arrow with a bold edge indicates the most energetic wave system. The average of total AAE and d_α, t_s, ϵ_{AAE} of the total AAE is also shown in the geographical distribution.

5.2.2 Region 2- Aleutian Trench and Gulf of Alaska

The wave resource characteristics for the Aleutian Trench and the Gulf of Alaska are illustrated in Figure 5.4. As seen on the geographic map, the energetic sites in this region are mainly located along the Aleutian trench and the offshore Gulf of Alaska, on the order of 300 MWh/m. The inshore of near the Aleutian Islands and the Gulf of Alaska has less energy, with total AAE below 100 MWh/m. The overall seasonal variability (1.58) is much smaller compared to the R1 (Bering Sea) due to ice formation. The overall directionality coefficient and spectral width are relatively large (0.82) and small (0.22) compared to the R1 due to the absence of the effects of the Polar Easterlies.

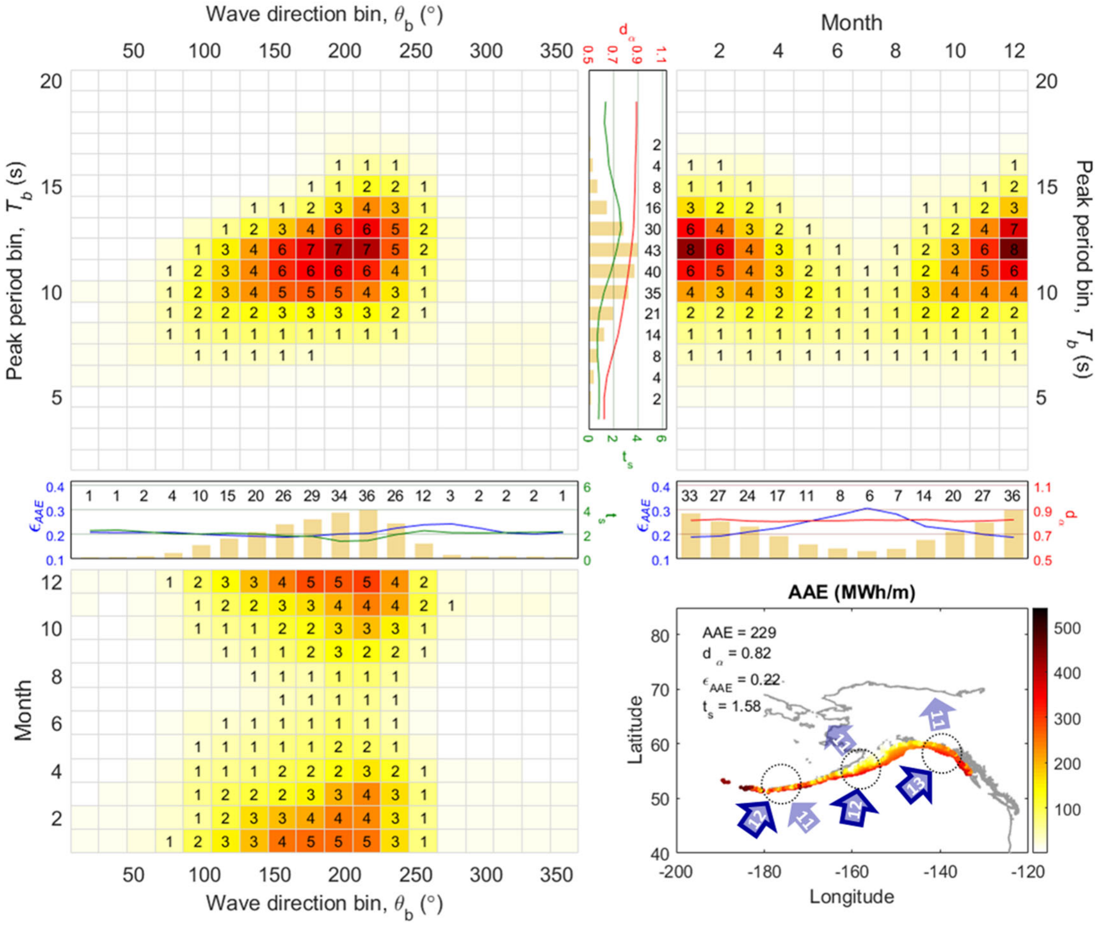

Figure 5.4. [Region 2 - Aleutian Trench and Gulf of Alaska] The detailed descriptions are identical to Figure 5.3.

Looking at the joint distributions together, local wind-sea (7s) mainly come from SE (100-170°) almost all year round. Short period swells (8-10s) are generated from S (130-220°) in winter. Moderate period swells (11-13s) mainly come from SSW (180-220°) in winter. Long period swells (>14s) come from SW (200-240°) in winter. The three marginal distributions show that the moderate period swell (11-12s), the waves from SSW, and winter months contain the most energy at each distribution. The d_α (red in $AAE(T_b)$) increase with increasing peak period and the t_s (green in $AAE(b)$) is relatively large at the energetic period, on the order of 2.5. The ϵ_{AAE} and t_s (blue and green in $AAE(\theta_b)$) are consistent for all wave directions, on the order of 0.2 and 2.0, respectively. The d_α (red in $AAE(M)$) is consistent for all months, on the order of 0.8. The ϵ_{AAE} (blue in $AAE(M)$) is small in winter, on the order of 0.2, and large in summer, on the order of 0.3.

The wave directions are smoothly shifted along the coastline due to the refraction. In order to describe the wave energy resource along the relatively long coastline, this region is divided into three areas; southern side of the Aleutian Islands, western Gulf of Alaska and eastern Gulf of Alaska. The wave systems are summarized and identified in the geographic map using arrow marks. The energy distribution of each area in this region generally has two swell systems: Swells (10-12s) in winter, Swells (12-13s) in winter. The more energetic wave system in each area comes from SSW (190-220°), S (170-200°), and SW (210-240°) and the other wave system come from SE (130-160°), SE (120-150°), and S (160-190°), respectively. The energetic swells are driven by westerlies from the WSW toward ENE in winter. In the Gulf of Alaska, storms caused by lower pressure in winter season generate the swell [92].

For this region, the operating period range of 11-12s may be recommended to maximize the energy generation and directionally dependent WEC technologies need to face SSW at the Aleutian Islands and western Gulf of Alaska, and SW at the eastern Gulf of Alaska. In general, wave systems from SSW have the smallest t_s in this region and facing SSW would maximize the capacity factor of WEC devices.

5.2.3 Region 3- Pacific Northwest Coast

The wave resource characteristics for the Pacific Northwest Coast are illustrated in Figure 5.5. As seen on the geographic map, the total AAE tends to increase with increasing latitude; energetic sites mainly located offshore of the Pacific Northwest Coast having power approximately 350 MWh/m. The inshore wave energy is weaker but still robust, on the order of 300 MWh/m. The overall spectral width is fairly small (0.19) and the overall directionality coefficient is fairly large (0.89), illustrating a high-quality energetic wave system with low frequency and directional variability.

Looking at the three joint distributions together, during the summer months, the waves are generally local wind-sea (7s) mainly come from NW (300-330^o). The short period swells (8-10s) come from SSW (200-230^o) in winter and from WNW (270-300^o) in summer. Longer period swells (>11s) are mainly generated from W (250-300^o) in winter. The three marginal distributions show that the long period swell (13-14s), the waves from W (250-300^o), and winter months contain the most energy for each distribution. The d_α (red in $AAE(T_b)$) is largest within the energetic period band, long period swell (13-14s), on the order of 0.9. The t_s (green in $AAE(T_b)$) is remarkably small for the short period swell band (8-10s), on the order of 1.0, due to the two comparable wave systems in both summer and winter. The ϵ_{AAE} (blue in $AAE(\theta_b)$ has a large fluctuation where the ϵ_{AAE} is smallest for the energetic directional band, on the order of 0.15. The ϵ_{AAE} (blue in $AAE(M)$) also has the large fluctuation where the ϵ_{AAE} is small in winter and large in summer. The d_α (red in $AAE(M)$) is relatively small in summer, on the order of 0.8.

The distinct wave systems are summarized and identified in the geographic map using arrow marks. The wave energy distribution in this region has four-wave systems: the most energetic wave system (13-14s) coming from W (260-290°) in winter, the wave system (9-11s) coming from SSW (200-230°) in winter and WNW (270-300°) in summer, the wave system (6-7s) with a little energy coming from NW (300-330°) in summer. The energetic swells are driven by westerlies from the WSW toward ENE in winter. The directions of local wind are seasonally changed. The local winds blow from NNW in summer and from SSW in winter. If constrained to a single wave system, a swell with 14s peak period from W (270°) in this region has the most dense wave energy resource, approximately 26 MWh/m, among the entire wave systems for the US coastal waters.

This data is also used to evaluate the influence of the resource characteristics on WEC design. The remarkably narrow directional and frequency spreading of the energetic wave systems potentially allows for a simplification of the device design for fewer frequencies/directions, potentially leading to a decrease in the cost of energy in this region. For this region, targeting WEC technologies with an idealized operating period of 13-14s would maximize the energy generation and a directionally dependent WEC technology needs to face W. A full rated power of a WEC technology may need to target the energetic wave systems in winter, thereby a capacity factor may be decreased in summer. Because the long period swells contain the most energy, WEC technology in this region will need to be relatively large to achieve natural resonance for optimal energy generation [100].

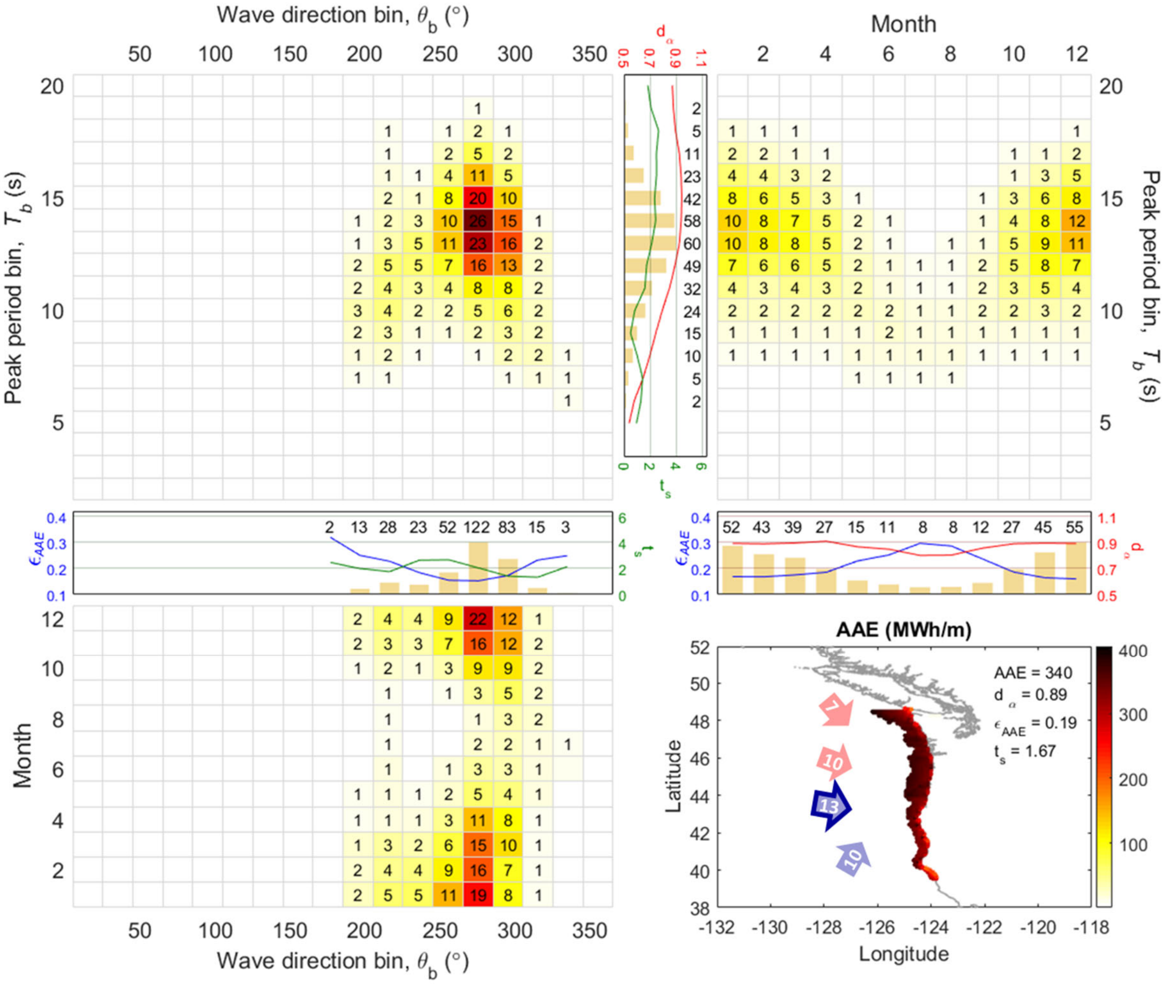

Figure 5.5. [Region 3 - Pacific Northwest Coast] The detailed descriptions are identical to Figure 5.3.

5.2.4 *Region 4- California Coast*

The wave resource characteristics for the California Coast are illustrated in Figure 5.6. As seen on the geographic map, the energetic sites are mainly located at the northern California Coast, on the order of 250 MWh/m. The total AAE in the Channel Islands located in the southern California Coast is remarkably less than the other sites, on the order of 50 MWh/m. The overall directionality coefficient is largest here (0.89) among the eleven regions and overall seasonal variability is relatively small (1.17) compared to the other regions located in the Pacific Ocean.

Looking at the joint distributions together, local wind-sea (<7s) is hardly observed in this region. Short period swells (8-10s) mainly come from WNW (270-320^{o}) in summer and long period swells (11-16s) mainly come from WNW (270-320^{o}) in winter. The three marginal distributions show that the long period swell (13-15s), the waves from WNW (270-300^{o}), and winter months contain the most energy for each distribution. The d_α (red in $AAE(T_b)$) is generally consistent, on the order of 0.9, except the longest period (17-19s) where the d_α is significantly small due to a combination of two comparable wave systems from different directions. The t_s (green in $AAE(T_b)$) is slightly large within the energetic period, on the order of 2.0. The ϵ_{AAE} (blue in $AAE(\theta_b)$) is smallest for the energetic directional band, on the order of 0.2. The ϵ_{AAE} (blue in $AAE(M)$) has a large fluctuation where the ϵ is small in winter and large in summer. The d_α (red in $AAE(M)$) is relatively small in summer, on the order of 0.8.

Like the R3 (Pacific Northwest Coast), the sites in this region also have a consistent wave energy distribution. The distinct wave systems are summarized and identified in the geographic map using arrow marks. The wave energy in this region can be characterized by three wave systems: the most energetic wave system (13-15s) coming from WNW (280-300^{o}) in winter, the wave system (8-10s) coming from WNW (290-310^{o}) in summer, the wave system (14-17s) with a little energy coming from SSW (190-220^{o}) almost all year round. The energetic swells are driven by westerlies from WSW toward ENE in winter.

The local wind direction in Pacific Northwest Coast has seasonality, while the local wind in this region blows from northwest throughout the year. This climatological discontinuity is located at the boundary between the two regions as well as the boundary between the Cascadia Subduction Zone and the San Andreas Fault. Interestingly, the local wind speed in this region is larger in summer than in winter [98]. Like other regions located near the Pacific Ocean, the westerlies from WSW direction in winter generate the energetic swell.

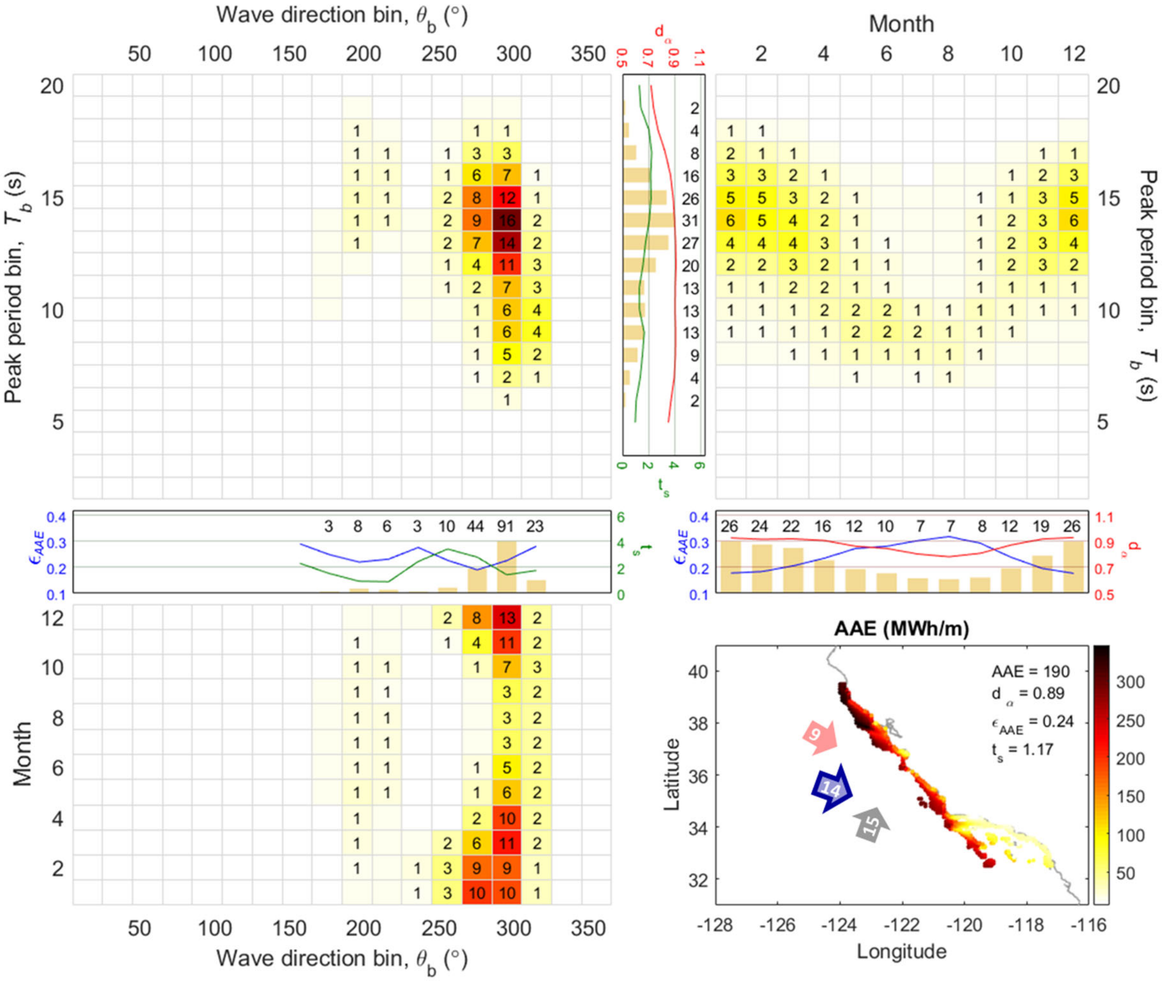

Figure 5.6. [Region 4 - California Coast] The detailed descriptions are identical to Figure 5.3.

In regards to WEC technology design requirements, the narrowest directional spreading of the energetic wave systems potentially allows for a simplification of the device design for fewer directions, potentially leading to a decrease in the cost of energy and the directionally dependent WEC technologies need to face WNW in this region. The operating period range of 13-15s may be recommended to maximize the energy generation for this region. Note that the energetic wave systems from WNW are distributed in a large period band over all year round, thereby adjustable operating period may contribute to increasing a capacity factor. Like the R3, WEC technology in this region will also need to be relatively large to achieve natural resonance for optimal energy generation [100].

5.2.5 Region 5- Hawaiian - northern coast

The wave resource characterizations for the northern Hawaiian coast are shown in Figure 5.7. As seen on the geographic map, the energetic sites are again mainly located offshore, on the order of 200 MWh/m. The overall directionality coefficient is relatively small (0.79) due to two comparable wave systems generated by westerlies and Trade winds. The wave system generated by the westerlies has long periods and the wave system generated by the Trade winds has relatively short periods. For this reason, the overall spectral width is relatively large (0.25) compared to the other regions located in the Pacific Ocean.

Looking at the joint distributions together, short period swells (8-10s) mainly come from ENE (60-100^{o}) almost all year round and long period swells (13-15s) mainly come from NNW (310-340^{o}) in winter. The marginal distributions have two comparable peaks in both peak period and wave direction. The d_α and t_s (red and green in $AAE(T_b)$) are large in the long period swells and relatively small in the short period swells. The ϵ (blue in $AAE(\theta_b)$) is large within the ENE (60-100^{o}) directional band and small for the NNW directional band. On the other hand, the t_s (green in $AAE(\theta)$) is small for the ENE (60-100°) directional band and large within the NNW (310-340°) directional band. The ϵ_{AAE} (blue in $AAE(M)$) is small in winter, on the order of 0.2, and large in summer, on the order of 0.25. The d_α (red in $AAE(M)$) is relatively small in summer, on the order of 0.7.

This region can be divided into three areas: west part (Kauai and Niihau), center (Oahu and Maui), and east part (Hawaii). As discussed above, the energy distribution in this region has two separate wave systems. Notably, sub-areas of this region have a different dominant peak between the two wave systems. The distinct wave systems are summarized and identified in the geographic map using arrow marks. The wave system (13-15s) from NNW (310-340°) contains the most energy in the west part and the wave system (8-10s) from ENE (60-100°) contains the most energy in the east part. Therefore, the wave energy at the west part is mainly distributed in winter and has a high value of t_s. The wave energy at the east part is distributed throughout the year with relatively low t_s. On the other hand, two wave systems equally contribute to the total energy in the center area. The wave system (8-10s) from ENE (60-100°) is generated by the Trade winds and wave system (13-15s) from NNW (310-340°) is generated by the westerlies from WNW traveling a long distance across the Pacific Ocean in winter.

The effect of the wave resource characteristics on the WEC technology varies for different sub-areas. In the western sub-area, an operating period range of 13-15s may be recommended to maximize the energy generation and directionally dependent WEC devices need to face NNW. Whereas, in the eastern sub-area, an operating period range of 8-10s may be recommended to maximize the energy generation and directionally dependent WEC devices need to face ENE. Because of the dominant longer period swell in the western sub-area, the WEC technology deployed there may need to be relatively large compared to the eastern sub-area. In addition, a low capacity factor in the western sub-area potentially leads to an increase in the cost of energy due to the large t_s. In the center sub-area, because both types of wave conditions exist with a high level of energy, a wave energy development project will need to select a target wave system based on the pros and cons of the two wave systems.

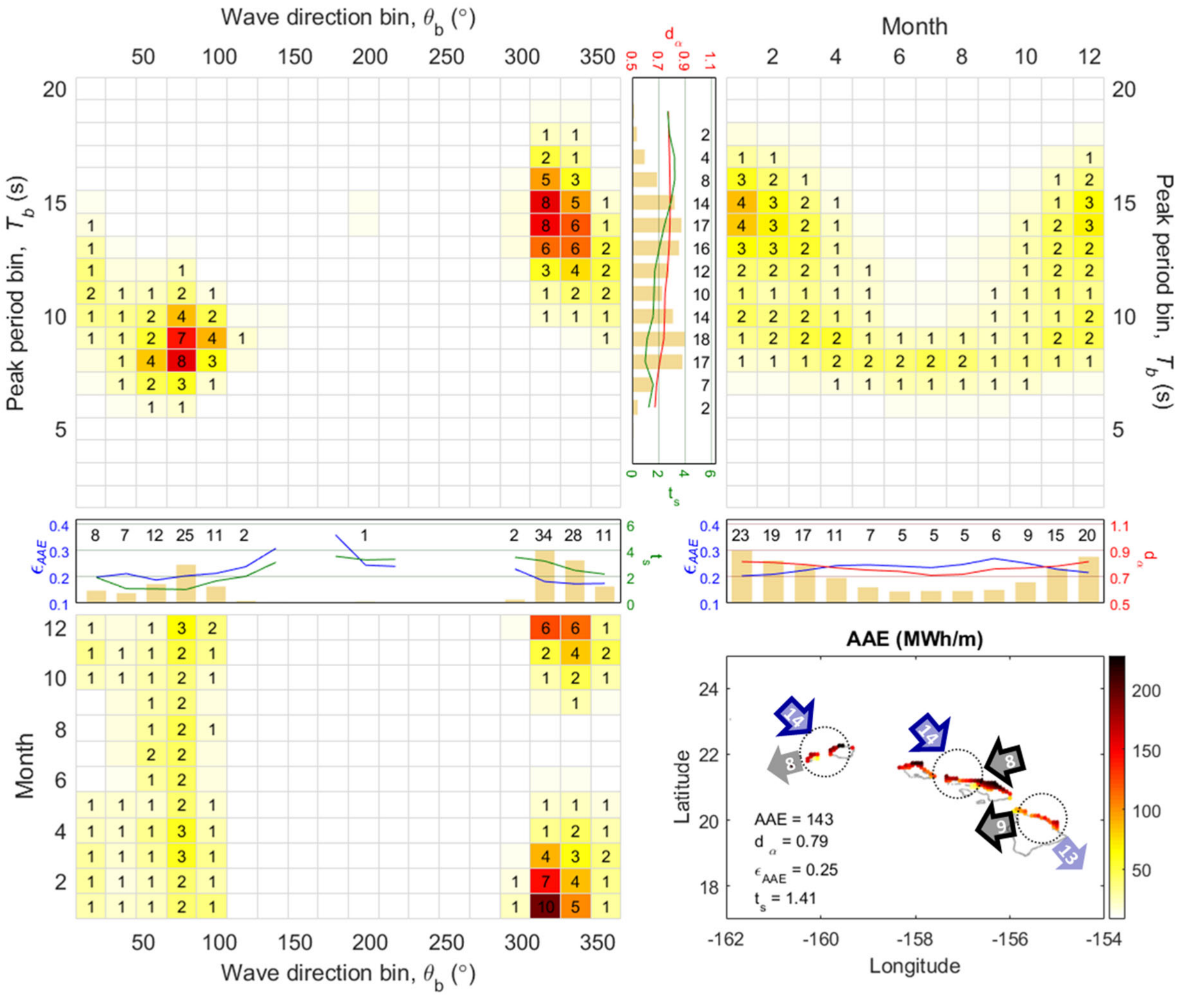

Figure 5.7. [Region 5 - Hawaiian - northern coast] The detailed descriptions are identical to Figure 5.3.

5.2.6 Region 6- Hawaiian - southern coast

The wave resource characteristics for the southern Hawaiian coast are illustrated in Figure 5.8. As seen on the geographic map, the energetic sites are mainly located between Oahu and Maui, on the order of 100MWh/m. Overall, the total AAE is relatively less compared to the R5 (northern Hawaiian coast). The overall spectral width is largest here (0.33) among the eleven energy regions due to three comparable wave systems generated by westerlies in the Northern Hemisphere and Trade winds in both hemisphere: The wave systems generated by the westerlies and Trade winds in the Southern Hemisphere have long periods and the wave system generated by the Trade winds in the Northern Hemisphere has a relatively short period. Because of different seasonalities of the three wave systems, the overall seasonal variability is smallest here (0.82) among the eleven energy regions. In addition, contributions to the total energy of the three wave systems are similar to each other.

Looking at the three joint distributions together, local wind wave and short period swells (<10s) mainly come from ENE (50-100°) almost all year round and long period swells (12-16s) mainly come from SSW (170-220°) in summer and NNW (300-350°) in winter. The marginal distributions in terms of the peak period and evenly distributed. The marginal distribution in terms of direction has three comparable peaks: from ENE (50-100°), SSW (170-220°), and NNW (300-350°). The d_α and t_s (red and green in $AAE(T_b)$) are consistent for all peak periods, on the order of 0.8 and 1.0, respectively. The ϵ_{AAE} of the energetic wave systems from SSW (170-220°) is remarkably small compared to the other directional band, on the order of 0.2. The t_s (green in $AAE(\theta_b)$) is small within ENE (50-100°) and SSW (170-220°) directional band and large for the NW (300-330°)

directional band. The d_α and ϵ_{AAE} (red and blue in $AAE(M)$) are consistent for all months, on the order of 0.8 and 0.3, respectively.

Notably, sub-areas of this region, same as defined in R5, have a consistent wave energy distribution like R3 (Pacific Northwest Coast) and R4 (California Coast). The distinct wave systems are summarized and identified in the geographic map using arrow marks. As discussed above, the energy distribution in this region has three separate wave systems which equally contribute to the total wave energy: the wave system (8-9s) coming from ENE almost all year round, the wave system (14-15s) coming from SSW (170-220°) in summer and NNW (300-350°) in winter. The two wave systems from NNW (300-350°) and ENE (50-100°) have a broader spectral width and large seasonal variabilities compared to the same wave systems in R5. Although the wave systems from ENE (50-100°) and NNW (300-350°) are generated by the trade winds and westerlies in the Northern Hemisphere, the wave energy in this region is less than R5 because these winds are weak on the leeward side. Long period swells are generated by the westerlies from WSW in winter and Southern Hemisphere Trade winds from SSW in summer.

Like R5, the wave energy development project will need to select a suitable WEC technologies or a target wave system due to the multiple wave systems having a different period band, directional and temporal variability. The sites located between Oahu and Maui can be considered as a potential project site and the operating period (13-15s) may be recommended to maximize the energy generation for these sub-areas. The combination of the two wave systems in this period band can supply consistent energy throughout the year. For directionally dependent WEC technologies, a seasonally adjustable deployment for front directions would be better to generate both wave systems and increase the capacity factor. If the WEC device needs a fixed front direction, the device front should face SSW because the wave system from SSW has the most narrow spectral width and moderate seasonal variability among the three wave systems. The wave system (8-9s) coming from ENE may still be viable for utility-scale projects that require a relatively small scale WEC device.

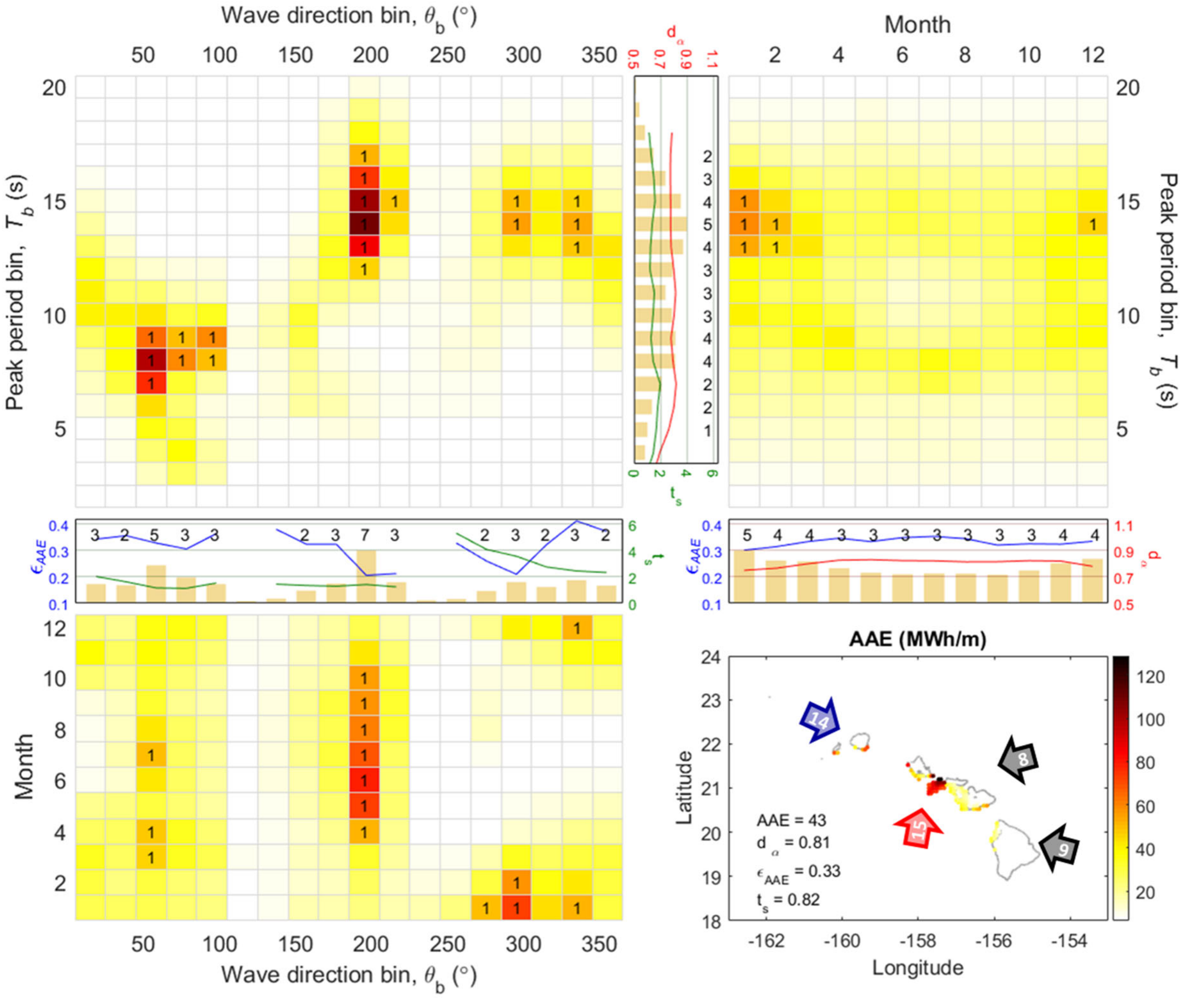

Figure 5.8. [Region 6 - Hawaiian - southern coast] The detailed descriptions are identical to Figure 5.3.

5.2.7 Region 7- Gulf of Mexico - western & central coast

The wave resource characteristics for the Gulf of Mexico (western & central coast) are illustrated in Figure 5.9. As seen on the geographic map, the energetic sites are mainly located in the western coast, on the order of 40 MWh/m. The central coast is sheltered by Florida and has relatively low energy, on the order of 20MWh/m. The overall resource parameters are generally moderate among the eleven regions.

Looking at the joint distributions together, during the winter months, the waves are generally local wind wave (<7s) mainly come from SE (120-160^{o}). The joints distribution in terms of the month and peak period has a wave system (12-15s), which are generated from tropical cyclones in late summer. The marginal distributions in terms of peak period and direction show that the local wind waves (6-7s), the waves from SE (120-160^{o}) contain the most energy, respectively. The marginal distribution in terms of the month shows that summer has relatively less energy. The d_{α} and t_s (red and green in $AAE(T_b)$) increase with increasing peak period. The t_s (green in $AAE(\theta_b)$) is smallest at the energetic directional band, on the order of 1.0. The ϵ (blue in $AAE(\theta_b)$) is largest at the energetic directional band, on the order of 0.25. The ϵ_{AAE} (blue in $AAE(M)$) has a large fluctuation where the ϵ_{AAE} is remarkably large in summer, on the order of 0.4. In summer season, kurtosis of the wave energy distribution in terms of the peak period would increase because the wave energy in wind sea and swell are comparable to each other. Especially in late summer, the spectral width is further increased due to the long period swell generated by the extreme events. The d_{α} (red in $AAE(M)$) is relatively small in winter, on the order of 0.7.

This region can be divided into two areas: western and central coast in the Gulf of Mexico. The wave systems are summarized and identified in the geographic map using arrow marks. Most energetic waves come from SE (110-160°) at the western coast and SSE (130-180°) at the central coast in late winter. The extreme events in late summer occur at the central coast. Local wind speed is stronger in winter than in summer and mean local wind direction in winter is ENE. However, the energetic wave systems are generated by the SE wind components in winter.

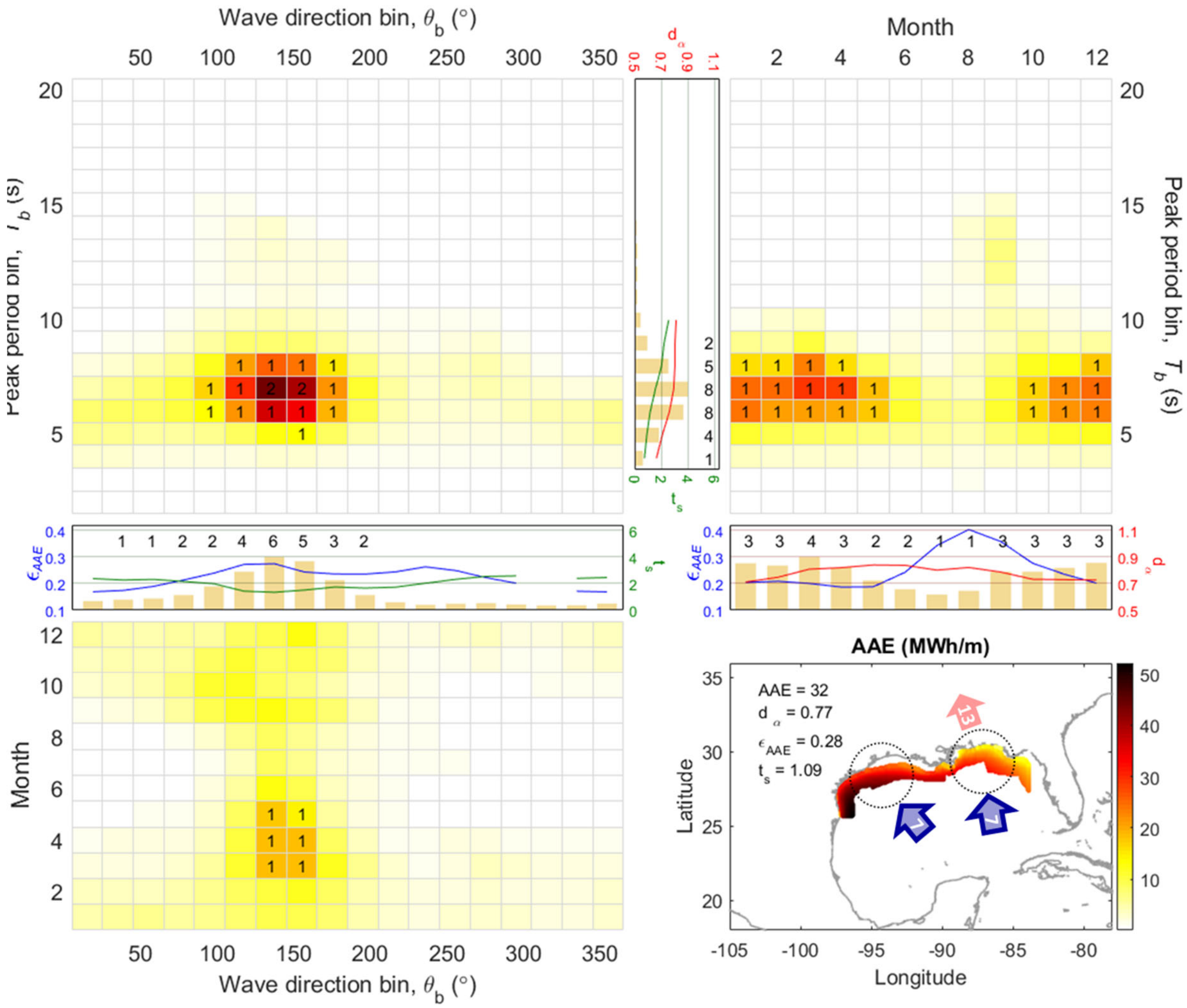

Figure 5.9. [Region 7 - Gulf of Mexico - western & central coast] The detailed descriptions are identical to Figure 5.3.

The sites located on the western coast can be considered as a small scale project due to the relatively small potential. For this region, targeting WEC technologies with an idealized operating period of 6-7s would maximize the energy capture. Therefore, the WEC technologies designed for this region would be relatively small to achieve natural resonance for optimal energy capture. The seasonal variability of the target wave system is relatively small, potentially leading to an increase of a capacity factor of the WEC device. A directionally dependent WEC technology needs to face SE. The central coast may have a risk to operation for survival due to extreme events.

5.2.8 *Region 8- Gulf of Mexico - eastern coast*

The wave resource characteristics for the Gulf of Mexico (eastern coast) are illustrated in Figure 5.10. As seen on the geographic map, the energetic sites are mainly located in a corner between the offshore Florida Shelf and southern coast of Florida, on the order of 30 MWh/m. The southern coast of Florida has relatively low energy, on the order of 10 MWh/m. The overall resource parameters are slightly larger than the R7 (western and central Gulf of Mexico).

Looking at the joint distributions together, local wind wave (<6s) mainly come from ESE (80-130^{o}) almost all year round and short period swells (7-9s) mainly come from WNW (280-330^{o}) in winter. The three marginal distributions show that the local wind waves (5-7s), the waves from WNW (280-330^{o}), and winter months contain the most energy for each distribution. The t_s (green in $AAE(T_b)$) increase with increasing peak period. The d_α (red in $AAE(T_b)$) is largest within the short period swells (7-9s), on the order of 0.8. The t_s (green in $AAE(\theta_b)$) is smallest for the ESE (90-120^{o}) directional band, on the order of 1.0, and largest within the WNW (280-320^o) directional band, on the order of 2.5. The ϵ_{AAE} (blue in $AAE(\theta)$) is smallest for the two energetic directional bands, on the order of 0.2. Like the R7, the ϵ_{AAE} (blue in $AAE(M)$) has a large fluctuation where the ϵ_{AAE} is remarkably large in summer, on the order of 0.4. Unlike the R7, the d_α (red in $AAE(M)$) is relatively small in summer, on the order of 0.7.

This region can be divided into three areas: Florida Shelf, southern coast of Florida and a corner between the two areas containing the Florida Keys. The wave systems are summarized and identified in the geographic map using arrow marks. The joint distribution in terms of the peak period and wave directions has two separate wave systems contributing to different sub-areas: Most of the energy in the Florida Shelf is dominated by the wave system (7-9s) coming from WNW (280-330^o) in winter. Most of the energy in the southern coast of Florida is dominated by the wave system (5-6s) coming from ESE (90-120^o) almost all year round. The corner area has both wave systems where the energy is mainly dominated by the wave system (7-9s) from WNW in winter. Although the mean direction of the winds at the Florida Shelf is NNE in winter, the energetic wave system is generated by the NNW wind components. In the south coast of Florida, winds from ENE generate the wind-seas almost all year round.

The corner area with the Florida Keys can be considered as a small scale project by targeting two wave systems, which are in opposite directions. For this sub-area, the operating period (5-8s) may be recommended to maximize the energy generation and a directionally dependent WEC technology needs to face WNW or ESE. For the corner area and southern coast of Florida, an energy project targeting wave systems for the short period (5s) can expect a relatively small size WEC technology with a high capacity factor. This compact and high-efficiency project can be merged with the other renewable energy resource projects, e.g., wind energy, ocean current energy, in these sub-areas. However, these areas may have a risk to operation or survival due to the strong Gulf Stream currents.

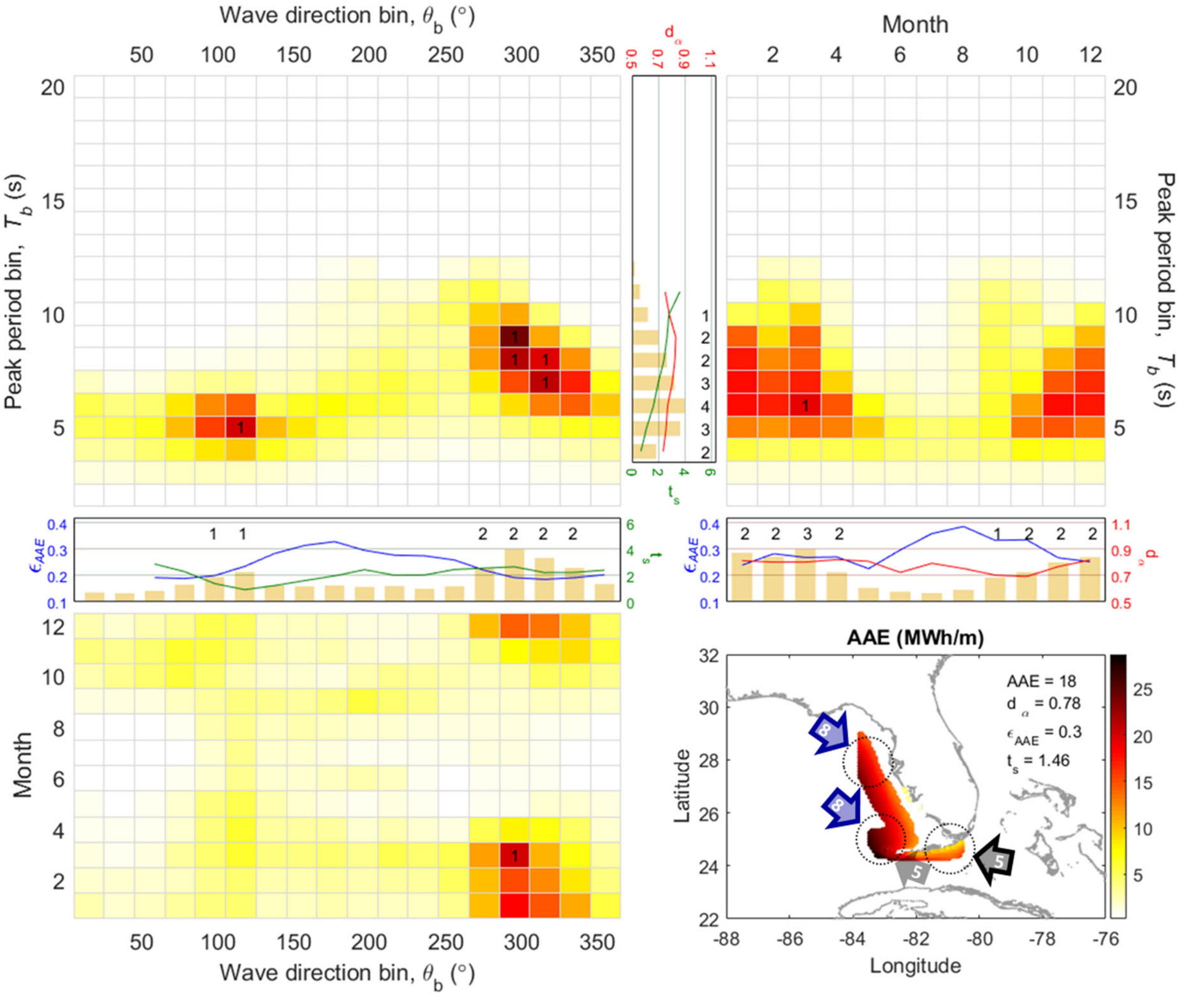

Figure 5.10. [Region 8 - Gulf of Mexico - eastern coast] The detailed descriptions are identical to Figure 5.3.

5.2.9 Region 9- Atlantic - South & Mid coast

The wave resource characteristics for the Atlantic (South and Mid coast) are illustrated in Figure 5.11. As seen on the geographic map, the energetic sites are mainly located at South and Mid-Atlantic offshore coast, on the order of 100 MWh/m. A submarine canyon between Florida and Bahama has low wave energy, on the order of 20 MWh/m. The overall directionality coefficient is relatively small (0.77) compared to other regions because the along-shelf waves, as well as the cross-shelf waves, contribute largely to the total energy. The overall seasonal variability is the second smallest here (0.88) among the eleven regions.

Looking at the joint distributions together, short period swells (8-10s) mainly come from ENE (50-100^{o}) in winter and ESE (90-140^{o}) in summer. Like the R7 (western and central Gulf of Mexico), the joints distribution in terms of the month and peak period has a little energy of wave system (14-15s) generated by the tropical cyclones in summer. The three marginal distributions show that the short period swell (8-10s), the waves from E (80-120^{o}) and winter contain the most energy for each distribution. The t_s (green in $AAE(T_b)$) is generally consistent, on the order of 1.0, except the long period swell with t_s exceeding 4.0. The d_α (red in $AAE(T_b)$) increase with increasing peak period where the d_α in the energetic period is on the order of 0.8. The t_s (green in $AAE(\theta_b)$) is smallest at the ESE (110-130^{o}) directional band, on the order of 1.0. The ϵ (blue in $AAE(\theta_b)$) is consistent over the energetic directional band, on the order of 0.2. Like the R7 and R8 (eastern Gulf of Mexico), the ϵ_{AAE} (blue in $AAE(M)$) is large in summer, on the order of 0.3.

This region can be divided into two areas: the South and Mid-Atlantic and the submarine canyon between Florida and Bahama. The wave systems are summarized and identified in the geographic map using arrow marks. In the submarine canyon, the wave energy is dominated by the wave systems (8-10s) from NE (40-70^{o}) in winter. The South and Mid-Atlantic coast have three wave systems: the most energetic wave system (9-11s) from ENE (60-100°) in winter, the wave system (8-10s) from ESE (90-140°) in summer, the wave system (7-8s) from S (170-210°) almost all year round. Local wind speed is stronger in winter than in summer and winter winds coming from NNE generate the short period swell as well as the wind-sea. The wave system in summer is generated by the trade winds just below the Horse Latitudes which are subtropical latitudes between 30-38 degrees.

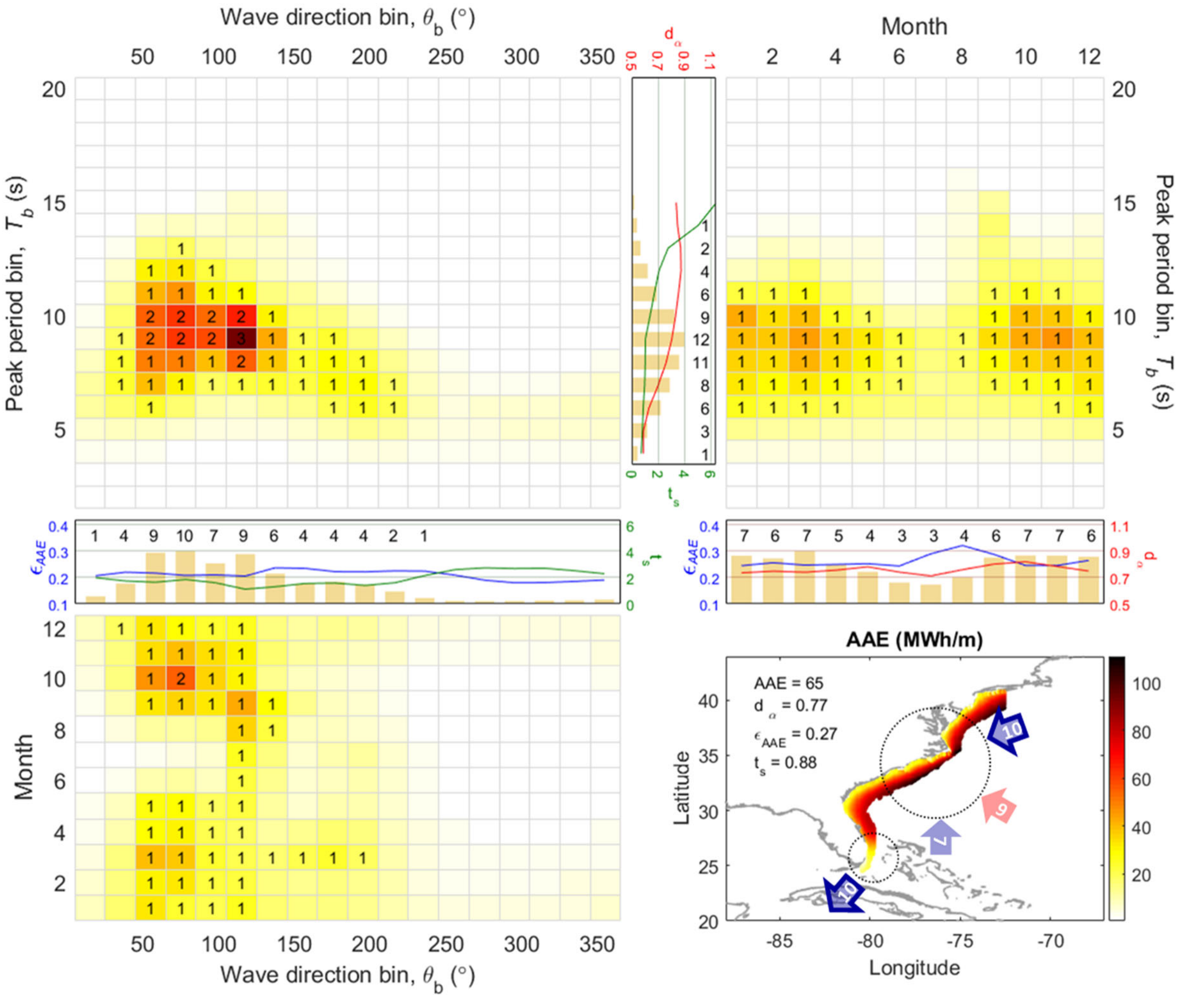

Figure 5.11. [Region 9 - Atlantic - South & Mid coast] The detailed descriptions are identical to Figure 5.3.

In regards to the design of WEC technology, the operating cost associated with the directionally dependent WEC technologies would be greater for this region because of the relatively small directionality coefficient. Instead, high capacity factors may be expected due to remarkably small t_s. The operating period (8-10s) may be recommended to maximize the energy generation and a device front needs to face E for the directionally dependent WEC technologies. Like R8, the energy projects in this region can also be merged with other ocean renewable resources because the energetic wave system, which requires a relatively small design is parallel with the local winds and ocean currents in this region. However, the energetic sites in this region may have a risk to operation or survival due to the strong Gulf Stream currents.

5.2.10 Region 10- Atlantic - North coast

The wave resource characteristics for the Atlantic (North coast) are illustrated in Figure 5.12. As seen on the geographic map, the energetic sites are mainly located at the north-Atlantic offshore coast, on the order of 150 MWh/m. It is clearly seen that the further sites are away from the coastline, the larger the wave energy. The overall directionality coefficient is smallest here (0.74) among the eleven regions because the along-shelf waves, as well as the cross-shelf waves, contribute significantly to the total energy. The overall seasonal variability is relatively small (1.05) compared to other regions.

Looking at the joint distributions together, during the winter months, the waves are generally local wind seas (<7s) mainly come from SWS (180-220^{o}) and W (250-300^{o}). Swells (8-11s) mainly come from a wave direction band ranging from E to S (70-200^{o}) in winter. Like the R7 (western and central Gulf of Mexico) and R9 (South and Mid-Atlantic), the joints distribution in terms of the month and peak period has a little energy of wave system (14-15s) generated by the tropical cyclones in summer. The three marginal distributions show that the short period swell (7-10s), the waves from SWS (180-220°), and winter months contain the most energy for each distribution. The t_s (green in $AAE(T_b)$) increase with increasing peak period where the t_s in the energetic period is on the order of 1.0. Although the overall d_α is smallest here among the eleven regions, d_α (red in $AAE(T_b)$) is relatively large in the energetic period, on the order of 0.8. The t_s (green in $AAE(\theta_b)$) is smallest within the energetic directional band ranging from SE to SWS (130-220°), on the order of 1.0. The other directional bands have a relatively large t_s, on the order of 2.0. The ϵ_{AAE} (blue in $AAE(\theta_b)$) is consistent over the energetic directional band, on the order of 0.2. Like the R7-9, the ϵ (blue in $AAE(M)$) is large in summer exceeding 0.3. The d_α (red in $AAE(\theta_b)$) is consistent for all wave directions, on the order of 0.7.

Similar to the R3 (Pacific Northwest Coast), R4 (California Coast), and R6 (southern Hawaiian Coast), the sites in this region also have a consistent wave energy distribution. The wave systems are summarized and identified in the geographic map using arrow marks. Most sites have two comparable wave systems coming from SWS (180-220°) and SE (110-150°) direction with a peak period ranging from 7 to 11s in winter. Unlike the R9, winter winds coming from S which is opposite to R9 generate the short period swell as well as the wind-sea. The source of the swell from SE (110-150°) is the trade winds just below the Horse Latitude.

The operating cost associated with the directionally dependent WEC technologies would be greater for this region because of the relatively small directionality coefficient derived from two comparable wave systems. Although the two wave systems are more energetic in winter than in summer, they contain considerable energy in summer, which may increase the capacity factor in this region. The operating period (8-10s) may be recommended to maximize the energy generation and a device front needs to face S for the directionally dependent WEC technologies.

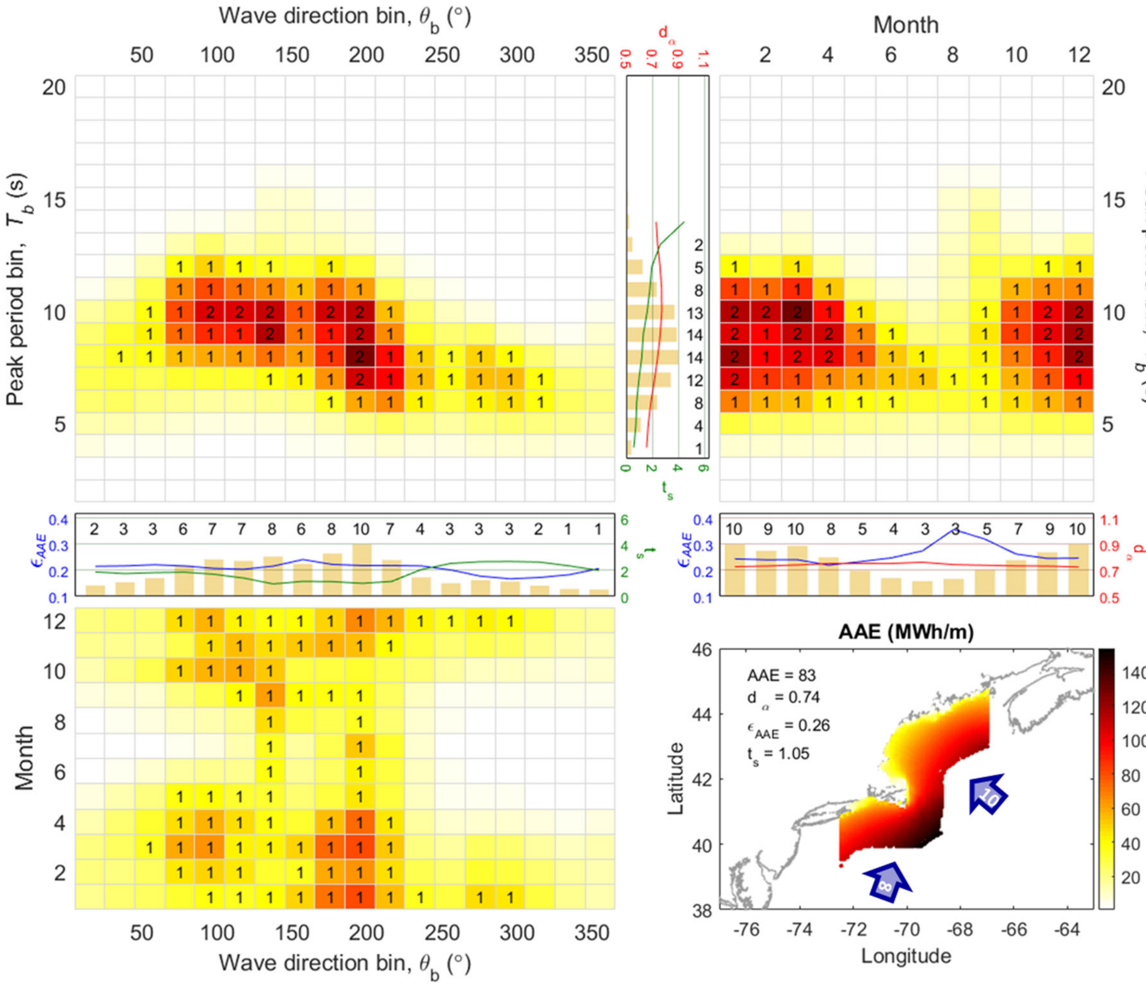

Figure 5.12. [Region 10 - Atlantic - North coast] The detailed descriptions are identical to Figure 5.3.

5.2.11 Region 11- Puerto Rico

The wave resource characteristics for the Puerto Rico coast are illustrated in Figure 5.13. As seen on the geographic map, most energetic sites are mainly located in the Atlantic Ocean side coast, on the order of 50 MWh/m. The Caribbean Sea side has a little energy generally below 10 MWh/m. The overall directionality coefficient is remarkably large (0.89) compared to the other regions. The overall seasonal variability (1.1) and spectral width (0.27) are moderate.

Looking at the joint distributions together, local wind seas (<7s) mainly come from ENE (40-80^{o}) and SE (100-150^{o}) almost all year round. Short period swells (8-9s) mainly come from ENE (40-70^{o}) almost all year round. Long period swell (10-14s) mainly come from NNE (350-30^{o}) in winter. The three marginal distributions show that the swell (9-11s), the waves from NNE (350-30^{o}), and winter contain the most energy for each distribution. The t_s (green in $AAE(T_b)$) increase with increasing peak period where the t_s in the energetic period is on the order of 2.0. The d_α (red in $AAE(T_b)$) is remarkably large for the energetic period, on the order of 0.9. The t_s (green in $AAE(\theta_b)$) is generally consistent, on the order of 2.0, except for the NNW (330-360^{o}) directional band, on the order of 3.0. The ϵ_{AAE} (blue in $AAE(\theta_b)$) is relatively small for the energetic directional band ranging from NNW to NNE (340-40^{o}), on the order of 0.25. The d_α (red in $AAE(M)$) is large in the energetic season, winter, on the order of 0.9. The ϵ_{AAE} (blue in $AAE(M)$) is small in winter, on the order of 0.25.

Similar to the Hawaiian regions, this region is roughly divided into the northern and southern coast: Atlantic Ocean side and Caribbean Sea side. The wave systems are summarized and identified in the geographic map using arrow marks. The Atlantic Ocean side has two comparable wave systems: long period swell (10-14s) coming from NNE (350-40°) in winter and short period swell (8-9s) coming from ENE (40-70°) throughout the year. On the other hand, the Caribbean Sea side has a local wind-sea (6-7s) coming from SE (100-150°) throughout the year. Like the Hawaiian coast, local trade winds blow from ENE around Puerto Rico almost all year round and these are weak on the leeward side. Long period swell generated by the NW trade winds in winter travels a long distance across the Atlantic Ocean.

The different wave energy planning and WEC designs may be required at the Atlantic Ocean side coast and the Caribbean Sea side. On the Atlantic Ocean side, because two types of wave conditions exist with a high level of energy, a wave energy development project will need to select a target wave system based on a projects scale and the pros/cons of the two wave systems. If an energy project emphasizes a constant energy generation (high capacity factor), targeting WEC technologies with an idealized operating period of 8-9s would maximize the energy generation and a directionally dependent WEC technology needs to face ENE. If an energy project targets the wave system from NNE to generate larger energy, the design size and capacity factor of the project would be increased and decreased, respectively. On the other hand, the WEC operating period (6s) may be recommended to maximize the energy generation and a directionally dependent WEC technology needs to face SE for the Caribbean Sea side. Although the energy potential is relatively low in this sub-area, the wave system within a narrow direction/period, which is evenly distributed over all year round allows for a simplification of the device design, potentially leading to an increase of a capacity factor and a decrease in the cost of small scale projects in this region.

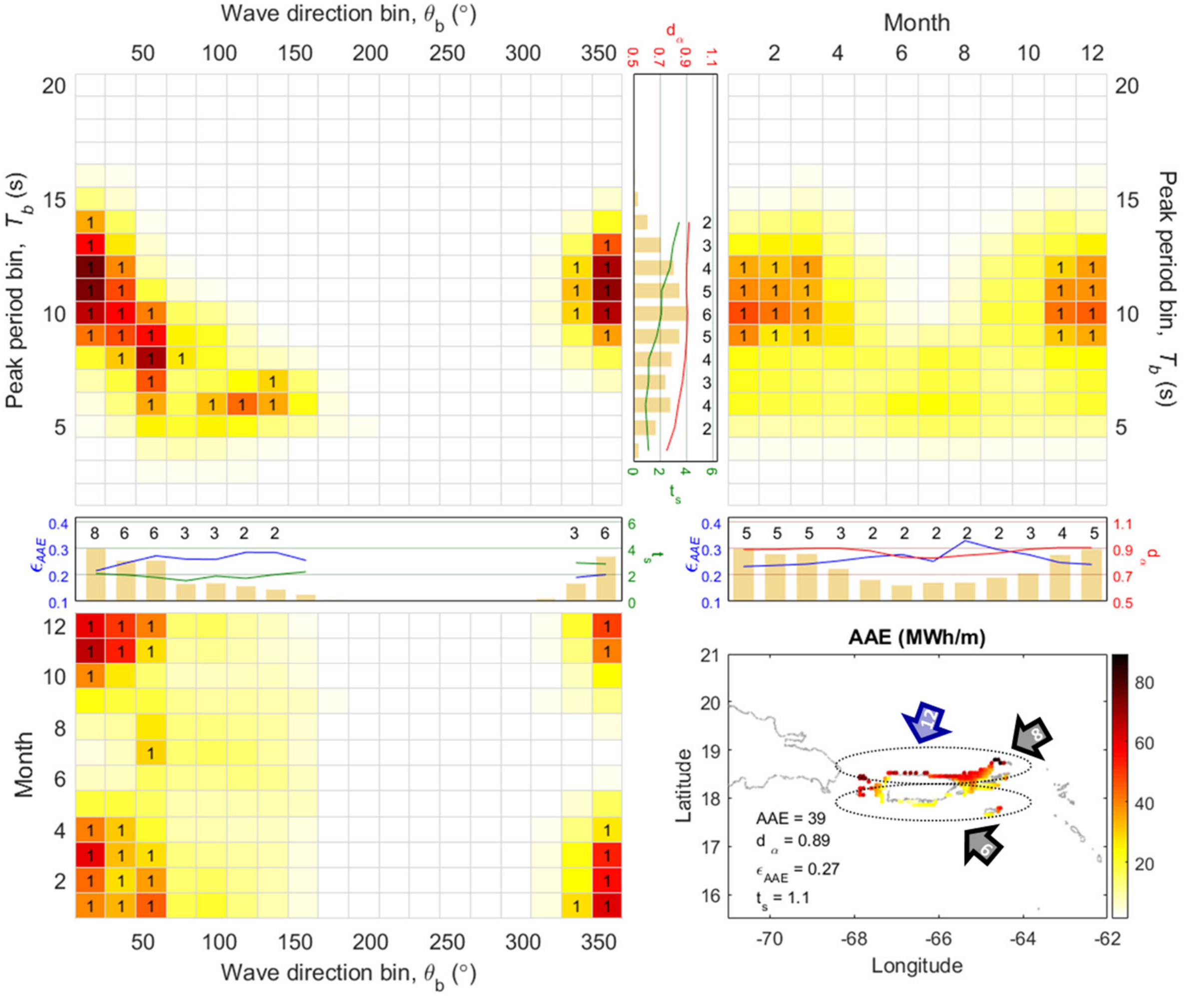

Figure 5.13. [Region 11 - Puerto Rico] The detailed descriptions are identical to Figure 5.3.

5.3 Summary

Eleven wave energy regions for the US coastal waters are delineated using the total wave energy potential and the resource parameters obtained in Chapter 4: total AAE, AAE-weighted period, AAE spectral width, AAE directionality coefficient, seasonal and inter-annual variability. The marginal and joint distributions of the wave energy resources are calculated and described to provide information about how much wave energy is available in a particular sea state within each region. In addition, the key characteristics, AAE spectral width, AAE directionality coefficient, and seasonal variability, are calculated using the marginal energy distributions to characterize the conditional wave energy resources, e.g., the spectral width of AAE from the particular directions, the spectral width of AAE in the particular month. The joint and marginal distributions of AAE and the corresponding resource parameters provide high-resolution assessments of US wave energy resources and characteristics relevant to the design, operation and maintenance of WEC technologies, e.g., targeting wave systems, optimal design size, operating period band, front direction, temporal variations, and capacity factors in specific wave energy regions.

The detailed characteristics of the energetic wave systems for each region are summarized in Table 5.2. In the Bering Sea and Pacific Ocean coast, R1-R4, winter season long period swell having a peak period exceeding 10 seconds contribute most to the total energy with different wave directions: Bering Sea (R1) SW, Aleutian Trench, Gulf of Alaska (R2) SSW, Pacific Northwest Coast (R3) W, California Coast (R4) WNW. The Hawaiian coast, R5 and R6, has multiple energy peaks. The northern coast (R5) has two comparable systems, winter season long period swell coming from NW and all year round short period swell coming from ENE direction. In addition to the two peaks, the southern coast (R6) has another energy peak during summer season, long period swells coming from SSW. In the Gulf of Mexico, region 7 and 8, winter season wind-sea with a peak period below 7 seconds contains the most energy with different wave directions: western and central (R7) SE, eastern (R8) NW. Like the Hawaiian coast, the Atlantic Ocean coast, region R9-11, has multiple wave systems: South & Mid-Atlantic (R9) has two energetic systems which are short period swell coming from ENE and ESE in winter and summer, respectively. The North Atlantic (R10) has two energetic winter season short period swell coming from SWS and SE. Puerto Rico (R11) has two separate energetic systems: winter season long period swell coming from NNE and all year round short period swell coming from ENE.

Table 5.2. Summary of the characteristics of the energetic wave systems at each region. Bold indicates the most energetic system.

Regions	Wind wave $T_p \leq 7$	Short swell $7 < T_p \leq 10$	Long swell $10 < T_p$
R1 : Bering Sea	N/Year	All/Win	**SW/Win**
R2 : Aleutian Trench, Gulf of Alaska	All/Year	S/Win	**SSW/Win**
R3 : Pacific Northwest Coast	NW/Sum	W/Year	**W/Win**
R4 : California Coast	NW/Sum	NW/Sum	**WNW/Win**
R5 : Hawaiian- Northern coast	ENE/Sum	**ENE/Year**	**NNW/Win**
R6 : Hawaiian- Southern coast	ENE/Year	**ENE/Year**	**NNW,SSW/Win,Sum**
R7 : Gulf of Mexico-Western,Central	**SE/Win**	SE/Win	SE/Sum
R8 : Gulf of Mexico-Eastern	**NW/Win**	NW/Win	
R9 : Atlantic-South, Mid	SWS/Win	**ENE, ESE/Win,Sum**	
R10: Atlantic-North	SW/Win	**SWS, SE/Win,Win**	
R11: Puerto Rico	E/Year	**ENE/All**	**NNE/Win**

CHAPTER 6.

WAVE ENERGY RESOURCE CLASSIFICATION

Energy resource classification systems are useful assessment tools that support energy planning and project development, e.g., siting and feasibility studies. They typically establish standard classes of power, a measure of the opportunity for energy resource capture. In this chapter, wave energy resource classification systems for the US are developed based on wave power and its distribution with peak period. As the operating resonant period bandwidth of a wave energy converter (WEC) technology is an important design characteristic, the dominant period band containing the largest energy content is identified among three peak period band classes. These classification systems, consisting of four power classes and three peak period band classes based on the total wave power as well as the partitioned wave power in the dominant peak period band, discriminate distinct trends in wave energy resource among five regions within the US, and provide useful information for energy planners, project developers, and technology designers. They also establish a framework for investigating the feasibility of a compatible wave climate (design load) conditions and WEC technology classification system to reduce design and manufacturing costs.

6.1 Definition of classes

6.1.1 *Peak period band classes*

To aggregate all the wave power and AAE data as a function of peak period band, three different peak period bands are defined as shown in Table 6.1. These peak period bands are designed to discriminate different WEC operating bandwidths, but roughly correspond to peak period bands for local wind seas, short period swell and long period swell.

Table 6.1. Definition of peak period and frequency band classes.

Class	Band 1	Band 2	Band 3
Period, $\boldsymbol{T_b}$ (s)	$0 < T_b < 7$	$7 < T_b < 10$	$10 < T_b$
Frequency, $\boldsymbol{f_p}$ (hz)	$0.14 < f_p$	$0.1 < f_p < 0.14$	$f_p < 0.1$

The distribution of wave power and AAE over peak period is shown in Figure 6.1 for the Hawaii site. The wave power $J_m(T_b)$ within each band are summed to compute their power contribution.

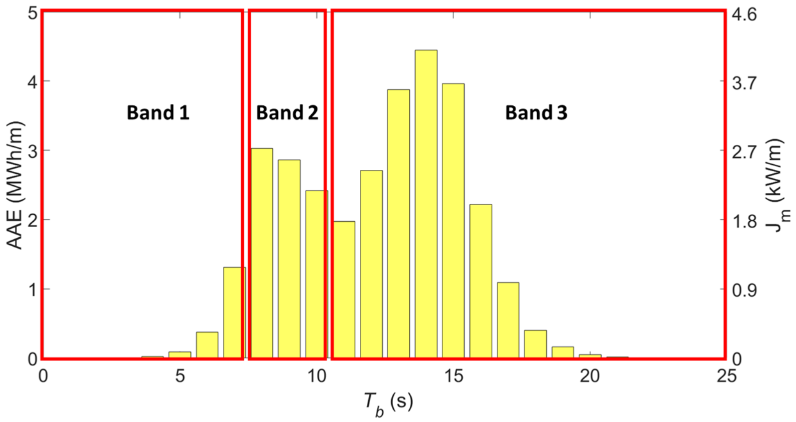

Figure 6.1. Example of splitting wave power distribution into different peak period bands for a particular location.

6.1.2 Wave power classes

Four wave power classes are defined as shown in Table 6.2. The threshold value separating Classes II and III roughly corresponds to the median wave power for the United States. The threshold value separating Classes I and II is one standard deviation greater than this median value, and that separating Classes III and IV is one standard deviation less than this median value. Like wind classification systems, this power class delineation is somewhat arbitrary, but relative qualitative descriptions for each resource class can be assigned, e.g., "excellent" for Class I and "poor" for Class IV. As the wave energy industry matures, the number of classes and class thresholds can be adjusted. Also, tangible metrics of wave energy project scale, e.g., installed power capacity, could be correlated with theoretical power; and more tangible descriptions of the types or applications of wave energy projects could be incorporated, e.g., to distinguish high power sites that could support utility-scale projects from low power sites that could only support distributed alternative market applications like desalinization or charging batteries for remote sensors.

Table 6.2. Definition of power classes.

Class (description)	I Excellent	II Good	III Marginal	IV Poor
J_m (kW/m)	$22.8 < J_m$	$5.7 < J_m < 22.8$	$1.1 < J_m < 5.7$	$J_m < 1.1$
AAE (MWh/m)	200 < AAE	50 < AAE < 200	10 < AAE < 50	AAE < 10

The power classification for wind energy resource classification is based on the total wave power, and this is the basis for one of the resource classification system proposed herein. But, it could also be based on the largest partitioned wave power among the peak period bands. For the Hawaii site example, Figure 6.2 shows that it is a Class I site based on the total wave power. Considering the largest power in the dominant peak period band 3, however, it would only qualify as a Class II resource. While this approach for defining the power class departs from convention, it may be more useful for technology developers; especially for less mature technologies that may be limited to a narrow bandwidth resonance response.

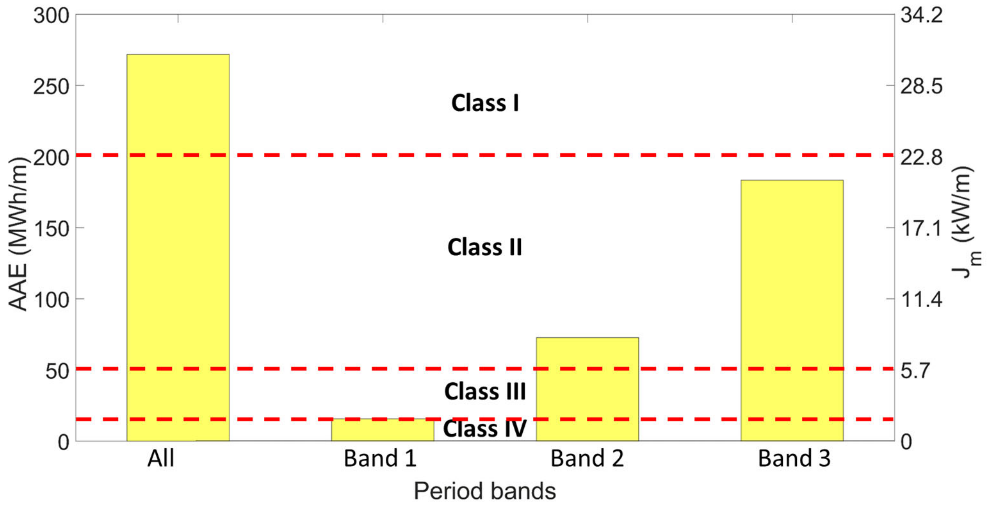

Figure 6.2. Definition of wave energy classes. The values correspond to Figure 6.1.

6.1.3 Wave power classification matrices

Based on the four power classes and three period band classes the wave power classification matrix has twelve possible resource classes. Two versions of the classification system are described, one based on the total wave power, and the other based on the maximum partitioned wave power occurring in the dominant peak period band. The classification matrix for both systems is shown in Table 6.3, with the total wave power or partitioned wave power determining the power Class (I-IV), and the predominant period band containing the largest energy content determining the subclass (1-3).

Table 6.3. Power classification matrix for US coastal waters.

Class	I $22.8 < J_m$	II $5.7 < J_m < 22.8$	III $1.1 < J_m < 5.7$	IV $J_m < 1.1$
1,0 < T_b < 7	I(1)	II(1)	III(1)	IV(1)
2,7 < T_b < 10	I(2)	II(2)	III(2)	IV(2)
3,10 < T_b	I(3)	II(3)	III(3)	IV(3)

If adopting the first classification system based on total wave power, the Hawaii site in the previous example is a Class I(3) resource based on the total wave power of approximately 30 kW/m, with its largest energy content in period band 3. With the second system, this site would be classified as a Class II(3) resource based on a partitioned wave power of approximately 20 kW/m. The classification systems can be applied with benefits not only to mono-resonant WEC technologies, but also to multi-resonant technologies. The first classification system may be useful to the multi-resonant WEC technologies operating in a broad range of the period bands, while the second classification system is more applicable to the mono-resonant technologies which tend to operate within the most energetic period band. Note that the second classification system would tend to better characterize sites having a narrow spectral width or unimodal energy distribution and would get lost power class in the other period bands. Although the wave powers in the second, third energetic period bands are not negligible, especially for the bimodal or multi-modal energy distributed sites, the second classification system still provides the most valuable information for the mono-resonant technologies.

6.2 Wave power and period classes for US coastal waters

The geographical distribution of the total wave power along the US coastline is shown in Figure 6.3. This map shows that the largest resources, with wave power exceeding

46 kW/m (400 MWh/m), are found along the West Coast and along the southern coast of Alaska. These are highly desirable regions, especially when sites are close to population centers and port facilities. Although Hawaii has slightly lower resource potential compared to the West Coast, on the order of 34 kW/m (300 MWh/m), it has a relatively high cost of energy. The East Coast, with relatively less resource potential (power densities typically below 26 kW/m) may still be viable, especially when considering the high population densities along the coast.

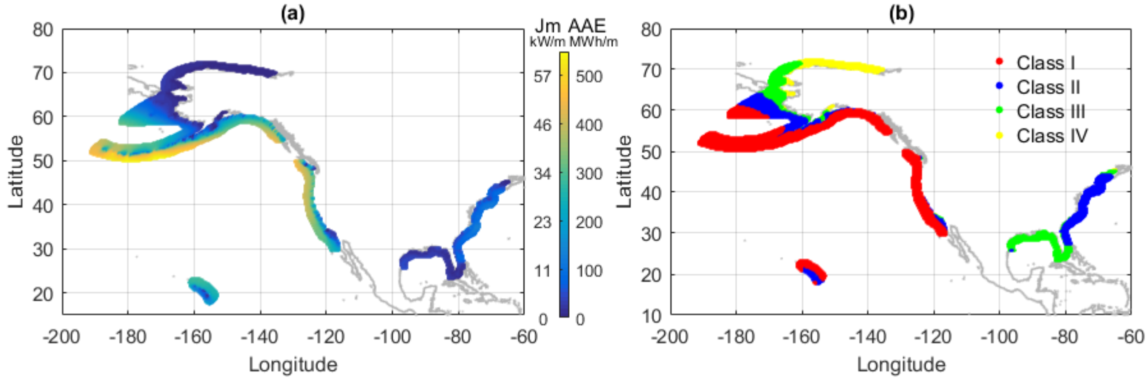

Figure 6.3. (a) Geographical distribution of the total wave power, (b) Power class based on the total wave power.

Figure 6.3(b) shows the geographic distribution of the power classes for the total wave power (classification system 1) defined in Table 6.1. Class I sites are located on the West Coast, the southern coast of Alaska, including the Aleutian Islands, offshore in the Bering Sea, including St. Mathew Island, and the Hawaiian Coast. Class II sites are dominant along the East Coast, but are also found along the southern portion of the West Coast, near the shoreline of the southern coast of Alaska, and offshore in the Bering Sea. Class III sites include all sites along the Gulf Coast. There are also many Class III sites along the west coast of Alaska and offshore in the Bering Sea above sixty-degrees latitude.

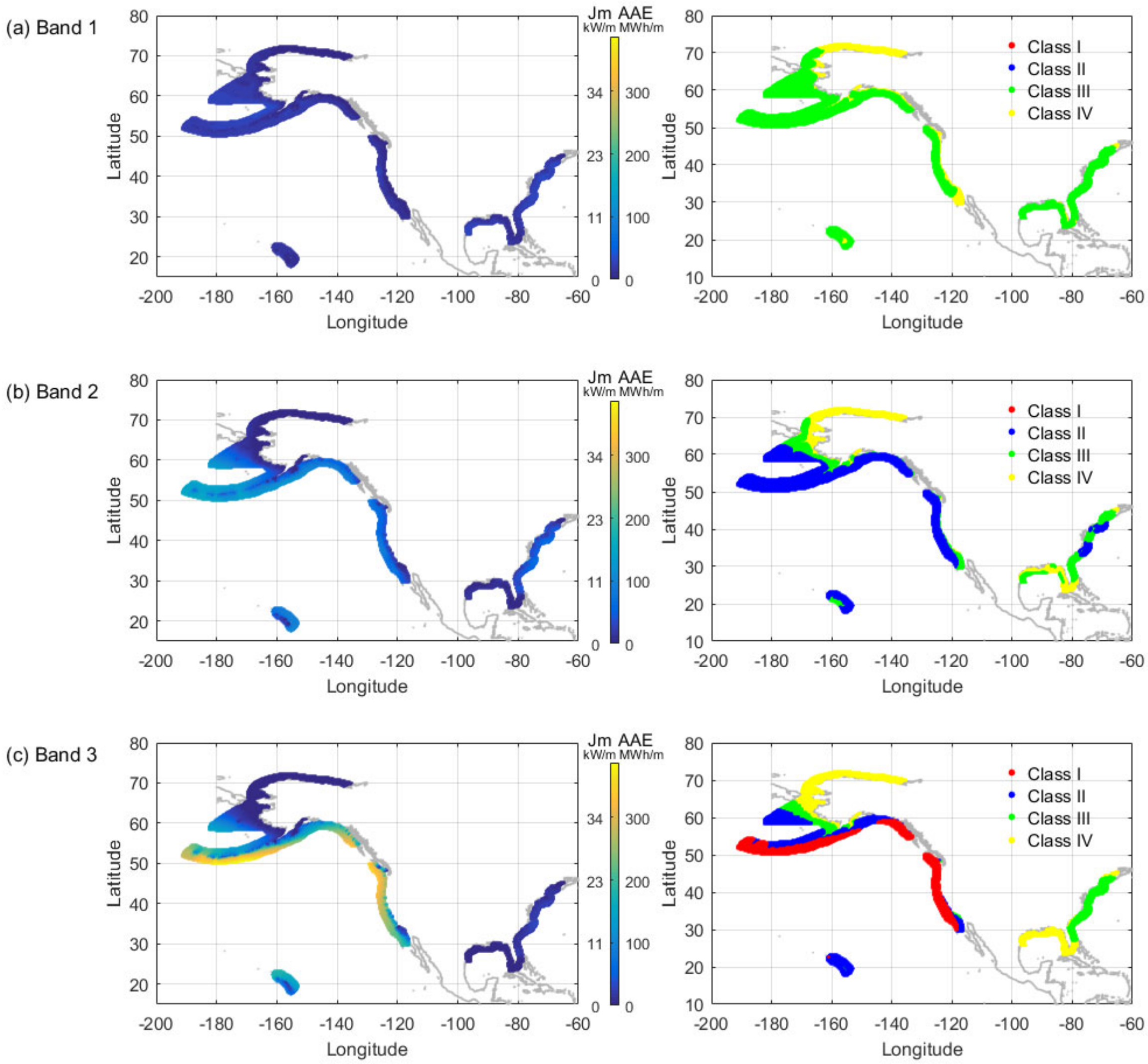

Figure 6.4. (left) Geographical distribution of wave power within each period band, (right) Geographical distribution of power classes based on wave power within each period: (a) band 1 constrained by period 0-7s, (b) band 2 constrained by period 7-10s, (c) band 3 constrained by period larger than 10s.

Considering the second classification system, which uses the partitioned wave power within the dominant peak period band to define the power class, allows an additional winnowing of sites that leads to a higher threshold for a power class designation. To evaluate the regional trends resulting from this classification system, the geographical distributions of the wave power for each of the period bands are shown in Figure 6.4 (left) along with the power class (right). These maps in Figure 6.4 can be compared with the one in Figure 6.3 to illustrate how the partitioned wave power classification system winnows sites to more exclusive power classes with better opportunities for wave energy extraction.

Local wind seas (band 1) generally contain the least wave power throughout US coastal waters. However, local wind seas can contain the most energy regionally, e.g., for the Gulf Coast where they generally contribute more than swell, and more than fifty-percent of the total energy contained in all sea states.

For the East Coast, a short period swell contains the most energy. Class II sites in two sub-regions standout because the energy content in this short period swell is sufficient to qualify as a Class II resource. These sub-regions are centered around the North Carolina Coast (Cape Hatteras) around thirty-five degrees latitude; and the New Jersey Coast around forty-degrees latitude. WEC technologies designed for these sub-regions could capture more energy resonating in the short period swell band than other sites along the East Coast, potentially saving costs associated with advanced controls and advanced power-take-offs (PTO) required to broaden resonance bandwidth.

For most of the West and Alaskan Coasts, the long period swell contains a sufficient amount of energy for most of the Class I sites to qualify as a Class I resource. A few Class I regions, by contrast, rely on the energy contained in short period swell, as well as long period swell to qualify as a Class I resource, e.g., Class I sites in the Gulf of Alaska and Bering Sea, including the Aleutians and West Alaskan Coast. Using similar arguments as above, these sites may be less desirable because the cost of WEC technologies generally rise to broaden the resonance bandwidth with advanced controls and advanced PTOs.

Hawaii tends to have Class II sites on the northern side for both swell bands (2-3). As discussed above, this unique feature of the Hawaiian wave energy resource, will likely require a different approach to WEC design and operation.

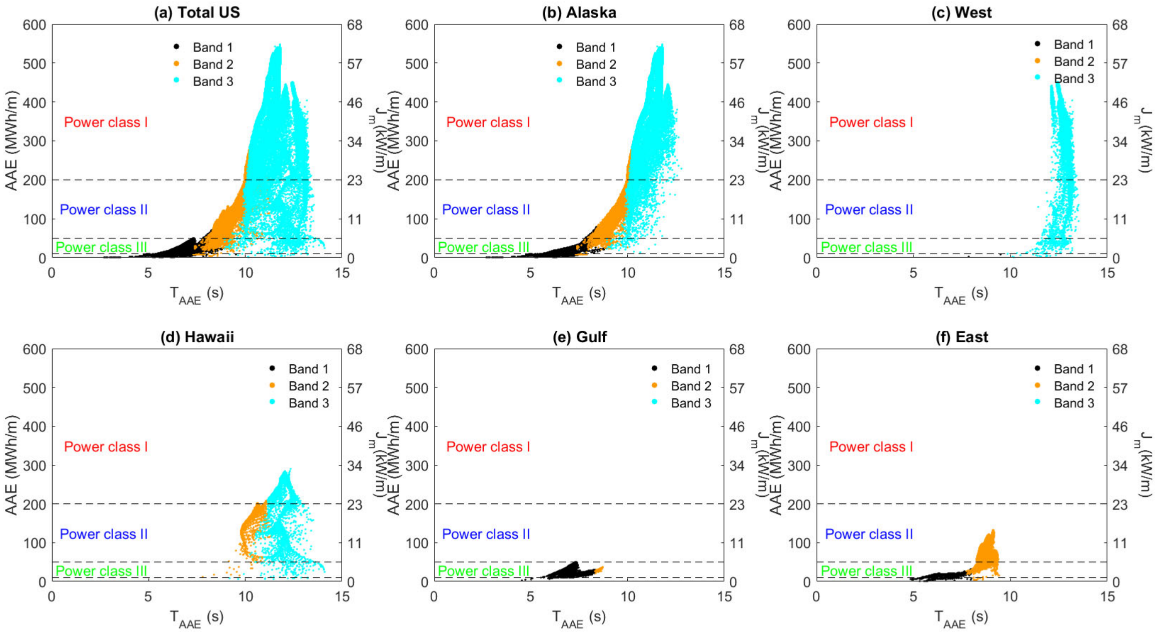

Figure 6.5. Total wave power scatter plots as a function of AAE-weighted period, T_{AAE} : (a) total US coastal waters, (b) Alaska Coast, (c) West Coast of US, (d) Hawaii Coast, (e) Gulf Coast, (f) East Coast of US. Dash line defines power classes and color indicate the dominant period band having the largest energy.

Because the energy period, the variance-weighted period of the frequency variance density spectrum, cannot be computed from the partition data; the analogous AAE-weighted period, T_{AAE} is computed based on the power as a function of the partition peak period. For each location, this parameter indicates the center of the period distribution containing the largest energy. A scatter plot of the total energy for each location as a function of the T_{AAE} is shown in Figure 6.5. The points are color coded by the dominant period band with the most energy. In general, the dominant period band corresponds well to the T_{AAE}, supporting the period band subclass delineation. The exception is a number of sites in band 2 for Hawaii, which have a T_{AAE} greater than 10s, corresponding to band 3. Locations in Hawaii have two energy peaks, in the short and long swell bands, which are frequently similar in magnitude; therefore, even if the energy for the short period swell is slightly larger, the energy in the long period swell is enough to increase the T_{AAE} to a value greater than 10s.

For the total wave power classes, the West Coast sites are mostly Class I resources and are generally clustered well above 10s of T_{AAE}, with the largest energy within band 3. Hawaii has two dominant period bands: band 2 dominant sites clustered around $T_{AAE} =$ 10s, which are almost all Class II resources, and band 3 dominant sites clustered around $T_{AAE} = 12$s, which are a mix of Class I and II resources. Alaska has band 1 sites qualifying as Class III resources, band 2 sites qualifying as Class II resources, and band 3 sites qualifying as both Class I and II resources. The Gulf is a band 1, Class II dominant resource and the East coast has band 1 and 2 dominant sites with a mix of Class II and III resources.

6.3 Classification systems for US coastal waters

The geographical distribution of the power classes using total wave power is shown in Figure 6.6, and that for partitioned wave power in Figure 6.7 to delineate distinct regional patterns of dominant resource classes. For the first classification system (Figure 6.6), sites along the West Coast and along the southern coast of Alaska have predominantly Class I(3) resource sites. In the Hawaii coast, three dominant resource classes are identified: I(3), II(3) and II(2). The East coast has predominantly Class II(2) resources, and the Gulf Coast has III(1).

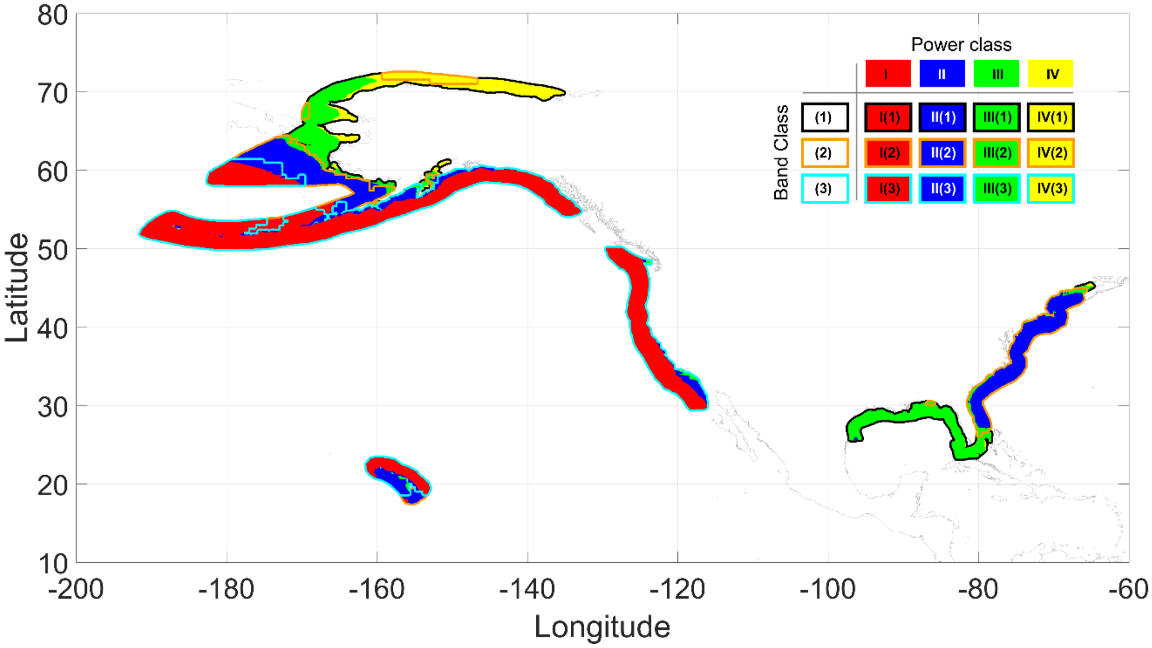

Figure 6.6. Geographical distribution of classification system 1. The face color indicates the class of total wave power and edge color indicates the class of predominant period band.

For the second classification system (Figure 6.7), Class I(3) resource sites are exclusive to the West Coast region, along the southern coast of Alaska and a small region in northern Hawaii. Class I(3) sites based on total wave power offshore of the west coast of Alaska in the Bering Sea at approximately sixty-degrees latitude, and most of the I(3) sites in Hawaii, become Class II(2) and Class II(3) sites when using the dominant partitioned wave power. Likewise, most of the Class II sites on the East Coast cannot qualify as Class II resources when using the dominant partitioned wave power.

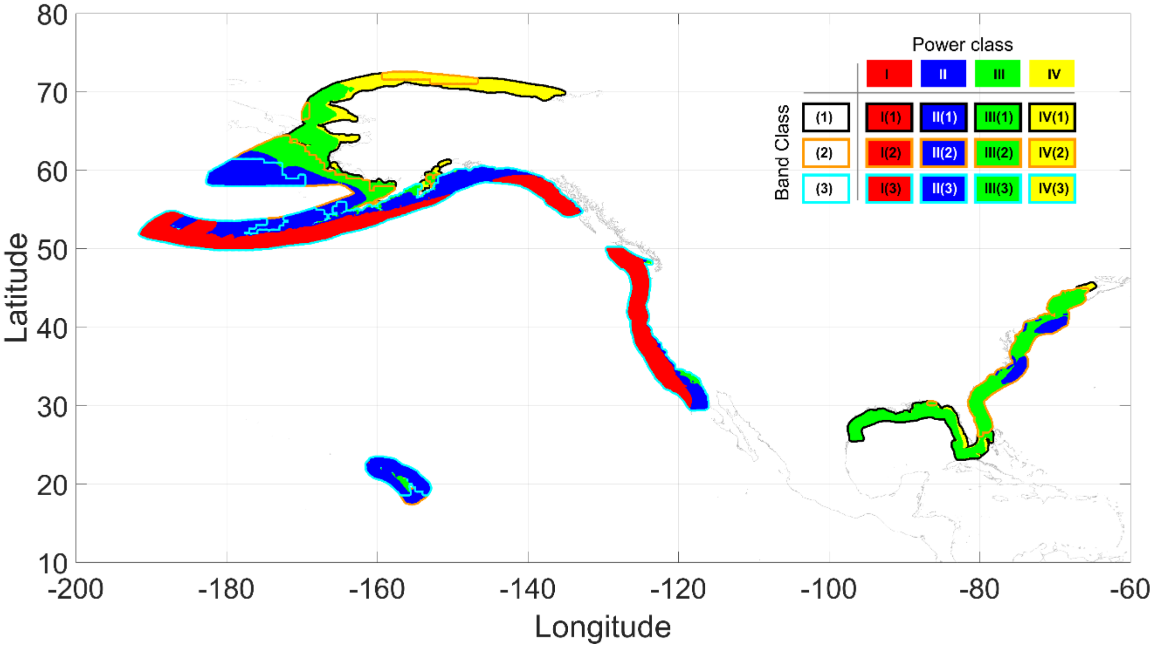

Figure 6.7. Geographical distribution of classification system 2. The face color indicates the class of partitioned wave power in the predominant peak period band and edge color indicates the class of predominant period band.

For regional energy planning, it is useful to consider the relative portion of these different resource classes for the entire US and within different regional wave climates. Percent contribution of sites that fall into the classification systems for the total US coastal water as well as the sub-regions is summarized in Table 6.4 (classification system 1) and Table 6.5 (classification system 2). The use of both classification systems to winnow resource classes offering potentially higher value propositions for wave energy conversion is illustrated in the following discussion.

Using total wave power to determine the power class (classification system 1), a large number of the sites in the US (45%) qualify as Class I resources. Using the more exclusive dominant partitioned wave power (classification system 2) reduces the number of Class I resource sites in the US to 29%. The second classification system is effectively a screening tool that filters resource classes using system 1 for further examination. These Class 1 resource sites using system 2 could be exceptional high-tier Class I resources with a potentially narrower power distribution that presents exceptional opportunities for wave energy conversion. However, exceptions can include sites where the maximum energy content straddles two period bands, or Class I(3) sites that have broad power distributions with a lot of the energy well above 10 seconds. Further examination to check for these conditions is, therefore, warranted.

Table 6.4. Percent contribution of classification system 1 (total wave power class).

Class	I	II	III	IV	I	II	III	IV	I	II	III	IV
	Total U.S.				Alaska				West			
1	-	-	16	5	-	1	14	9	-	-	-	-
2	1	22	2	1	2	16	1	2	-	-	-	-
3	45	7	1	-	49	6	-	-	90	8	2	-
	Hawaii				Gulf				East			
1	-	-	-	-	-	-	99	1	-	-	10	1
2	1	16	-	-	-	-	-	-	-	81	8	-
3	49	31	3	-	-	-	-	-	-	-	-	-

Table 6.5. Percent contribution of classification system 2 (dominant partitioned wave power class).

Class	I	II	III	IV	I	II	III	IV	I	II	III	IV
	Total U.S.				Alaska				West			
1	-	-	15	7	-	-	12	12	-	-	-	-
2	-	9	16	1	-	9	10	2	-	-	-	-
3	29	21	2	-	28	26	1	-	82	15	3	-
	Hawaii				Gulf				East			
1	-	-	-	-	-	-	93	7	-	-	8	4
2	-	17	-	-	-	-	-	-	-	19	69	-
3	-	75	8	-	-	-	-	-	-	-	-	-

The effect of this screening is more pronounced in some regions compared to others. Resource classes in the West Coast and Gulf Coast do not change significantly, indicating regions with exceptionally narrow ranges of peak periods for the power distributions. Those for the remaining regions change more significantly because they do not exhibit this same resource attribute. Class I resource sites in Alaska and Hawaii using total wave power are effectively divided into Class I and II resource sites when using the dominant power. These changes are even more pronounced for the East Coast, where the majority of Class II resource sites (System 1) become Class III sites (System 2).

6.4 Summary

Wave energy resource classification systems are developed for the US based on wave power and the dominant peak period band. Recognizing that energy capture is maximized when the natural frequency of the WEC device is close to the dominant frequency (period) of the incident wave, the distribution of the wave power is assessed by quantifying its contribution to total wave power in terms of the peak period partition.

Four wave power classes, representing different wave energy conversion opportunities, and three peak period band classes, representing different wave energy transfer mechanisms, local wind-seas, and short and long-period swell, are defined. Two classification systems are proposed, one based on the total wave power and the other based on the partitioned wave power in the dominant peak period band. These classification systems discriminate distinct trends in wave energy resource among five regions within the US, and provides useful information for technology designers. Energetic Class I sites (based on total wave power) that support utility-scale applications are predominant all along the West Coast and the northern and eastern shores of Hawaii and the southern coast of Alaska, extending west along the Aleutians, and for deep sites in the Bering Sea. Class I sites based on the dominant power are more exclusive sites representing exceptional resource opportunities and are also predominant along the West Coast. However, these sites are confined to fewer locations along the southern coast of Alaska and the Aleutians.

CHAPTER 7.

NUMERICAL SIMULATION OF COASTAL CIRCULATION

This chapter focuses on the coastal circulation during upwelling events, which are detected based on the wind records and wind stress driven temperature/salinity changes indicating a consequence of onshore transport near the bottom. In order to describe three-dimensional circulations, particle trajectories during the selected period are calculated and characteristics of the circulations, e. g., divergences of onshore transports near the bottom, upwelling fronts, convergence/divergence of surface flows, are discussed by linking the currents and stratifications. To understand the structures of circulation driven by the wind stresses, alongshore currents, complex bathymetry, and coastline promontory near Pt. Sal, basic mechanisms directly influencing the circulations are discussed. Finally, the mechanisms are linked with the three-dimensional momentum balances and dominant forcing mechanisms are identified for two different circulation events.

7.1 Method

To examine the circulations at Pt. Sal, numerical simulations are conducted for the upwelling favorable wind period, June-July 2015 and July-September 2017 using the Regional Ocean Modeling System (ROMS). Based on long-term (1854-1972) ship reports [101], mean monthly wind stress over the California Coast, the center of maximum equatorward wind stress migrates northward from 28°N in February to 38°N in August. The upwelling favorable winds over the Pt. Sal is strongest in June to July and there are strong temperature gradients with cold coastal waters from the upwelling [101], [102]. The three-dimensional outputs, e.g., velocity, temperature, salinity, and momentum terms, are used to select the upwelling event and describe the circulations.

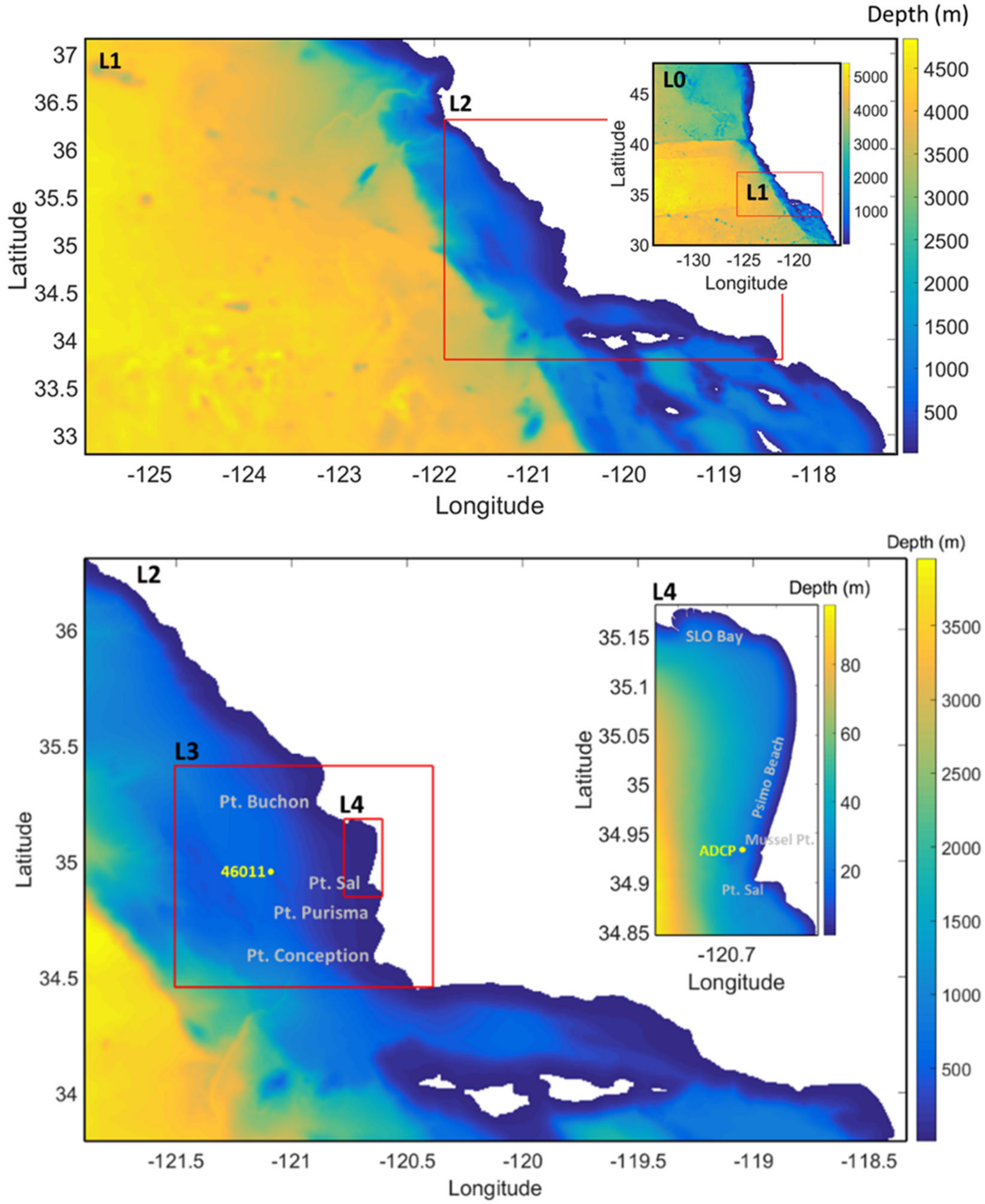

Figure 7.1. Grids used for simulations with three levels of successive one-way nesting from (a) L0 grid (dx = 3km), L1 grid (dx = 1km), (b) L2 grid (546X386, dx=600m), L3 grid (857X732, dx=120m), L4 grid (382X772, dx=40m). The color indicates the water depth.

7.1.1 Numerical model

The Regional Ocean Modeling System (ROMS), ROMS is a three-dimensional ocean circulation model solving the Reynolds averaged Navier Stokes equations with the hydrostatic and Boussinesq approximations [103]–[106]. Multiple nested grids are configured (Figure 7.1). The model grids downscale from a domain of the US west coast and Eastern Pacific (L0, resolution 3km), to continental slope and outer-shelf region from the Southern to Central California (L1, resolution 1km), to the region from Point Conception to south of Monterey Bay (L2, resolution 600 m), to the interior Point Sal region (L3, resolution 120 m, and L4, resolution 40 m). The larger grid simulation provides the initial and boundary conditions for the next smaller grid through open boundary conditions using standard offline, one-way nesting techniques [107]. The L1, L2, L3, and L4 grid systems have 42 bathymetry-following vertical levels and sigma-coordinate parameter settings. Model bathymetry (1 arc second resolution) is obtained from the NOAA NGDC database (https://www.ngdc.noaa. gov/). The model configurations are summarized in Table 7.1.

Table 7.1. ROMS model configurations. The √ symbol means the model is performed.

Model	Grid	Resolution	Period	With Winds	Without Winds	With Winds &Tides
L0	556 X 541 X 42	3km	Jun.- Jul. 2015	√	-	-
			Jun.- Sep. 2017	√	-	-
L1	770 X 392 X 42	1km	Jun.- Jul. 2015	√	-	-
			Jun.- Sep. 2017	√	-	-
L2	546 X 386 X 42	600m	Jun.- Jul. 2015	√	√	√
			Jun.- Sep. 2017	√	√	-
L3	857 X 732 X 42	120m	Jun.- Jul. 2015	√	√	√
			Jun.- Sep. 2017	√	√	-
L4	382 X 772 X 42	40m	Jun.- Jul. 2015	√	√	√
			Jun.- Sep. 2017	√	√	-

Radiation boundary conditions are applied to barotropic fields where the interior energy of the domain pass through the boundary [107], [108]. Nudging, the 1-day time scale for incoming and 365 days for outgoing, is added for baroclinic boundary conditions [109]. For non-linear model, a horizontal viscosity of 0.1 m^2/s^s is applied to dampen small-scale numerical instabilities. The Coupled Ocean-Atmosphere Mesoscale Prediction System (COAMPS) model provides meteorological forcing (3km resolution) to estimate bulk fluxes: surface wind, net shortwave/longwave radiation flux, rain fall rate and surface air relative humidity/pressure/temperature. A quadruply nested model output over the northeast Pacific and western North America domain is hourly averaged and combined to produce ROMS surface forcing files [110], [111]. To validate the surface forces, the COAMPS wind is compared to observed wind records at NDBC buoy 46011 during June-July 2015. As shown in Figure 7.2. Hourly averaged time series (GMT) of 46011 buoy records (black) and COMAPS model results (blue) interpolated to the buoy location during June- July 2015. NDBC 46011 buoy location is indicated with a yellow circle in Figure 7.1. The wind is consistent with typical conditions in this area [18], [112]–[114] indicating the upwelling favorable with several wind relaxations. The direction and amplitude of the COAMPS wind are well matched to the observed wind (R^2 ≈ 0.8). To understand mechanisms influencing the circulations, e.g., wind stresses, California Undercurrent, coastal jet, upwelling plume, and the promontory of bathymetry, tidal forcing is not included. The model without tidal motion is easier to resolve the lagrangian tracks and identify the forcing mechanisms, particularly for the cross-shelf circulations. Note that the model results with and without tides are similar to each other.

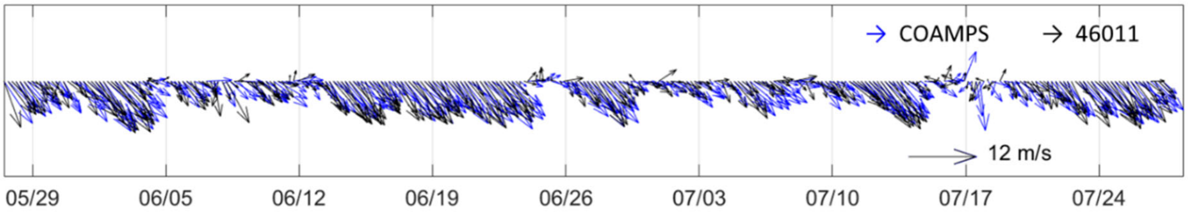

Figure 7.2. Hourly averaged time series (GMT) of 46011 buoy records (black) and COAMPS model results (blue) interpolated to the buoy location during June- July 2015. NDBC 46011 buoy location is indicated with a yellow circle in Figure 7.1.

7.1.2 Model validation

Results of a field experiment measuring the temporal and spatial variability near the Pt. Sal headland during June- July 2015, a pilot study named Pt. Sal Inner Shelf Experiment (PSIEX) [115], [116], are used to validate the numerical model. In order to facilitate direct comparison with the measurement, a model including tide forcing is simulated for the validation purpose. Barotropic tidal elevations and velocities of astronomical tidal constituents (K2, S2, M2, N2, K1, P1, O1, and Q1) are projected onto the lateral boundaries of L2 grid from the ADCIRC tidal model [117]. The interaction of tidal forcing within L2 grid model transmits to the finer-resolution grid models by the lateral boundary conditions. The subtidal currents and temperature obtained from a thermistor and an acoustic Doppler current profiler are compared with the model results in Figure 7.3. The location of the measurement is shown in Figure 7.1. The 1 Hz ADCP velocities were averaged over 2.5 minutes, and the velocities were then depth-averaged from the bins below the sea surface to the first ADCP bin above the transducer head. The temperature and ocean currents are low-pass filtered with a 33-hr cutoff in order to remove any tidal, diurnal, or higher frequency processes.

As shown in Figure 7.3, the modeled results are generally well matched with the measurements, indicating the similar temporal trends in both temperature (0.7 R-squared) and currents (Eastward : 0.6 R-squared, Northward : 0.5 R-squared). Especially, the model shows reliable results during the upwelling favorable wind periods with 0.8 R-squared in currents and 0.9 R-squared in temperature, e.g., 06/14-6/20, 07/13-7/16, and 7/24-7/27. On the other hands, the errors are relatively large during wind relaxation periods with 0.3 R-squared in currents and 0.7 R-squared in temperature, e.g., 06/07, 06/25, 07/08, and 07/17.

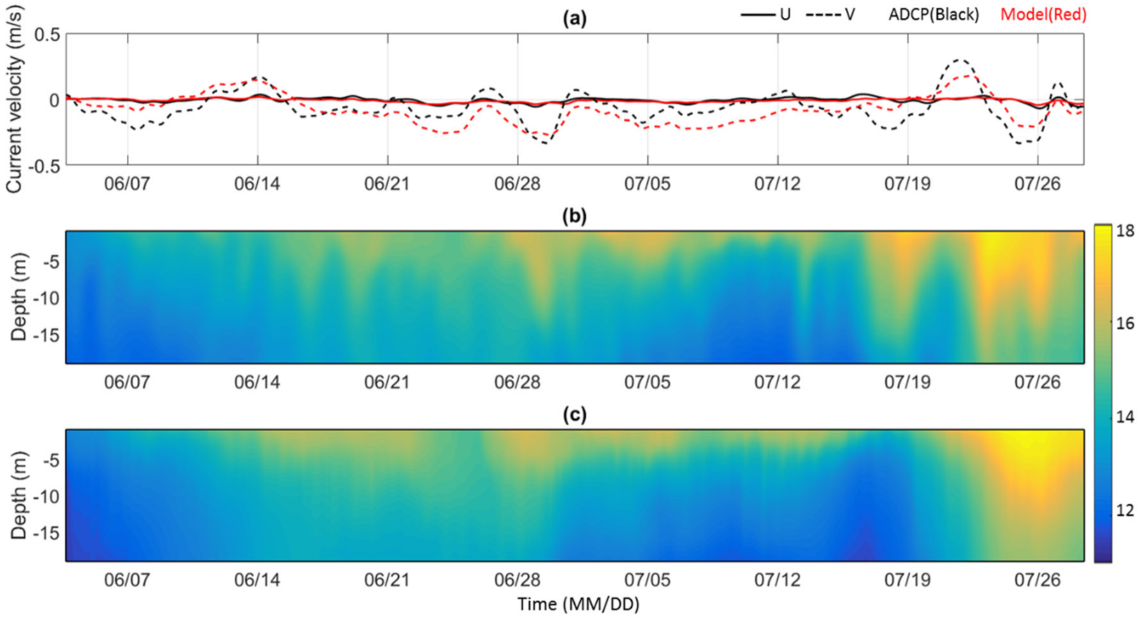

Figure 7.3. (a) Depth-averaged U-velocity (solid-line) and V-velocity (dash-line) from the ADCP measurement (black) and model (red). Vertical structures of temperature from a thermistor (b) and model (c).

7.1.3 Coastal upwelling detection

To identify time periods where the circulation includes wind-driven coastal upwelling at Pt. Sal, two different sets of model simulations are run: including and excluding the surface wind stresses. Indices indicating the effect of the wind stress driven flow are quantified using the results of two models which are then used to identify the coastal upwelling events to be analyzed in detail. Offshore transport in the surface layer, the primary consequence of the coastal upwelling, may not be helpful to delineate the coastal upwelling in this area; the regional upwelling front and the edge of the upwelling jets are indistinguishable because the multiple flows, e.g., upwelling jets from Pt. Buchon, locally upwelled cold water, and trapped warm water at the upwelling shadow zone, interact and mix at the surface layer. Especially, the offshore Ekman transport at the surface layer does not guarantee the upwelling circulation when the strong geostrophic current dominates the bottom flow [55]. To avoid the complexities of the surface layer, another consequence of the coastal upwelling, feeding the cold and salty water to the coast near the bottom, is quantified using indices indicating wind stress driven temperature and salinity changes near the bottom.

The temperature and salinity results with the wind stresses are subtracted from the results without the wind stresses. The 80% bathymetry-following water depth is adopted, because thermoclines and haloclines reach 70% depth and the currents are relatively strong at from 80% to 70% in this region as well be shown later in Figure 7.8. These indices are illustrated in Figure 7.4 by using example results from the 40m grid model. The temperature decreases by 8° along the shallow continental shelf due to the wind stresses. Interestingly, temperature changes shown in Figure 7.4(c) is almost zero beyond 6km offshore from the coast which means that the wind stress at this time may not affect the bottom in this area. This result is consistent with the existence of spatial variations of onshore transport near the bottom discussed in a previous study [55]. Beyond 6km offshore from the coast, the upwelling may not be sufficient to overcome the strong poleward geostrophic flow. Salinity increases by 0.2 PSU within the similar boundary shown in temperature changes except for a coast along the Pismo Beach where the salinity decrease by 0.2 PSU. The explanations for these results are presented in section 7.2 and 7.3.

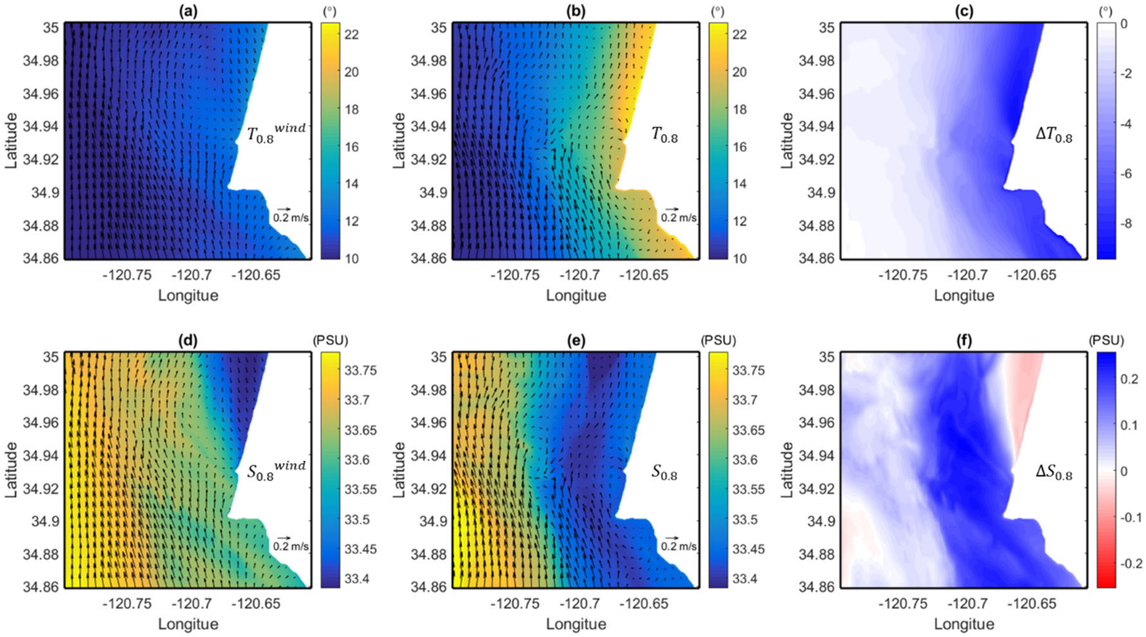

Figure 7.4. Comparisons the two models, including wind stresses and excluding wind stresses, at 80% bathymetric-following depth on 15 July 2015, 05:30 (GMT): (a, d) Temperature and Salinity modeled with wind stresses, respectively. (b, e) Temperature and Salinity modeled without wind stresses, respectively. (e, f) Temperature and Salinity differences between the two models, respectively. The vectors in (a,b,d,e) are the current velocity at 80% bathymetric-following depth.

These indices for the entire simulation period are calculated at the initial positions of the lagrangian tracks, which are defined in section 3.1. The time evolutions of the indices are quantified by averaging the indices at these locations and their anomalies from the mean of the time series for June-July 2015 model are plotted in Figure 7.5 and compared with the wind records at NDBC 46011 buoy station. It is found that the strong upwelling favorable winds do not always result in the temperature drops and salinity increases near the bottom. The maximum decrease of temperature changes and the maximum increase of salinity changes coincidentally occur on 7/15 (in blue) when the alongshore wind is also remarkably strong. Because the tide is excluded and the California Undercurrent is warm and high salinity, the temperature drop and salinity increase near the bottom can be the consequence of the regional upwelling. The next strong signal occurs on 6/17 (in blue) when the temperature drops, salinity increases, and alongshore winds are remarkably strong. Note that an opposite result, the maximum increase of temperature changes and the maximum decrease of salinity changes occur on 6/28 (in red), a relaxation wind period. Based on Figure 7.5, 15 July 2015 is selected and the circulation (hereinafter referred to as the 2015 circulation) at this period are discussed in section 7.2 and 7.3. This method is applied to July-September 2017 simulation and 22 July 2017 (hereinafter referred to as the 2017 circulation) is also detected and the circulation is discussed in section 7.4.

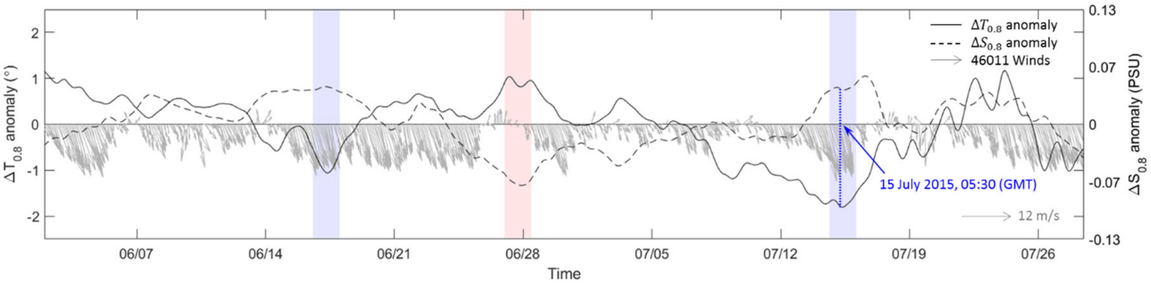

Figure 7.5. Time evolutions of the 15 sections-averaged $\Delta T_{0.8}$ (solid-line, left-axis) and $\Delta S_{0.8}$ (dash-line, right-axis) anomaly during June-July 2015. The $\Delta T_{0.8}$ and $\Delta S_{0.8}$ means temperature and salinity difference between the two models at 80% bathymetry-fallowing water depth, respectively. Vectors indicate wind records at NDBC 46011 buoy. Blue dash-line is a time of the selected coastal upwelling. Boxes spanning 36 hours highlight the upwelling (blue) and relaxation (red) period.

7.2 Circulation near Pt. Sal during upwelling favorable conditions

A baroclinic alongshore pressure gradient derived from remotely forced coastal trapped waves, sea level setup by coastal winds or density gradients [68] can drive a poleward California Undercurrent [69], [70]. A strong southward coastal jet that is in geostrophic balance with the upwelled isopycnals is formed and the winds parallel to a coast results in an accelerating coastal jet in the surface layers [58], [118]. These current systems over the continental shelf during the period of upwelling favorable winds play an important role in the circulation by influencing the Coriolis force and pressure gradient force. The coastline promontory near the Mussel Pt. can affect the pressure gradient forces driven by sea level changes. In addition, the wind stresses in both cross-shore and alongshore directions generate the vertical mixing as well as the pressure gradient force, resulting in various circulation mechanisms. The current systems are resolved in coarser-resolution grid models and projected onto the finer-resolution grid models by the lateral boundary conditions.

In this section, the 2015 circulation near the Pt. Sal is described using the results of the model with wind stresses. Figure 7.6 shows a snapshot of the SST and depth-averaged velocity of the L3 (120m) model during the upwelling event. Consistent with typical circulations in this region, the poleward flow dominates the current over the continental slope. This region has cold water plumes adjacent to the coast where the coastline is parallel to the southeastward winds [27] and strongest temperature gradients within 30 km of the coast [55]. The SST clearly shows that relatively cold waters adjacent to the coast at Pt. Buchon, Pt. Sal, and Pt. Concepcion are a likely consequence of coastal upwelling. The upwelled cold waters at the southern coast of Pt. Buchon pass through the nearshore of the

Pt. Sal [60]. The San Luis Obispo (SLO) Bay is sheltered from regional northwesterly winds by the Pt. Buchon resulting in the development of an upwelling shadow zone with a warm surface flow [60]–[62]. Consistent with the previous research, the result shows that the trapped relatively warm waters transport to southward along the Pismo Beach.

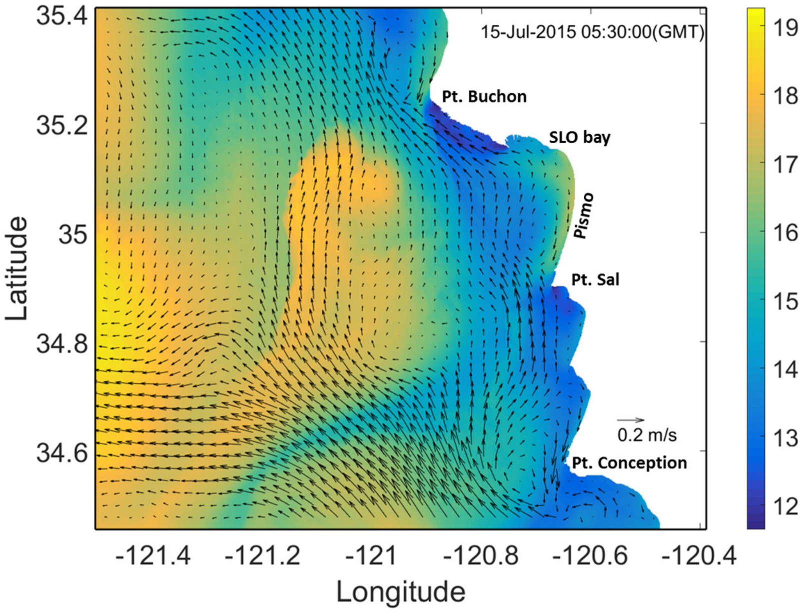

Figure 7.6. SST (color) and depth-averaged current velocity (vector with a 2km interval) snapshot on 15 July 2015, 05:30 (GMT) from the 120m grid model.

Figure 7.7(a) shows snapshots of SST and depth-averaged current velocity of L4 (40m grid) model. In order to describe the currents near the Pt. Sal, cross-sections for the North/West/South boundaries of Figure 7.7(a) are shown in Figure 7.7(b, c, d), respectively. Figure 7.7(b, d) show strong vertical shear in the alongshore flow with the poleward current near the bottom and southward flow at near the surface. The isothermal and isohaline lines are generally sloping upward toward the coast over the continental shelf. However, the consequences of coastal upwelling, offshore transport at the surface layer and onshore transport at the bottom layer, are not clearly evident in Figure 7.7(c) where the velocity in east-west direction is much weaker than in north-south direction. Vertical profiles at two sample points are compared in Figure 7.8. Both points have similar westward transport at near the surface, but Point B has no eastward current near the bottom where the V-velocity is relatively large. It is possible that the upwelling may not be sufficient to overcome the strong poleward geostrophic flow [55], which implies the existence of spatial variations of onshore transport near the bottom or other forcing mechanisms that may influence the momentum balance.

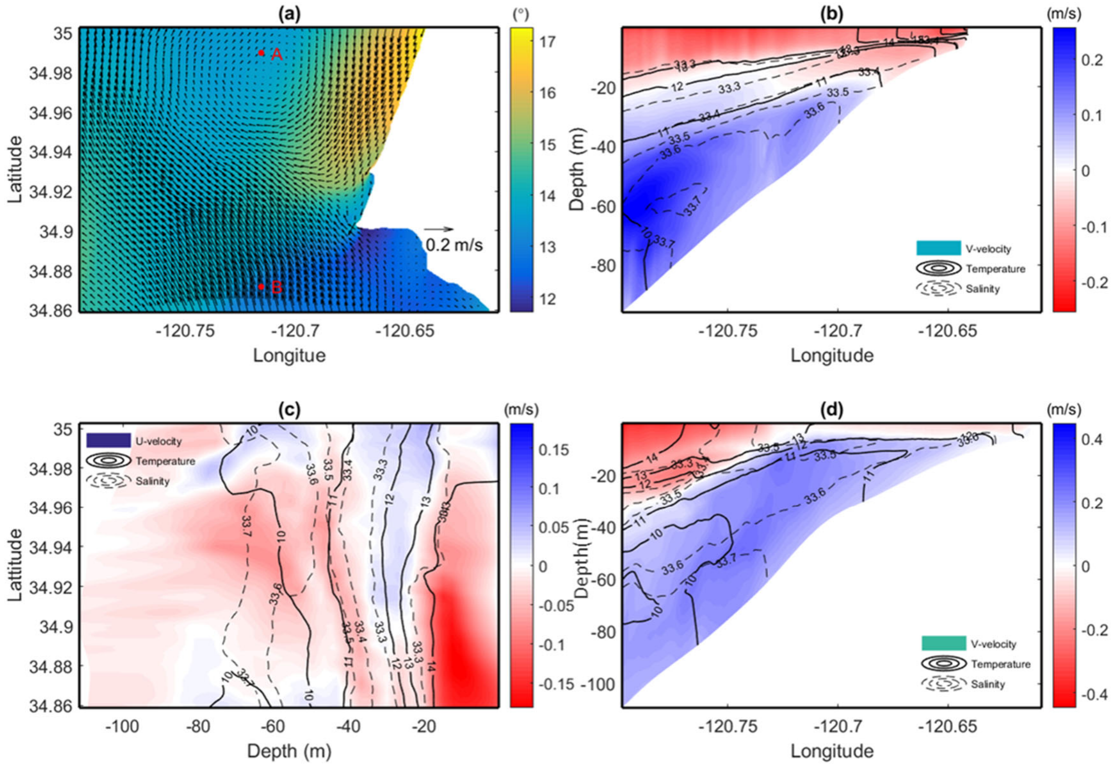

Figure 7.7. Snapshots of the current velocity, temperature and salinity fields near Pt. Sal on 15 July 2015, 05:30 (GMT) from the 40m grid model: (a) SST and depth-averaged current velocity vectors. Section profiles at the north boundary (b), west boundary (c) and south boundary (d). In the section profiles, solid-line is the isothermal, dash-line is the isohaline and color indicates northward(positive)-velocity component in (b, d) and eastward(positive)-velocity component in (c), respectively. Vertical profiles at points A and B shown in (a) are described in Figure 7.8.

The salinity and temperature profiles below the halocline and thermocline are similar at both points which means that the interior and bottom flow in this region may be defined as a single current system (California Undercurrent). On the other hand, the surface water at the two points seems to have different flow systems as the SST and salinity are quite different from each other. As shown in Figure 7.7(a), the surface near the Pt. Sal has various flow systems: relatively cold upwelling plume from the north boundary, relatively warm southward coastal jet along the Pismo Beach, cold water adjacent to the coast between the Mussel Pt. and Pt. Sal, and cold water adjacent to the coast of south Pt. Sal.

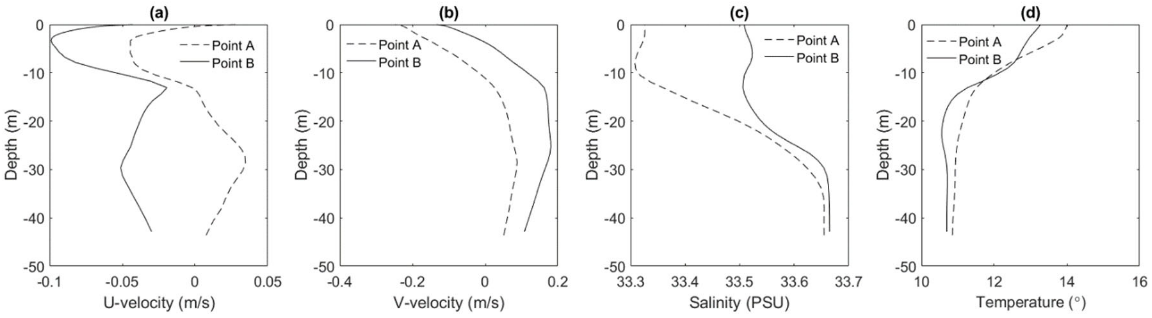

Figure 7.8. Vertical profiles of the current velocity, temperature, and salinity at the Point A (solid-line) and B (dash-line) on 15 July 2015, 05:30 (GMT) from the 40m grid model: (a) east-westward-velocity component, (b) north-south-velocity component, (c) Salinity, (d) Temperature. The locations of the points are shown in Figure 7.7.

The alongshore currents, the poleward current near the bottom and southward currents at near the surface, are clearly shown near Pt. Sal. The main body of the southward currents near the surface is the large scale coastal jet passing through the entire north and south boundaries shown in Figure 7.7(b,d). The cold upwelling plume from the Pt. Buchon (hereinafter referred to as upwelling plume) and the warm coastal jet from the SLO bay (hereinafter referred to as coastal jet) join the main body over the relatively narrow bands.

While the surface generally shows offshore transport, the cross-shore transport near the bottom depends on the location relative to Mussel Pt. and Pt. Sal.

7.2.1 Lagrangian transports

In order to assess characteristics of the circulation, particle trajectories spanning 36 hours during the detected periods are calculated and three-dimensional circulations are discussed. In this section, the characteristics of the 2015 circulations, e. g., the divergence of onshore transport near the bottom, upwelling fronts, and convergence/divergence of the surface flows are discussed. In addition, the complex surface current systems shown in Figure 7.7 and corresponding stratifications are explained.

Cross-shore Lagrangian transport

In Figure 7.9, dots and solid lines indicate the initial positions and trajectories of each particle, respectively. To avoid sharp changes in thermocline or halocline, all particles are initiated at 80% bathymetry-fallowing water depth along the 15 cross-sections spacing 1km in northward and 0.2km in eastward. Once particles are upwelled above the thermocline or halocline (approximately -5m water depth), the trajectories are defined as upwelling and marked in blue color. Consistent with the spatial variations of the onshore transport shown in geographical distributions of wind-driven changes of temperature and salinity (Figure 7.4), Figure 7.9 shows that most of the upwelling mainly occurs within the onshore side of 6km offshore from the coast. The particles initiated offshore of this boundary have less vertical movements.

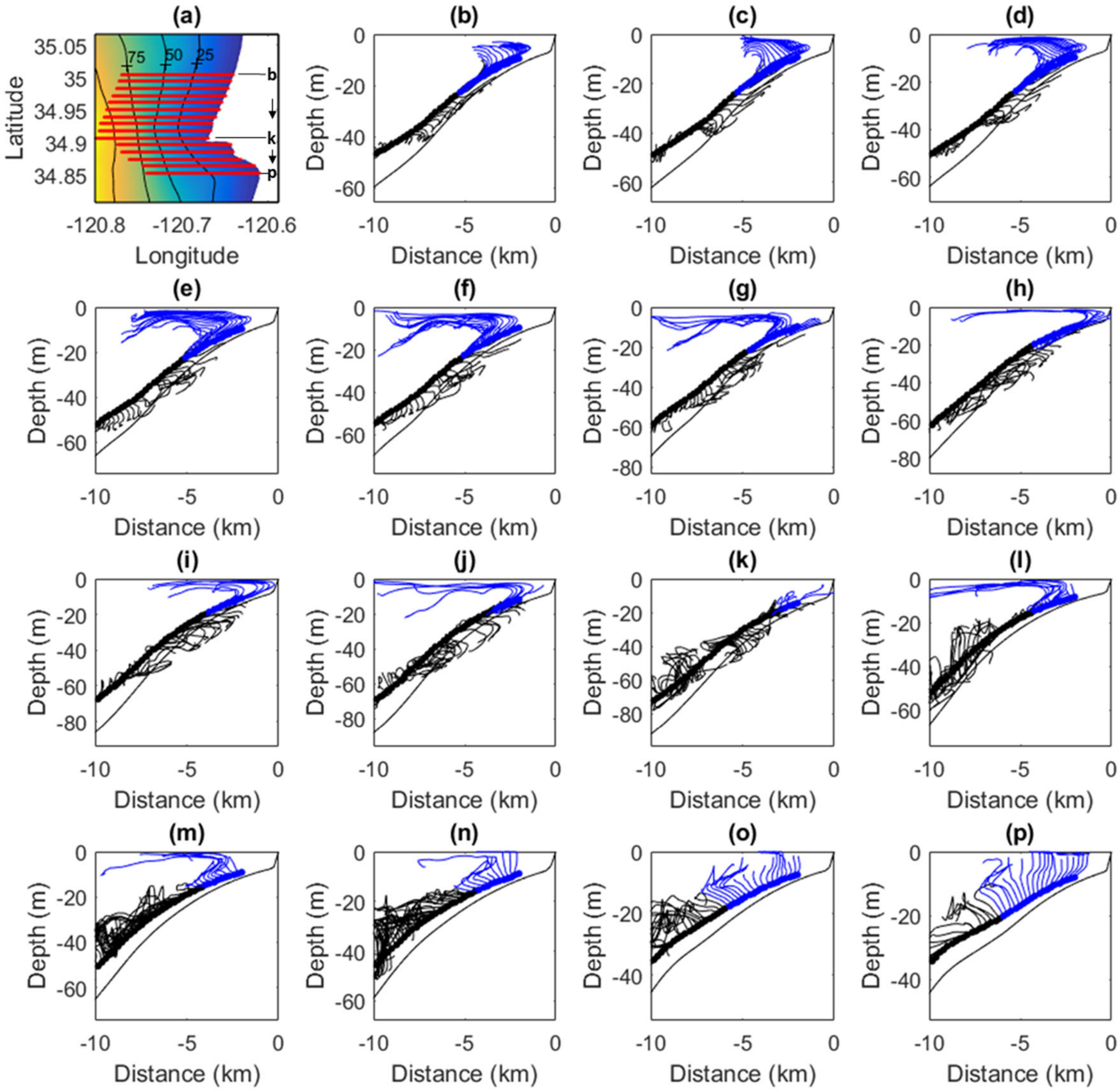

Figure 7.9. Particle trajectories during the 2015 circulation (36 hours from 14 July, 15:30 to 16 July 03:30, GMT). (a) Locations of the 15 sections (red lines). The color indicates water depth. (b-q) The trajectories initiated at 80% bathymetry-fallowing depth along the 15 sections. Upwelling is marked with blue trajectories.

The upwelled trajectories of each section show three different patterns. The upwelled particles initiated at section n-p have less eastward movement (Figure 7.9 (n-p)). The upwelled particles initiated at section i-m (southern coast of Pt. Sal, Figure 7.9 (i-m)) tend to move toward the offshore in the beginning, then the onshore in the middle and then the offshore after upwelling. The upwelled particles initiated at section b-j (northern coast of Pt Sal, Figure 7.9 (b-j)) tend to move onshore in the beginning and then offshore after upwelling. The travel distance of the upwelled particles may differ according to the speed of the currents and the distance between initial positions and upwelling locations. For example, the upwelled particles initiated at sections f and g travel more toward the offshore than the particles initiated at sections c and d during the same period. It can possibly be understood that the particles initiated at sections f and g upwell earlier than particles initiated at sections c and d. In order words, there is a possibility of the existence of an upwelling convergence area, and the sections f and g may be close to this area compared to sections c and d. The complex surface current systems and corresponding stratifications significantly affect formations of the upwelling front and convergence area.

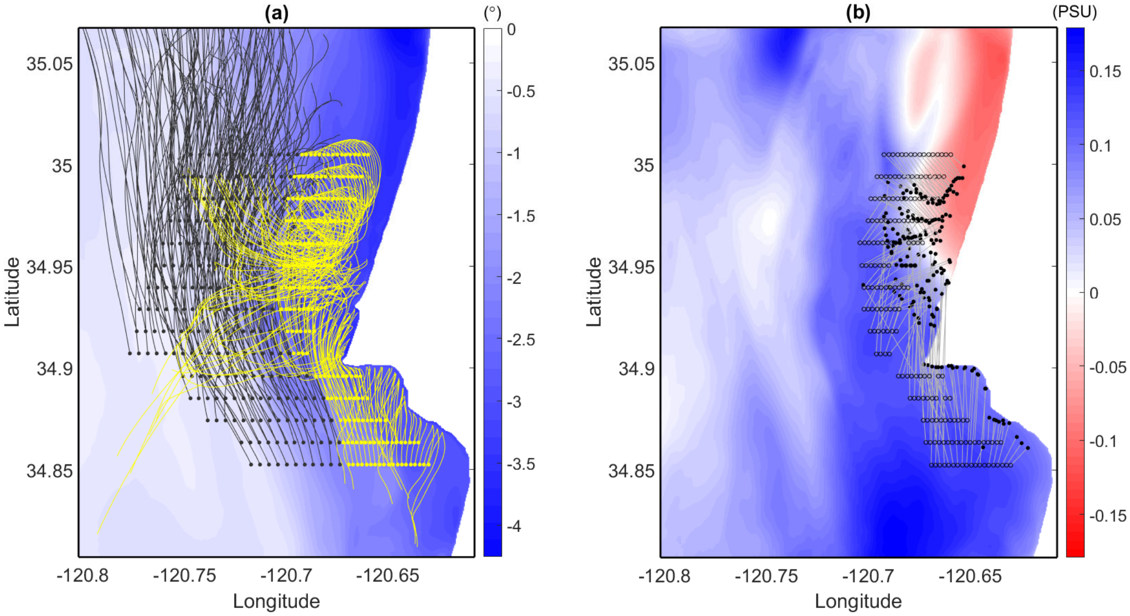

Figure 7.10. (a) Geographical distributions of particle trajectories shown in Figure 7.9. Upwelling is marked with yellow trajectories (blue in Figure 7.9). The color indicates 36 hours (trajectory period) averaged $\Delta T_{0.8}$ anomaly. (b) Geographical distributions of the initial (empty circles) and turning (filled circles) positions of the upwelling trajectories. The color indicates 36 hours averaged $\Delta S_{0.8}$ anomaly.

Plan view of Lagrangian transport

The upwelling fronts are typically identified by localized cross-shelf gradients of temperature, salinity, and density [119]. However, the particle trajectory analysis has the benefit to display the physical particle movements of the upwelling allowing visualization of the physical upwelling front. In Figure 7.10(a), the particle trajectories shown in Figure 7.9 are displayed in the two-dimensional horizontal domain where black dots are initial positions, yellow lines are upwelling trajectories (blue in Figure 7.9) and the background color indicates the $\Delta T_{0.8}$ anomaly. As seen in Figure 7.9, most upwelling trajectories are initiated at the onshore side of 6km offshore from the coast and the others are washed away by the California Undercurrent. The divergence of cross-shore transport is represented both in Lagrangian particle trajectory and Eulerian $\Delta T_{0.8}$, $\Delta S_{0.8}$ anomalies, which can be used to determine the boundary of onshore transport near the bottom.

In Figure 7.10(b), the initial (empty dots) and turning (black dots) positions of the upwelling particles are connected by grey lines. The background color indicates $\Delta S_{0.8}$ anomaly. In Figure 7.10(b), the black dots are the most onshore positions of upwelling trajectories which means that the upwelling particles transport toward onshore near the bottom and change the directions toward offshore at these positions. In this sense, these positions can be used to determine the upwelling fronts. As expected from Figure 7.9, the turning points tend to converge to the northern coast of Mussel Pt. (lat. 34.96), which is the confluence of the cold upwelling waters and warm coastal jet. Looking at grey lines in Figure 7.10(b), the particles initiated above Mussel Pt. tend to transport onshore perpendicular to the coast but slightly inclined to the south due to the southward flow along the coast. The upwelling fronts are mainly formed 2-4km offshore from the coast. The upwelling trajectories initiated below Mussel Pt. show different transport patterns along with the complex Pt. Sal coastline: 1) the particles initiated close to the boundary of the onshore transport near the bottom are transported to the convergence area, 2) less upwelling occurs between Mussel Pt. and Pt. Sal, 3) turning positions and upwelling fronts of the upwelling trajectories initiated from the southern coast of Pt. Sal are formed close to the coast.

As shown in Figure 7.10(a), the trajectories upwelled over the convergence area diverge into two offshore streams, southward flow near the surface and northward flow near 10-20m water depth (hereinafter referred to as the lower surface). This divergence is also shown vertically in Figure 7.9(e-g). Note that the vertical mixing generated by the meeting of the two opposite currents may force parts of upwelled particles to lower surface where the poleward alongshore current is strong. The upwelled particles at the southern coast of Pt. Sal are transported away from the coast to the southwest direction. Therefore, the surface current separate into two flows: relatively strong southwest-ward flow from the upwelling convergence area and weak southwest-ward flow from the southern coast of Pt. Sal.

7.2.2 Surface currents and stratification

The characteristics of the 2015 circulation obtained in this section, e.g., boundaries of onshore transport near the bottom, upwelling fronts, convergence/divergence of the surface flow, can contribute to discussions of the complex surface currents near the Pt. Sal. The spatial and temporal variations of the stratification are greatly influenced by the surface currents and thus coastal upwelling, surface currents, and stratification cannot be analyzed separate from each other. Figure 7.11(a) shows the 36 hours averaged SST and current velocity vectors. The arrow boxes indicate difference surface flow systems and blue lines indicate SST fronts. From the north boundary, the relatively cold upwelling jet (S1) generated remotely from this area (Pt, Buchon) and warm coastal jets (S2) from the upwelling shadow zone pass through the nearshore of Pt. Sal. The coastal upwelling fronts are aligned between the two distinct flows and contribute to creating a SST front (F1). The warm coastal jet (S2) and upwelled cold water at the upwelling convergence area are merged into (S3) flow. The relatively cold water (S4) upwelled near the Mussel Pt. coast creates a SST front (F2) bordering the flow in (S3). The cold water (S5) ranging from 12 to 13 degree upwelled at the southern coast of Pt. Sal flows toward the south and forms another surface temperature and velocity front (F3) bordering the flow in (S4). The surface flows (S1, S3, S4) merge offshore of Pt. Sal and continues toward the southwest.

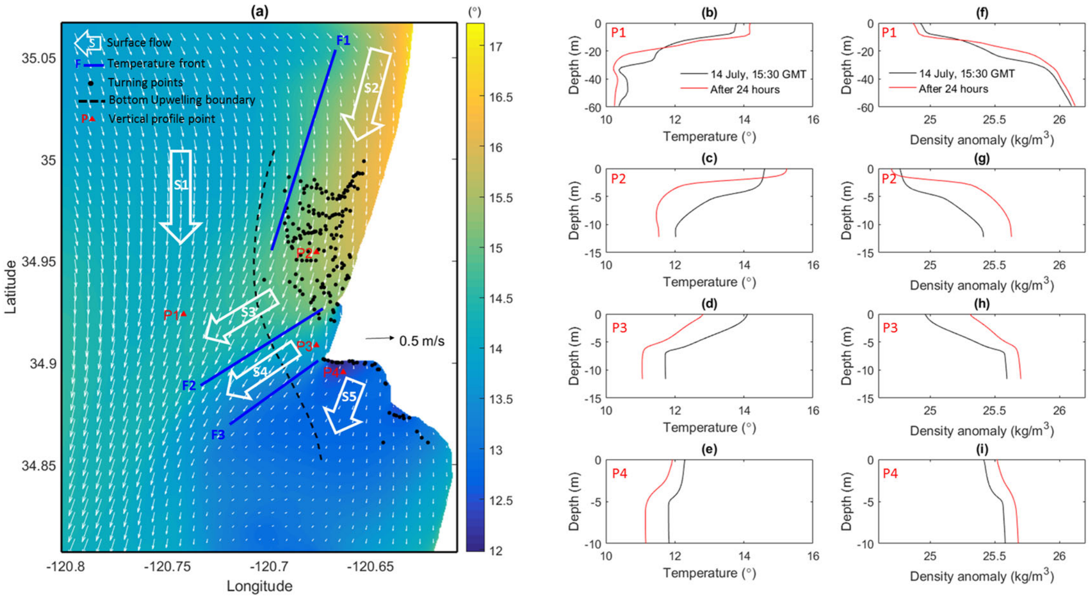

Figure 7.11. (a) 36 hours averaged SST (color) and surface current (white vector). The arrow boxes are different surface flow systems and the blue solid-line indicates SST fronts. The black dot indicates the turning position of the upwelled particles and the black dash-line indicates the boundary of the onshore transport near the bottom shown in Figure 10(b). (b-i) Two vertical temperature and density anomaly profiles at the beginning (black) and 24 hours later (red) of the particle tracking for four locations.

In order to describe the relationship between the coastal upwelling and stratification, two vertical profiles of temperature and density anomaly, at the beginning (black) and 24 hours later (red) of the particle tracking for different locations (P1-P4 in Figure 7.11(a)) are shown in Figure 7.11(b-i).

At P1 located outside of the boundary for the near bottom onshore transport, the temperature and density anomaly profiles are generally maintained during the circulation. Consistent with the results mentioned before, no upwelling effects are shown in this location. The P2 and P3 show similar initial profiles but remarkably different later profiles. At P2 located at the upwelling convergence area, the temperature decreases and density increases over the depth except for near the surface. Note that the upwelling favorable wind in this region contributes not only to feeding the upwelled cold water but to boosting the warm water jet (S2) at the same time. Therefore, these two different processes make larger stratifications or gradients of temperature and density, which explain the wind stress driven salinity drops shown in Figure 7.4(f). In this location, the thermocline and pycnocline rise upward during the upwelling event. On the other hand, the temperature decreases and density increases over the entire depth at the P3 located at the pocket between Mussel Pt. and Pt. Sal. The P2 and P3 are close to each other, but the warm coastal jet from the upwelling shadow zone dominates the P2 surface and the upwelled cold water dominates the P3 surface due to a rocky promontory of the Mussel Pt.. Notably, the stratification at the P4 located at the southern coast of the Pt. Sal is remarkably weak and the changes during the circulation are relatively uniform over the depth, resulting in very little stratification change.

7.3 Circulation momentum analysis

The goal of this section is to identify the forcing mechanisms of the circulation patterns using the cross-shore and alongshore momentum balances. Various forcing mechanisms affecting the coastal circulation are listed and projected onto the three-dimensional momentum balance at three cross-sections.

7.3.1 Forcing mechanisms

Relevant processes affecting mixing and the transport of water masses across the nearshore include rip currents [120], shoaling and breaking NLIWs [121]–[123], semidiurnal internal tides [124], wind and wave-driven circulation [14], subtidal rotation influenced processes [125], and turbulence generated in the boundary layer [126], [127]. This study focuses on understanding the structures of circulations driven by the alongshore and cross-shore wind stresses, California Undercurrent, coastal jets, upwelling plume, bathymetry, and the coastline promontory near Pt. Sal.

A baroclinic alongshore pressure gradient derived from remotely forced coastal trapped waves, sea level setup by coastal winds or density gradients [68] can drive a poleward California Undercurrent [69], [70]. The strong cross-shore Coriolis force from the California Undercurrent can create an alongshore geostrophic flow if the Coriolis force balances an offshore-directed pressure gradient force. Gómez et. al (2017) [128] explains that strong offshore-directed pressure gradients strengthen the California Undercurrent and weaker pressure gradients make the undercurrent feeble and intermittent along the inner shelf. The extended California Undercurrent with a poleward decrease in temperature also drives an alongshore pressure gradient force in the lower portion of the water column which in turn generates an offshore geostrophic flow by balancing with the alongshore Coriolis force [129].

The southward coastal jets along Pismo beach plays three different roles in the circulation at the nearshore region: the offshore Coriolis force driven by the strong alongshore coastal jets can balance the onshore pressure gradient force and strengthens the coastal jets. In addition, the warm jet with a southward decreases in temperature creates an alongshore pressure gradient force in a north direction which in turn generates an onshore geostrophic flow by balancing the alongshore Coriolis force. On the other hand, the pressure gradient force in a south direction can be observed and generate an offshore geostrophic flow because the model result shows that the sea level is elevated toward the SLO bay during the 2015 circulation. The southward cold upwelling plume adjacent to the Pt. Buchon also creates the alongshore pressure gradient and forces offshore geostrophic flows by balancing the Coriolis force near the surface. The warm coastal jet and cold upwelling plume with the opposite temperature gradient in alongshore direction can result in a divergence of cross-shore transport along the boundary between the two and thereby form the upwelling convergence area. The southward wind stress over the Pt. Sal nearshore plays two roles in driving cross-shore circulations: the alongshore winds generate vertical shear stresses, which are balanced by the Coriolis force near the surface, and force offshore Ekman transport at the surface layer [16]. On the other hand, the alongshore winds also force onshore transport through the entire water column where the water piles up at the downwind coast and a northward alongshore pressure gradient grows [130], [131]. This pressure gradient and Coriolis force balance and create the onshore geostrophic flow.

Therefore, the cross-shore circulation driven by the alongshore wind in this region can show opposite reactions depending on the alongshore Coriolis force.

The onshore wind stress plays different roles at offshore and nearshore regions; the alongshore Ekman transport in a south direction is generated from the balance between the cross-shore vertical stress and Coriolis force. However, Tilburg (2003) [65] show a cross-shelf momentum balance is not geostrophic in water shallower than about 25 m. The water near the surface moves onshore and piles up at the coast where a cross-shore pressure gradient grows to balance the wind stress and drives an offshore return flow in the lower portion of the water column [67], [132].

In the nearshore region, the alongshore currents pass over an offshore directed ridge adjacent to the headland of Mussel Pt., resulting in the sea level decrease at the promontory area. Mussel Pt. is a small (350m), rocky promontory 3 km north of Pt. Sal. Offshore of Mussel Pt, there is a nearly circular submerged rocky outcrop approximately 2 km in diameter. Mussel Pt. extends 350 m in the alongshore direction, and protrudes 350 m seaward. Warner et al. (2014) showed that an alongshore flow creates pressure gradients due to the setdown of water level on the crest of a shoreface-connected ridge [133]. The alongshore pressure gradient force is directed to the promontory area and balanced with the Coriolis force, resulting in off/on-shore geostrophic flows at the northern side and southern side, respectively.

The physical processes listed above occur simultaneously and the circulation may be amplified or offset by a combination of these mechanisms. The mechanisms are simplified and tabulated in Table 7.2 by indicating the factor and direction of forcing source (red), necessary condition (blue), and resultant circulation (black). The forcing sources (red) directly cause the corresponding momentum force and the resultant circulations (black) are expected to depend on the necessary conditions (blue). Various combinations among the mechanisms may be applied at different locations depending on the distance from the coast and water depth.

Table 7.2. The mechanisms influencing the circulation near Pt. Sal during the selected period. Abbreviations indicate circulation (Cir.), Coriolis force (C), pressure gradient force (P), vertical mixing (V). The signs indicate directions of the circulation and each momentum term where "+/-" is toward north/south and onshore/offshore in alongshore and cross-shore direction, respectively. The color indentifies the forcing source (red), necessary condition (blue), and resultant circulation (black).

No	Factor	Forcing source	Alongshore				Cross-shore			
			Cir.	C	P	V	Cir.	C	P	V
1	California Undercurrent	Alongshore velocity	+					+	-	
2	California Undercurrent	Temperature grad.		+	-		-			
3	Coastal jet	Alongshore velocity	-					-	+	
4	Coastal jet	Temperature grad.		-	+		+			
5	Coastal jet	Sea level grad.		+	-		-			
6	Upwelling plume	Temperature grad.		+	-		-			
7	Alongshore wind	Wind stress		+		-	-			
8	Alongshore wind	Sea level grad.		-	+		+			
9	Cross-shore wind	Wind stress	-					-		+
10	Cross-shore wind	Sea level grad.					-		-	
11	Promontory	Sea level grad.(up)		+	-		-			
12	Promontory	Sea level grad. (down)		-	+		+			

7.3.2 *Momentum balance*

The dominant mechanisms influencing the circulation at different locations are identified by linking the three-dimensional momentum balance. ROMS diagnostic outputs are utilized to examine the detailed dynamics of the circulation response that occurred during the selected period. Equations (7.1) and (7.2) express the dominant terms in the momentum balance in the cross-shore and alongshore directions, respectively.

$$\underbrace{\frac{\partial u}{\partial t}}_{Acc.} = \underbrace{fv}_{C} - \underbrace{\vec{v}\cdot\nabla u}_{A} - \underbrace{\frac{\partial \phi}{\partial x}}_{P} - \underbrace{\frac{\partial}{\partial z}\left(\overline{u'w'} - \nu\frac{\partial u}{\partial z}\right)}_{V} \tag{7.1}$$

$$\underbrace{\frac{\partial v}{\partial t}}_{Acc.} = -\underbrace{fu}_{C} - \underbrace{\vec{v}\cdot\nabla v}_{A} - \underbrace{\frac{\partial \phi}{\partial y}}_{P} - \underbrace{\frac{\partial}{\partial z}\left(\overline{v'w'} - \nu\frac{\partial v}{\partial z}\right)}_{V} \tag{7.2}$$

The left-hand side is the acceleration term (Acc.). The right-hand side including four dominant terms, Coriolis force (C), nonlinear advection (A), pressure gradient force (P), and vertical mixing (V), is decomposed in Figure 7.12 for the three cross-sections shown in Figure 7.13.

The velocity fields can be inferred from the Coriolis terms, e.g., the cross-shore Coriolis momentum term is a function of alongshore velocity. As shown in Figure 7.12, the cross-shore momentum terms are more dynamic than those in the alongshore direction, except the advection term. Although the inner shelf flow fields are often dominated by energetic alongshore currents, cross-shore gradients in most properties (i.e. temperature, salinity, or dissolved materials) are usually far stronger than those in the alongshore direction [119]. The Coriolis force momentum terms in cross-shore direction, Figure 7.12.a(C), show two distinct layers of alongshore flow where the surface flow is generally balanced by both pressure gradient force, Figure 7.12.a(P), and vertical mixing, Figure

7.12.a(V). Figure 7.12.a(C) near the bottom, however, are predominately balanced with the pressure gradient force. Note that the advection term in cross-shore direction is generally weaker than the other terms, although it increases for profile 3 closer to Pt. Sal. While the cross-shore momentum balances show similar patterns for the different cross-sections, the alongshore momentum balances have different patterns for each cross-section. For section 1, the pressure gradient force (Figure 7.12.b1(P)) generally balances the Coriolis force (Figure 7.12.b1(C)) except for a lower surface layer where the Coriolis force is balanced with the vertical mixing (Figure 7.12.b1(V)). Although the vertical mixing (Figure 7.12.b2-3(V)) still balances the Coriolis force (Figure 7.12.b2-3(C)) at section 2 and 3, these sections are largely dominated by the geostrophic balance. While the alongshore Coriolis force at section 2 (Figure 7.12.b2(C)) clearly shows the divergence of the onshore transport near the bottom, the onshore transport is not present for section 3 (Figure 7.12.b3(C)).

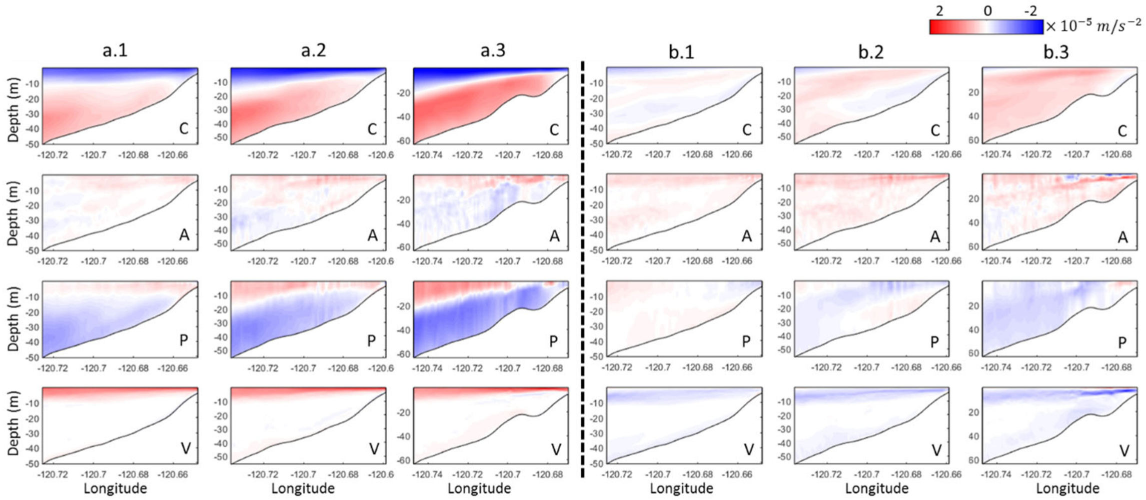

Figure 7.12. (a) cross-shore momentum terms, (b) alongshore momentum terms for the cross-section (1), section (2), and section (3) where (C) is Coriolis force, (A) is nonlinear advection, (P) is pressure gradient force, and (V) is vertical mixing. Colors indicate 24 hours averaged momentum terms during the 2015 circulation.

In order to diagnose the momentum balances for the circulation in more detail, the forcing mechanisms listed in Table 7.2 are linked to the momentum fields and dominant mechanisms are identified for different regions in the cross-sections. The cross-section is roughly divided into six sectors: offshore, inshore, and mid-shore between the two, as well as near the surface and bottom.

[Offshore near surface]

This location is affected by the upwelling plume, alongshore wind, and cross-shore wind (6-9, Table 7.2). The southward alongshore flow is driven by the Ekman transport generated by the cross-shore wind stress (mech 9), at all cross-sections where the cross-shore Coriolis force (Figure 7.12.a(C)) and vertical mixing (Figure 7.12.a(V)) balance. The alongshore Coriolis force in cross-section 1 and 2 (Figure 7.12.b1-2(C)) shows two-layered surface flow, the upper surface from the surface to 10m and the lower surface from 10m to 20m water depth. Most of the surface flow can be explained by the onshore geostrophic flow generated from the alongshore wind stress (mech 8). As the alongshore Coriolis force is southward in this location, the southward forcing from the pressure gradient and vertical mixing induced by the spatial variation in the temperature (mech 6) and alongshore wind stress (mech 7) is reduced by the wind induced alongshore pressure gradient (mech 8). The lower surface flow in section 1 can be explained by the offshore Ekman transport generated from the alongshore wind stress (mech 7). In addition to the alongshore wind stress (mech 7), the spatial variation in temperature also contributes to the lower surface flow in section 2 where the southward cold upwelling plume leads to the offshore geostrophic flow (mech 6). Unlike cross-section 1 and 2, section 3 shows a single surface flow which can be explained by the offshore geostrophic flow (mech 6) and Ekman transport (mech 7).

[Mid-shore near surface]

This location is affected by the coastal jet, upwelling plume, alongshore and cross-shore wind (3-9 Table 7.2). Like the offshore near surface location, here the southward alongshore flow is also driven by the Ekman transport induced from the cross-shore wind (mech 9) at all cross-sections. In addition to the cross-shore wind, the coastal jet also contributes to the southward alongshore flow by adding the cross-shore Coriolis force in this location (mech 3). The two-layered surface flow in the cross-shore direction discussed in the offshore near surface is observed in cross-section 1. The upper portion of the surface flow can be explained by the geostrophic flows where the alongshore pressure gradient force induced by the temperature gradient from the coastal jet (mech 4) and sea level gradient from the alongshore wind (mech 8) contributes to the onshore flow. In the lower surface layer at the cross-section 1, the upwelling plume dominates and results in the offshore geostrophic flow induced from the temperature gradient (mech 6). The cross-shore surface flow at the cross-section 2 and 3 can be explained by the geostrophic flow induced from the coastal jet (mech 5) as well as the geostrophic flow (mech 6) and Ekman transport (mech 7). The southward alongshore pressure gradient force is added by the elevated southward costal jet and contributes to the offshore geostrophic flow (mech 5).

[Inshore near surface]

This location is affected by the coastal jet, alongshore and cross-shore wind, and promontory (3-5, 7-9, 11-12, Table 7.2). Like the mid-shore near surface location, the southward alongshore flow can be explained by the geostrophic flow induced by the coastal jet (mech 3) and Ekman transport induced by the cross-shore wind (mech 9) at all cross-sections. Note that the driving source for the southward alongshore flow near the surface gradually migrates from the cross-shore wind stress at the offshore to the coastal jets at the inshore. The cross-shore flow shows a similar pattern at the cross-section 1 and 2 where the southward pressure gradients induced by the northward sea level gradient from the coastal jet (mech 5) and promontory (mech 11), and southward vertical mixing induced by the alongshore wind (mech 7) contribute to the offshore flow. The southward alongshore pressure gradient force is added by the setdown of water level on the promontory area resulting in the offshore geostrophic flow (mech 11). The cross-section 3, however, is dominated by the coastal jet (mech 5) and alongshore wind (mech 7) where the northward alongshore pressure gradient force generated from the setdown on the promontory area (mech 12) may be offset by the mech 5 and 7. This promontory also plays an important role in the stratification. The coastal jet increases the surface temperature at P2 (Figure 7.11(c)) and results in increasing the stratification at P2. On the other hand, the P3 is sheltered from the warm coastal jets by the coastal promontory resulting in the temperature drop (Figure 7.11(d)) near the surface where the cold upwelled waters forced by the geostrophic flows from the coastal jet (mech 4) and alongshore wind (mech 8) create the temperature front from the warm coastal jets.

[Offshore near bottom]

This location is affected by the California Undercurrent and alongshore wind (1, 2, 8, Table 7.2). The northward alongshore flow can be explained by the geostrophic flow generated from the California Undercurrent (mech 1) at all cross-sections where the cross-shore Coriolis force (Figure 7.12.a(C)) and pressure gradient force (Figure 7.12.a(P)) balance. The offshore flow at the cross-section 2 and 3 can be explained by the geostrophic flow where the temperature gradient from the California Undercurrent induces offshore flow (mech 2). On the other hand, the geostrophic flow induced by the pressure gradient force from the alongshore wind (mech 8) dominates at cross-section 1 and forces the onshore transport. Note that the interaction between the alongshore wind stress and California Undercurrent determines the cross-shore transport near the bottom in this location. Due to the steadiness of California Undercurrent during the selected period, the time evolution of the temperature structure near the P1 bottom is weak as shown in Figure 7.11(b).

[Mid-shore near bottom]

This location is affected by the California Undercurrent, coastal jet, and alongshore wind (1, 2, 5, 8, Table 7.2). Like the offshore near bottom location, the northward alongshore flow can be explained by the geostrophic flow induced by the Coriolis force from the California Undercurrent (mech 1) at all cross-sections. The onshore transport at cross-sections 1 and 2 can be induced by the sea level gradient from the alongshore wind (mech 8). On the other hand, the temperature gradient induced by the California Undercurrent (mech 2) and sea level gradient from the coastal jet (mech 5) create the southward alongshore pressure gradient force, resulting in the offshore geostrophic flow at the cross-section 3. These opposite forcing mechanisms form the divergence of the cross-shore transport near the bottom shown in Figure 7.11(a) and control the upwelling circulation.

[Inshore near bottom]

This location is affected by the California Undercurrent, coastal jet, alongshore and cross-shore wind, and promontory (1-5,7,8,10-12 Table 7.2). Like the mid-shore near bottom location, the northward alongshore flow can be explained by the geostrophic flow induced by the California Undercurrent (mech 1) at all cross-sections. In addition to the alongshore wind (mech 8), the temperature gradient induced by the coastal jet creates alongshore pressure gradient force (mech 4) and contributes to the onshore transport at the cross-section 1 and 2. In addition to the southward pressure gradient force from the temperature gradient induced by the California Undercurrent (mech 2) and sea level gradient from the coastal jet (mech 5), the southward vertical mixing induced by the alongshore wind (mech 7) force the offshore transport at cross-section 3. The onshore wind piles up the water at the coast and drives the offshore return flow near the bottom of the water column (mech 10). As shown in Figure 7.11(c,d,e), the northward alongshore current passing through the cross-section 2 and 3 cool down during the selected period and the stratifications at P2 and P3 are increased. The geostrophic flow induced by the coastal jet (mech 4) and alongshore wind (mech 8) transports relatively cold waters to the bottom at the cross-section 2 (P2), enhancing the stratification.

7.3.3 Dominant forcing mechanisms

The dominant forcing mechanisms influencing the circulation at each location are illustrated in Figure 7.13. The alongshore circulation near the bottom is mainly derived from the extended undercurrent, the geostrophic flow generated by the Coriolis force of the California Undercurrent (mech 1). The southward alongshore flow can be explained by the Ekman transport induced from the cross-shore wind (mech 9) at all cross-sections. In addition to the cross-shore wind, the coastal jet also contributes to the southward alongshore flow by adding the cross-shore Coriolis force in this location. The Ekman transport induced by the cross-shore wind (mech 9) and geostrophic flow enhanced by the coastal jet (mech 3) dominate the alongshore circulation near the surface for the three cross-sections; the Coriolis force from the coastal jets balances the pressure gradient force and derives the alongshore geostrophic flows (mech 3) at the inshore region. On the other hand, the alongshore Ekman transport generated by the cross-shore wind stress (mech 9) dominates the offshore region. Unlike the alongshore circulation, the cross-shore circulation shows different combinations of the mechanisms for the cross-sections. The cross-section 1 and 2 located at the northern coast of the Mussel Pt. shows the onshore geostrophic transport near the bottom, which is forced by the pressure gradient from warm coastal jet (mech 4) and alongshore wind stress (mech 8). The cross-section 3 located at the southern coast of the Mussel Pt., however, shows the offshore geostrophic transport near the bottom due to the warm California Undercurrent (mech 2) and elevated coastal jet (mech 5). The cross-shore transport near the surface also shows both onshore and offshore flow; the offshore surface located at the northern coast of the Mussel Point shows the onshore geostrophic flow induced by the coastal jet (mech 4) and alongshore wind (mech 8). Looking at the gray arrows in Figure 7.13(b), these locations show offshore transport near the lower surface, which is the combination of the geostrophic flow induced by the cold upwelling flume (mech 6) and Ekman transport induced by the alongshore wind stress (mech 7). The other surface regions show offshore transport with various combinations of the geostrophic flows induced by the coastal jet (mech 5), upwelling plume (mech 6), and promontory (mech 11) and the Ekman transport induced by the alongshore wind (mech 7).

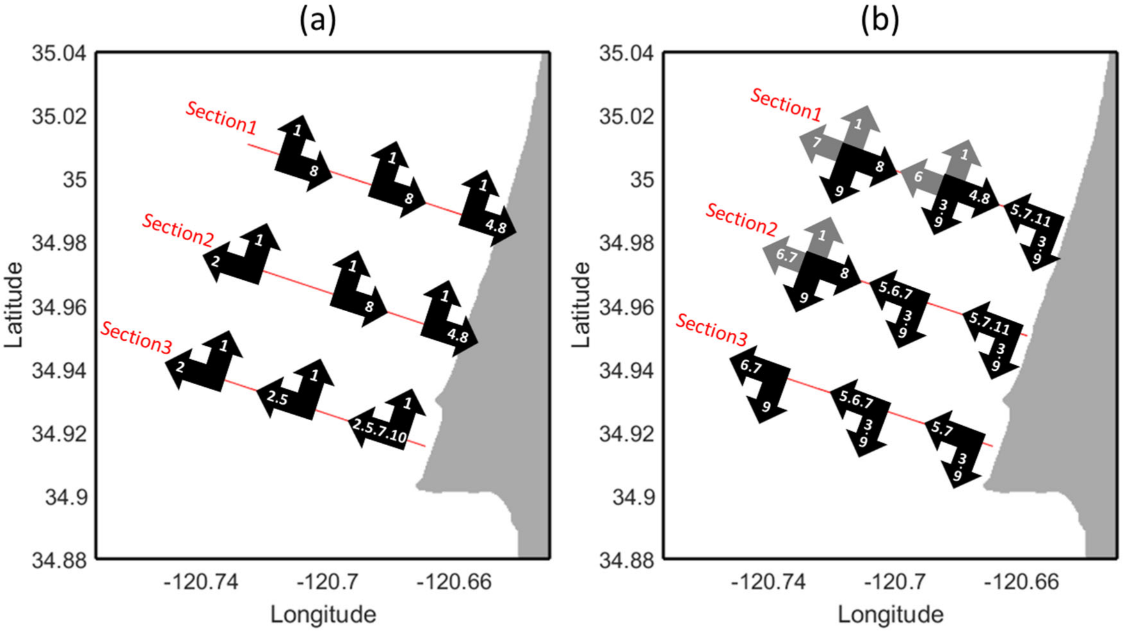

Figure 7.13. Dominant forcing mechanisms influencing the circulation during the selected period for three cross-sections (red) near the bottom (a) and surface (b) of the water column. Arrows indicate the direction of the alongshore and cross-shore circulation at each location and numerals in the arrows indicate the alongshore and cross-shore components of dominant forcing mechanisms at each location. The gray arrows in (b) indicate the lower surface flow. Note that the arrows are not scaled in magnitude or direction of the circulation.

7.4 Comparison with circulation in July 2017

The 2017 circulation is discussed by highlighting difference from the 2015 circulation. Particle trajectories spanning 36 hours during the 2017 circulation are calculated and the characteristics of the circulations are illustrated in Figure 7.14. The current system is generally very similar to the 2015 circulation; the bottom is dominated by the California Undercurrent and the surface is the confluence of the warm coastal jet and upwelling plumes.

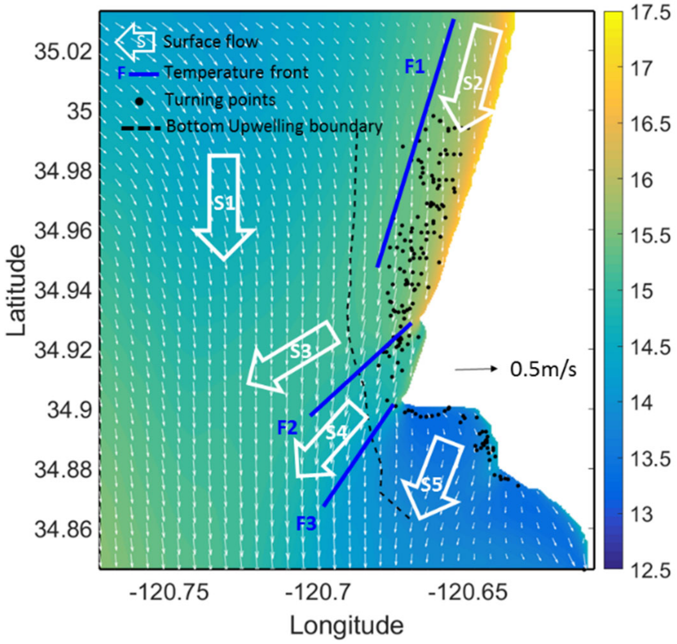

Figure 7.14. Thirty six hour averaged SST (color) and surface current (white vector) during the 2017 circulation. Descriptions are identical to Figure 7.11(a).

Looking at the surface current passing through the Mussel Pt. and Pt. Sal, a portion of the cross-shore component is increased compared to the 2015 circulation where the surface current is more parallel to the coastline. Note that wind directions in 2017 circulation are generally more normal to the coast. Another distinct difference between the two events is that the temperature front (F1) formed by the warm coastal jet is shifted close to the coast compared to the 2015 circulation (Figure 7.11(a)), resulting in a shifted upwelling front toward the coast. The boundary of the upwelling near the bottom is also shifted closer to the coast because the increased cross-shore wind stress forces the offshore return flow in the lower portion of the water column [67], [132] and can offset the onshore transport. In addition, the upwelling convergence shown in the 2015 circulation is not formed and the turning points of upwelling trajectories (black dots in Figure 7.14) are distributed along the inshore side of SST front (F1).

In order to diagnose the different circulation patterns, the momentum balances for the three cross-sections are also examined in Figure 7.15. Like the momentum fields of the 2015 circulation (Figure 7.12), the cross-shore momentum terms are more dynamic than those in the alongshore direction. The Coriolis force, advection, and vertical mixing show similar patterns to the 2015 circulation. Notably, alongshore currents are weaker than those in 2015 circulation as shown in cross-shore Coriolis force (Figure 7.12.a(C) and Figure 7.15.a(C)), which explains the weakened coastal jet. The surface layer influenced by the cross-shore wind stress (vertical mixing, Figure 7.15.a(V)) is thicker than those in 2015 circulation. The most remarkable difference in the momentum field is that the pressure gradient forces near the surface change directions in both the cross-shore and alongshore momentum terms (Figure 7.12.(P) and Figure 7.15.(P)). The cross-shore pressure gradient is not balanced with the Coriolis force near the surface and thereby the alongshore geostrophic flow shown in the 2015 circulation is no longer present in the 2017 circulation. While the alongshore surface flow in 2015 circulation consists of the geostrophic flow and Ekman transport, the alongshore surface flow in 2017 circulation is mainly dominated by the Ekman transport. In the alongshore momentum terms (Figure 7.15.b), the geostrophic balance near the surface is also reduced and the vertical mixing (Figure 7.15.b(V)) contributes to generating cross-shore Ekman transport.

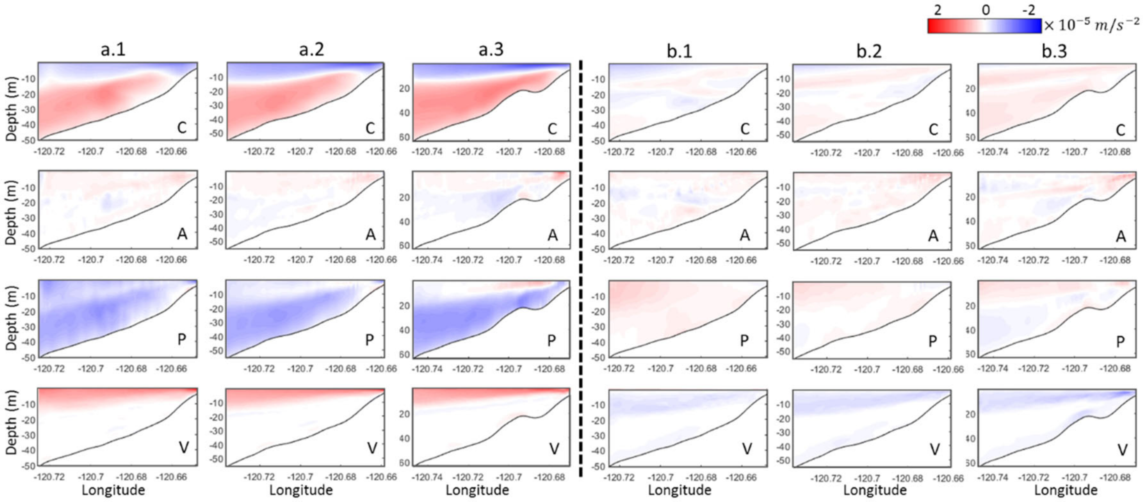

Figure 7.15. Twenty four hours averaged momentum terms during the selected period on Jul 2017. (a) cross-shore momentum terms, (b) alongshore momentum terms for the cross-section (1), section (2), and section (3) where (C) is Coriolis force, (A) is nonlinear advection, (P) is pressure gradient force, and (V) is vertical mixing.

The forcing mechanisms listed in Table 7.2 are linked with the momentum fields of the 2017 circulation and illustrated in Figure 7.16 and mechanisms driving the difference circulation patterns are identified. The dominant forcing mechanisms influencing near the bottom are almost identical to the 2015 circulation as shown in illustrated in Figure 7.16(a) except the mid-shore at cross-section 3 where the offshore geostrophic flow induced by the coastal jet (mech 5) is reduced. The offshore flow at the lower surface (gray arrows in Figure 7.16(b)) is forced by the alongshore wind stress (mech 7) and the southward upwelling plume (mech 6) may not contribute to the offshore flow. While the alongshore flow at the surface in 2015 circulation is dominated by the Ekman transport driven by the cross-shore wind (mech 9) for the offshore region and by the extended coastal jets (mech 3) for the inshore region, the surface flow in the 2017 circulation is mainly governed by the cross-shore wind (mech 9) because the portion of the cross-shore component of wind stress is increased and the coastal jet is slowed down. As shown in the cross-shore flow near the surface, the influences of the coastal jet (mech 4 and 5) are also remarkably decreased.

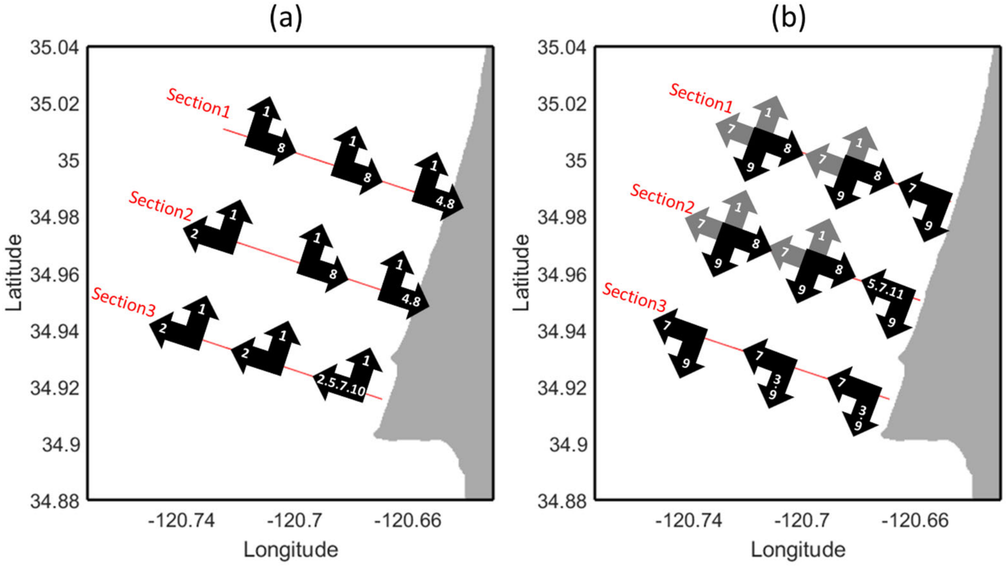

Figure 7.16. Dominant forcing mechanisms influencing the circulation during the selected period for three cross-sections (red) near the bottom (a) and surface (b) of the water column. The description is identical to Figure 7.13.

7.5 Summary

Nested grids for the Regional Ocean Model (ROMS) are configured to simulate the three-dimensional circulation during a coastal upwelling event at Pt. Sal, CA. In order to select the coastal upwelling period, two model results, including wind and excluding wind stresses, are simulated for June-July 2015 and July-September 2017. By comparing the two results, the coastal upwelling events on 15 July 2015 and 22 July 2017 are selected based on indices indicating the wind-driven changes of salinity and temperature near the bottom. Consistent with the typical impacts of the upwelling, the largest drop in temperature and the largest increase in salinity near the bottom simultaneously occur on the selected periods among the entire simulation period. The model result including wind stress shows that the water column is dominated by the northward California Undercurrent near the bottom and southward coastal jet and upwelling plume near the surface during the select periods. Particle trajectories during the coastal upwelling are calculated to describe the characteristics of three-dimensional circulations near Pt. Sal. The circulation patterns are diagnosed by projecting basic forcing mechanisms influencing the circulation, e.g., wind stresses, currents, bathymetry, onto the three-dimensional momentum balance at different locations. The dominant forcing mechanisms acting on two different circulations are identified and discussed.

For the 2015 circulation, the onshore transport near the bottom are limited to 5km nearshore from the coast and the trajectories initiated offshore of this boundary are washed away. The upwelling front shows the alongshore variability; the front forms at 2~4km from the coast at the north of Pt. Sal and the front is formed close to the coast at the north of Pt. Sal. The convergence of the upwelling front forms at the north of Mussel Pt., a confluence region of the surface current systems including the warm coastal jets from the upwelling shadow zone, cold upwelling plumes from Pt. Buchon, and upwelled cold water near the Pt. Sal. The different currents passing through the complex bathymetry and coastline result in the spatial variation of the stratification. The alongshore circulation near the bottom is mainly forced by northward geostrophic balanced between cross-shore Coriolis and pressure gradient force while the southward surface is forced by the combination of the Ekman transport (driven by the cross-shore wind stress) and geostrophic flow (driven by the coastal jet). The cross-shore circulation near the bottom is a balance of the opposing forces, offshore transport (driven by the alongshore temperature gradient from California Undercurrent, sea level gradient from the coastal jet and cross-shore wind stress, and alongshore wind stress) and onshore transport (driven by the alongshore temperature gradient from the coastal jet, and sea level gradient from the alongshore wind stress). The dominant forcing mechanisms among these opposing forces offset the other forces and determine the directions of the cross-shore transport and explain the divergence of the cross-shore transport near the bottom as shown in Figure 7.11. The offshore transport dominates the surface where the pressure gradient force (driven by the sea level gradient from the elevated coastal jet and temperature gradient from the upwelling plume originated from the Pt. Buchon) and vertical mixing from alongshore wind stress are balanced with the Coriolis force and derive offshore geostrophic and Ekman transport, respectively. In addition, the southward alongshore pressure gradient generated by the promontory contributes to the offshore transport at the inshore surface along the north of Mussel Pt.

In the 2017 circulation, the overall pattern is quite similar to the 2015 circulation but two noticeable differences are found that the wind direction are more normal to the coast and the coastal jet is weaker than those in the 2015 circulation. As the alongshore component of wind stress at the SLO port decreases, the coastal jet and its influence are tempered down. The offshore transport losses the driving force generated by the coastal jet, resulting in the onshore-released upwelling front and onshore-shifted boundary of cross-shore transport near the bottom. Due to the weakened coastal jet, the enhanced cross-shore wind stress over the inshore region is rarely offset by the pressure gradient near the surface and thereby allowed to balance with the Coriolis force, leading the alongshore Ekman transport. Although the geostrophic flow forced by the coastal jet is reduced, the southward current near the surface is compensated by the Ekman transport forced by the cross-shore wind component.

CHAPTER 8.

CONCLUSION

Although we have relied mostly on the natural gas and fossil fuels, using renewable energy sources is a growing trend among the world. Ocean surface wave power is considered a tremendous potential source with limited environmental impact and high energy density. The previous research has centered on the total wave energy potential or temporal distributions and variability of the total wave energy potential focusing mainly on regional characterizations with a limited location. Due to the specific aspects of WEC technologies, e.g., frequency dependence, directionality, and temporal variability (capacity factor), the wave energy resource should be resolved based on the regional wave climates. Comprehensive data on the various attributes of the theoretical wave energy, and of sufficient quality, is not broadly available to fully inform the development of WEC technologies. In order to reduce this data gap to support greater opportunities of wave power and WEC technologies into the US energy markets, the wave energy resource within US coastal waters is assessed, characterized, and classified based on the wave energy potential using spectral partitioned data generated from a 30-year WaveWatch III spectral wave model hindcast. Unique contributions of the wave energy research include:

- Quantified annual available energy (AAE) along the US coastal waters in terms of the peak period, direction, month, and year
- Proposed new attribute parameters for characterizing the wave energy resource, e.g., AAE-weighted period, AAE spectral width, directionality coefficient,

direction of maximum directionally resolved AAE, seasonal and inter-annual variability

- Delineated eleven wave energy regions for the US coastal waters based on the wave energy resource parameters
- Assessed and characterized regional wave energy resource by providing marginal and joint distributions of AAE and corresponding resource parameters, and identified energetic wave systems for each region
- Developed two classification systems based on wave power and the dominant peak period band classes, one based on the total wave power and the other based on the partitioned wave power in the dominant peak period band, and classified the wave energy along the US coastal waters

The advantage of using the partition data instead of the complete wave spectrum is that the spectral partitioned data isolates and defines a particular wave train within an irregular wave field, thereby better resolves the frequency and directional dependence of the wave energy resource. The resource metrics used in this study facilitate regional energy planning, WEC project development, and WEC design by reducing data needs and providing a more comprehensive characterization and assessment of opportunities and constraints for energy generation than AAE alone. Regions and sites where the energy is concentrated within a dominant period band and directional bandwidth can be distinguished from those where the energy is spread more broadly. Regions and sites that exhibit a more constant and reliable resource can be distinguished from those with significant temporal variability. Depending on the particular technology, developers can use the relevant characterization parameters to help with siting and feasibility assessments.

In addition, the WEC technology developers benefit from knowing the range of conditions that potentially exist such that they can target the technology to work most efficiently under those conditions. The classification systems provide key resource attributes that are relevant for the design and operation of WEC technologies, e.g., the operating period bandwidth that links a WEC technology design performance parameter with the period band representing a population of waves at each site. It also establishes a framework for investigating the feasibility of a compatible wave conditions and technology classification system to reduce design and manufacturing costs.

The coastal circulation plays critical roles in coastal ecosystems by influencing the transport of heat, sediment, entrained gases, nutrients, pollutants, and biota. Therefore, characteristics of the circulation pattern and forcing mechanisms influencing the circulation should be understood. The complexity of coastal circulation has been recognized due to the interaction between winds, submesoscale eddies, currents, mixing and surfzone processes near the inner shelf. The circulation during coastal upwelling near Pt. Sal is considered complex not only due to a confluence of distinct alongshore currents but also the complex bathymetry and coastline. In the presence of the strong alongshore currents over the along-shelf varying topography, the circulation significantly varies over the along-shelf thus requires three-dimensional analysis. Numerical simulations are performed to understand the three-dimensional circulation during coastal upwelling conditions near Pt. Sal, CA. Unique contributions of the coastal circulation research include:

- Performed a multi nested grid simulation using the Regional Ocean Model (ROMS) for June-July 2015 and June-September 2017.

- Detected upwelling circulation events by comparing two model results (with winds and without winds), one during June 2015 and the other one during July 2017.
- Characterized and compared circulation patterns of two events, e.g., divergence of upwelling transports near bottom, upwelling front and convergence, divergence surface current near Pt. Sal, using Lagrangian tracks.
- Diagnosed the forcing mechanisms influencing the circulation, e.g., alongshore / cross-shore wind, alongshore currents, coastline promontory, using the momentum balance, and identified the dominant forcing mechanisms at different locations.

This study establishes a framework for understanding the coastal circulations using numerical simulations, which can provide one of the guidelines for detecting the coastal upwelling, characterizing the circulation patterns, and identifying the forcing mechanisms for the circulation by linking the Lagrangian transport and Eulerian momentum diagnostics. Although the coastal circulation study focuses on two circulation events during upwelling favorable conditions, the similarities and differences in the circulation patterns and forcing mechanisms of the two cases are successfully described. This framework is applicable to other conditions as well as other locations and can contribute to classifying the circulation patterns in terms of the combinations of forcing mechanisms.

The classification systems and regional opportunities and constraints for wave energy generation discussed in this study are based on the theoretical resource. Other factors to consider include market size, local cost of energy, proximity to demand centers, the energy price (an estimation of avoided energy cost in the market), distance to transmission, and shipping costs [134]. The wave energy characteristics described in this study maintain no inherent assumptions based on any specific WEC archetype and, therefore, is considered to be archetype agnostic. Because the wave conditions largely influence the operation or survival of the technology, characterizing risks to energy generations based on extreme wave conditions is also important [135]. The long-term trends of the wave energy resource attribute, e.g., the long-term trend of the wave energy within a particular period, direction, and season, slope of the spectral width and directionality coefficient, is also important for planning the wave energy projects. In addition, the wave energy resource attributes developed in this study are based on wave climate statistics generated entirely from deep and intermediate wave conditions. Future investigations will extend this work with wave climate statistics generated from shallow nearshore sites. Since the WWIII wind-wave models could not compute the complicated wave interactions for near-shore sites, SWAN modeling is an option for the wave energy resource analysis at the shallow water sites.

The ROMS simulation performed in this study does not include the tide forcing. Because the tide affects curents and sea level variations, a comparison with the circulation patterns including tide forcing can be used to explain the effects of the tide on the coastal circulation. Similarly, a two-way coupled SWAN/ROMS model would help to analyze the effects of waves on the circulation. This would include the large wave driven currents originating within the surf zone and their dynamical interactions with the inner shelf flow field.

In addition, the two-way coupling model can be used to examine the effects of currents on the large scale wave energy resource. Although waves refract to be more shore-normal as they propogate over decreasing water depth towards the shore, the wave direction is often quite variable as shown in the regional wave energy resource characteristics (e.g. the along-shelf directed waves contains comparable energy in the Atlantic ocean coast). Therefore, the effects of strong along-shelf currents on the wave energy resource analysis are not negligible and could be addressed in a future study.

APPENDIX A.

CONVERSION FACTORS FOR WAVE ENERGY CALCULATION

The Pierson-Moskowitz spectrum for wind-sea and Gaussian spectrum for swell are used to compute the conversion factors between energy period and peak period. The conversion factors are derived from calculating the energy period which is defined in terms of two spectral moments, m_{-1} and m_0

$$T_e = \frac{m_{-1}}{m_0} \tag{A.1}$$

$$m_{-1} = \int_0^\infty S(f) f^{-1} df \tag{A.2}$$

$$m_0 = \int_0^\infty S(f) df = H^2/16 \tag{A.3}$$

where H is the significant wave height and $S(f)$ is wave spectrum in terms of the frequency. The Pierson-Moskowitz spectrum defined in terms of the partition wave height and peak period is of the form:

$$S_{pm}(f) = \frac{5}{16} H^2 f_p^4 f^{-5} exp^{-1.25\left(\frac{f_p}{f}\right)^4} \tag{A.4}$$

where fp is the peak frequency which is the reciprocal of the peak period. Plugging the form of Pierson-Moskowitz spectrum into Eq. (A.2) gives following expression

$$m_{-1} = \frac{H^2 f_p^{-1}}{16}\left[\frac{1.25^{3/4}\Gamma(0.25)}{5}\right] \tag{A.5}$$

where Γ is the gamma function. Finally, the conversion factor for the wind-sea partitions is estimated as

$$T_e = \frac{m_{-1}}{m_0} = \left[\frac{1.25^{3/4}\Gamma(0.25)}{5}\right] f_p^{-1} = 0.858\, T_p \tag{A.6}$$

This conversion factor C=0.858 is identical to $\alpha = 0.86$ which is generally used for the Pierson-Moskowitz spectrum [14].

The Gaussian spectrum is also defined in terms of partition wave height and peak period as

$$S(f) = \frac{H^2}{16\sigma\sqrt{2\pi}} exp^{-\frac{(f-f_p)^2}{2\sigma^2}} \tag{A.7}$$

where σ is the standard deviation. Plugging the form of Gaussian into Eq. (A.2) gives following expression.

$$m_{-1} = \int_0^\infty f^{-1} \frac{H^2}{16\sigma\sqrt{2\pi}} exp^{-\frac{(f-f_p)^2}{2\sigma^2}} df \tag{A.8}$$

Unfortunately, Gaussian integral with negative power is known as non-integrable. To eliminate the Gaussian integral with negative power, $S_g(f)$, a new Gaussian function of $S(f)f^{-1}$ having a peak frequency of $S(f)f^{-1}$ is proposed as

$$S_g(f) = \alpha\, exp^{-\frac{(f-g_p)^2}{2\sigma_g^2}} \tag{A.9}$$

Eq. (A.9) is a general form of the Gaussian function where g_p is the peak frequency of $S_g(f)$ which can be estimated by the derivative of $S(f)f^{-1}$ as

$$g_p = \frac{f_p + \sqrt{f_p^2 - 4\sigma^2}}{2} \tag{A.10}$$

where α is the peak of the spectrum which is estimated by plugging g_p into $S(f)f^{-1}$ as

$$\alpha = \frac{1}{g_p}\frac{H^2}{16\sigma\sqrt{2\pi}}e^{-\frac{(g_p-f_p)^2}{2\sigma^2}} \tag{A.11}$$

where σ_g is the standard deviation of $S_g(f)$ which is calibrated by the following relation,

$$S_g(f) = S(f)f^{-1} \qquad at \qquad f = g_p - \sigma \tag{A.12}$$

$$\sigma_g = \left[1 + 2\ln\left(\frac{g_p - \sigma}{g_p}\right) + 2\frac{(f_p - g_p)}{\sigma}\right]^{-0.5} \sigma \tag{A.13}$$

It gives

$$S_g(f) = \frac{1}{g_p}\frac{H^2}{16\sigma\sqrt{2\pi}}e^{-\frac{(g_p-f_p)^2}{2\sigma^2}}e^{-\frac{(f-g_p)^2}{2\sigma_g^2}} \tag{A.14}$$

To validate the $S_g(f)$ function, the shape of $S_g(f)$ is compared to $S(f)f^{-1}$ function in Figure A. 1. As demonstrated in Figure A. 1, $S_g(f)$ can be used without noticeable error.

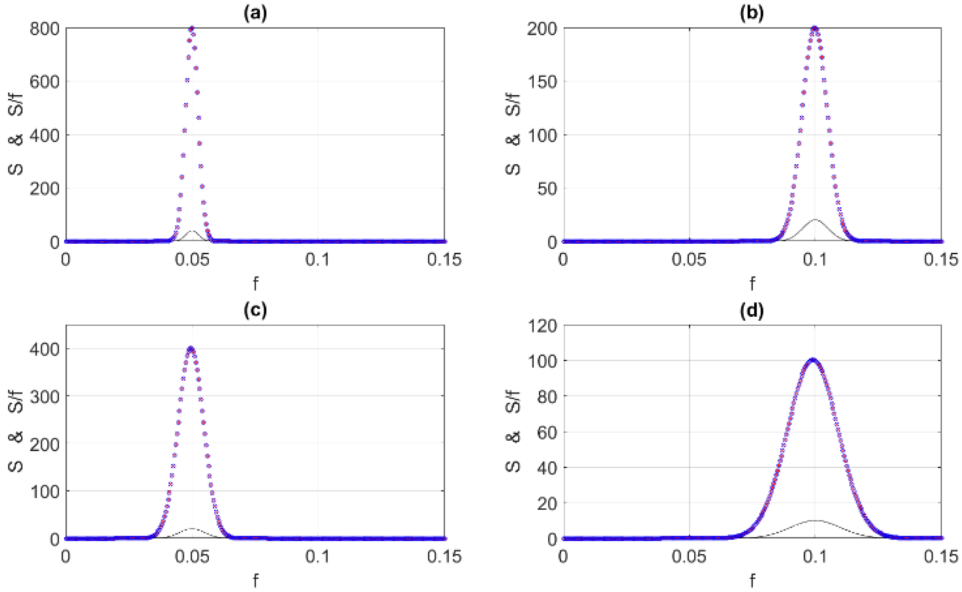

Figure A. 1. Scatter plots of Gaussian spectrum having a significant wave height of 2.0m. Black line represents *S(f)*, red dot represents $\boldsymbol{S(f)f^{-1}}$ and blue dot indicates $\boldsymbol{S_g(f)}$ in terms of frequency: (a) $\boldsymbol{f_p}$ = 0.05(Hz) and $\boldsymbol{\sigma}$ = 0.0025(Hz), (b) $\boldsymbol{f_p}$ = 0.1 and $\boldsymbol{\sigma}$ = 0.0025, (c) $\boldsymbol{f_p}$ = 0.05 and $\boldsymbol{\sigma}$ = 0.005, (d) $\boldsymbol{f_p}$ = 0.1 and $\boldsymbol{\sigma}$ = 0.005.

Plugging the $S_g(f)$ function into Eq. (A.1) and (A.2) gives following expression:

$$m_{-1} = \frac{1}{g_p}\frac{H^2}{16\sigma}\sigma_g e^{-\frac{(g_p-f_p)^2}{2\sigma^2}} \tag{A.15}$$

$$T_e = \frac{m_{-1}}{m_0} = \frac{1}{g_p\sigma}\sigma_g e^{-\frac{\left(g_p-f_p\right)^2}{2\sigma^2}} \tag{A.16}$$

Plugging Eq. (A.10), (A.11) and (A.13) into Eq. (A.16) gives the conversion factor for the swell partitions as a function of spectral width, ν as

$$\begin{aligned} T_e = \frac{2exp^{\frac{-1+2\nu^2+\sqrt{1-4\nu^2}}{4\nu^2}}}{1+\sqrt{1-4\nu^2}}\Bigg[1+2ln\left(\frac{1-2\nu+\sqrt{1-4\nu^2}}{1+\sqrt{1-4\nu^2}}\right) \\ +\frac{1-\sqrt{1-4\nu^2}}{\nu}\Bigg]^{-0.5} T_p \end{aligned} \tag{A.17}$$

The spectral width (ν), standard deviation (σ) and peak period (f_p) are related through the following equation.

$$\nu = \sqrt{\frac{m_0 m_2}{{m_1}^2}-1} = \frac{\sigma}{f_p} \tag{A.18}$$

To simplify the conversion factor, the spectral width is restricted by the following physical property of wave moment.

$$\int_{-\infty}^{\infty} S(f)df = \int_{0}^{\infty} S(f)df \tag{A.19}$$

This restriction gives

$$erf\left(\frac{\sqrt{2}f_p}{2\sigma}\right) = 1, \quad \frac{\sigma}{f_p} = \nu \leq 0.25 \tag{A.20}$$

where erf is Gauss error function. Finally, the conversion factor simplified by the restriction is

$$1 \leq C(\nu) \leq 1.083 \tag{A.21}$$

For validation of the conversion factors, the energy period estimated from the conversion factors is compared to the results of complete directional spectra at 125 locations where the partitioned data and complete wave spectra are both available.

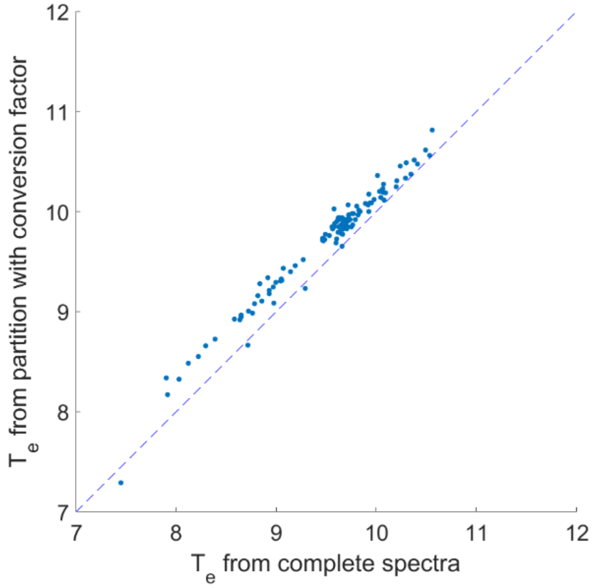

Figure A. 2. Comparison of $\boldsymbol{T_e}$ computed from complete directional spectra and $\boldsymbol{T_e}$ estimated from spectral partitioned data using the conversion factors at 125 locations. The dots represent the mean $\boldsymbol{T_e}$ for the hindcasted time period.

As shown in Figure A. 2, the T_e estimated from the conversion factor tend to overestimate the results of the complete directional spectrum on the order of 2%. Therefore, to minimize the error, the Pierson-Moskowitz spectrum is used instead of the JONSWAP spectrum because the peak enhancement of the JONSWAP spectrum results in longer energy periods. In a similar fashion, the conversion factor 1.0 for swell partition is used in order to minimize the overestimates.

REFERENCES

[1] R. Alamian, R. Shafaghat, M. Safdari, and R. Bayani, “An empirical evaluation of the sea depth e ff ects for various wave characteristics on the performance of a point absorber wave energy converter,” *Ocean Eng.*, vol. 137, no. August 2015, pp. 13–21, 2017.

[2] D. Hand, M.M.; Baldwin, S.; DeMeo, E.; Reilly, J.M.; Mai, T.; Arent, D.; Porro, G.; Meshek, M.; Sandor, “Renewable Electricity Futures Study.”

[3] IEC, “International Standard, Marine energy – Wave, tidal and other water current converters – Part 101: Wave energy resource assessment and characterization, IEC 62600-101: Edition 1.0,” 2015.

[4] Department of Energy (DOE), “Quadrennial Technology Review 2015, Chapter 4: Advancing Clean Electric Power Technologies, Technology Assessments,” 2015.

[5] *An Evaluation of the U.S. Department of Energy’s Marine and Hydrokinetic Resource Assessments*. National Academies Press, Washington, D.C., 2013.

[6] C. J., *Ocean wave energy: current status and future perspectives. Green Energy and Technology.* Springer: Berlin., 2008.

[7] A. R. Dallman and V. S. Neary, “Characterization of U . S . Wave Energy Converter (WEC) Test Sites : A Catalogue of Met-Ocean Data 2nd Edition,” no. September, 2015.

[8] U. A. Korde, “Efficient primary energy conversion in irregular waves,” *Ocean Eng.*, vol. 26, no. 7, pp. 625–651, Jul. 1999.

[9] A. Chawla, D. M. Spindler, and H. L. Tolman, “Validation of a thirty year wave hindcast using the Climate Forecast System Reanalysis winds,” *Ocean Model.*, vol. 70, pp. 189–206, Oct. 2013.

[10] G. Chang, C. A. Jones, J. D. Roberts, and V. S. Neary, “A comprehensive evaluation of factors affecting the levelized cost of wave energy conversion projects,” *Renew. Energy*, vol. 127, pp. 344–354, 2018.

[11] IEC, "International Standard: Wind turbines – Part 1: Design Requirements, IEC 61400-1:2500(E)," 2014.

[12] B. Drew, A. R. Plummer, and M. N. Sahinkaya, "A review of wave energy converter technology," *Proc. Inst. Mech. Eng. Part A J. Power Energy*, vol. 223, no. 8, pp. 887–902, Dec. 2009.

[13] R. W. Garvine, "The vertical structure and subtidal dynamics of the inner shelf off New Jersey," pp. 337–371, 2004.

[14] S. J. Lentz and M. R. Fewings, "The Wind- and Wave-Driven Inner-Shelf Circulation," *Ann. Rev. Mar. Sci.*, vol. 4, no. 1, pp. 317–343, 2012.

[15] K. H. Brink, "Cross-Shelf Exchange," *Ann. Rev. Mar. Sci.*, vol. 8, no. 1, pp. 59–78, 2016.

[16] V. Ekman, "On the influence of the earth's rotation on ocean currents.," *Ark. Mat. Astron. Fys.*, vol. 2, pp. 1–53, 1905.

[17] J. A. Austin and S. J. Lentz, "The Inner Shelf Response to Wind-Driven Upwelling and Downwelling*," *J. Phys. Oceanogr.*, vol. 32, no. 7, pp. 2171–2193, 2002.

[18] S. H. Suanda, N. Kumar, A. J. Miller, E. Di Lorenzo, K. A. Haas, D. Cai, C. A. Edwards, L. Washburn, M. R. Fewings, R. Torres, and F. Feddersen, "Wind relaxation and a coastal buoyant plume north of Pt. Conception, CA: Observations, simulations, and scalings," *J. Geophys. Res. Ocean.*, vol. 121, no. 10, pp. 7455–7475, 2016.

[19] F. Feddersen, J. Barth, J. Calantoni, C. Chickadel, J. Colosi, and E. Di Lorenzo, *October 2016 Applied Physics Laboratory University of Washington*. 2016.

[20] J. Gan and J. S. Allen, "A modeling study of shelf circulation off northern California in the region of the Coastal Ocean Dynamics Experiment : Response to relaxation of upwelling winds," *J. Geophys. Res.*, vol. 107, pp. 1–31, 2002.

[21] M. Roughan, E. J. Terrill, J. L. Largier, and M. P. Otero, "Observations of divergence and upwelling around Point Loma , California," vol. 110, no. August 2004, pp. 1–11, 2005.

[22] R. L. Wiegel, *Oceanographical Engineering. Englewood Cliffs, N.J.: Prentice-Hall*. 1964.

[23] Y. Fan, S.-J. Lin, I. M. Held, Z. Yu, and H. L. Tolman, "Global Ocean Surface Wave Simulation Using a Coupled Atmosphere-Wave Model," *J. Clim.*, vol. 25, no. 18, pp. 6233–6252, Sep. 2012.

[24] I. R. Young, S. Zieger, and A. V. Babanin, "Global Trends in Wind Speed and Wave Height," *Science (80-.).*, vol. 332, no. 6028, pp. 451–455, Apr. 2011.

[25] E. P. R. I. (EPRI), "Mapping and Assessment of the United States Ocean Wave Energy Resource, EPRI 2011 Technical Report to U.S. Department of Energy," 2011.

[26] A. R. Dallman and V. S. Neary, "Characterization of U.S. Wave Energy Converter (WEC) Test Sites: A Catalogue of Met-Ocean Data," Albuquerque, NM, and Livermore, CA (United States), Oct. 2014.

[27] A. Cornett, "A global wave energy resource assessment," in *International Offshore and Polar Engineering Conference*, 2008, vol. ISOPE-2008.

[28] R. A. Arinaga and K. F. Cheung, "Atlas of global wave energy from 10 years of reanalysis and hindcast data," *Renew. Energy*, vol. 39, no. 1, pp. 49–64, Mar. 2012.

[29] K. Gunn and C. Stock-Williams, "Quantifying the global wave power resource," *Renew. Energy*, vol. 44, pp. 296–304, Aug. 2012.

[30] *An Evaluation of the U.S. Department of Energy's Marine and Hydrokinetic Resource Assessments*. Washington, D.C.: National Academies Press, 2013.

[31] Department of Energy (DOE), "Quadrennial Technology Review 2015, Chapter 4: Advancing Clean Electric Power Technologies, Technology Assessments.," 2015.

[32] J. H. Wilson and A. Beyene, "California Wave Energy Resource Evaluation," *J. Coast. Res.*, vol. 233, pp. 679–690, May 2007.

[33] A. BEYENE and J. WILSON, "Comparison of wave energy flux for northern, central, and southern coast of California based on long-term statistical wave data,"

Energy, vol. 31, no. 12, pp. 1856–1869, Sep. 2006.

[34] A. Beyene and J. H. Wilson, “Digital mapping of California wave energy resource,” *Int. J. Energy Res.*, vol. 31, no. 12, pp. 1156–1168, Oct. 2007.

[35] G. Hagerman, R. Bedard, M. Previsic, Electric Power Research Institute, and Electricity Innovation Institute, “Survey and characterization of potential offshore wave energy sites in Oregon,” 2004.

[36] G. Hagerman, R. Bedard, M. Previsic, Electric Power Research Institute, and Electricity Innovation Institute, “Survey and characterization of potential offshore wave energy sites in Washington,” 2004.

[37] G. García-Medina, H. T. Özkan-Haller, and P. Ruggiero, “Wave resource assessment in Oregon and southwest Washington, USA,” *Renew. Energy*, vol. 64, pp. 203–214, Apr. 2014.

[38] J. E. Stopa, K. F. Cheung, and Y.-L. Chen, “Assessment of wave energy resources in Hawaii,” *Renew. Energy*, vol. 36, no. 2, pp. 554–567, Feb. 2011.

[39] J. E. Stopa, J.-F. Filipot, N. Li, K. F. Cheung, Y.-L. Chen, and L. Vega, “Wave energy resources along the Hawaiian Island chain,” *Renew. Energy*, vol. 55, pp. 305–321, Jul. 2013.

[40] Z. Defne, K. A. Haas, and H. M. Fritz, “Wave power potential along the Atlantic coast of the southeastern USA,” *Renew. Energy*, vol. 34, no. 10, pp. 2197–2205, Oct. 2009.

[41] H. L. Tolman, “User manual and system documentation of WAVEWATCH-III version 3.14,” 2009.

[42] G. Hagerman, “Southern New England Wave Energy Resource Potential,” in *Building Energy 2001*, 2001.

[43] O. Yaakob, F. Ellyza, K. Mohd, A. Hassan, and K. King, “Satellite-based wave data and wave energy resource assessment for South China Sea,” *Renew. Energy*, vol. 88, pp. 359–371, 2016.

[44] D. Gonz, “Wave energy resource assessment in Menorca (Spain),” *Renew. Energy*, vol. 71, pp. 51–60, 2014.

[45] M. Gonçalves, P. Martinho, and C. G. Soares, “Assessment of wave energy in the Canary Islands,” *Renew. Energy*, vol. 68, pp. 774–784, 2014.

[46] J. Pastor and Y. Liu, “Wave Climate Resource Analysis Based on a Revised Gamma Spectrum for Wave Energy Conversion Technology,” *Sustainability*, vol. 8, pp. 1321–1334, 2016.

[47] M. Mestres and R. Jebbad, “Wave energy potential along the Atlantic coast of Morocco,” *Renew. Energy*, vol. 96, pp. 20–32, 2016.

[48] J. Pastor and Y. Liu, “Wave Energy Resource Analysis for Use in Wave Energy Conversion,” *J. Offshore Mech. Arct. Eng.*, vol. 137, no. February, pp. 1–9, 2015.

[49] P. Lenee-bluhm, R. Paasch, and H. T. Özkan-haller, “Characterizing the wave energy resource of the US Paci fi c Northwest,” vol. 36, 2011.

[50] B. G. Reguero, I. J. Losada, and F. J. Méndez, “A global wave power resource and its seasonal , interannual and long-term variability,” vol. 148, pp. 366–380, 2015.

[51] S. G. Jacobson PT, Hagerman G, “Mapping and assessment of the United States ocean wave energy resource. EPRI 2011 Technical Report to U.S. Department of Energy,” 2011.

[52] M. Lehmann, F. Karimpour, A. Goudey, and P. T. Jacobson, “Ocean wave energy in the United States : Current status and future perspectives,” vol. 74, no. February 2016, pp. 1300–1313, 2017.

[53] R. K. Linsley, J. B. Franzini, D. L. Freyberg, and G. Tchobanoglous, *Water Resources Engineering*. McGraw-Hill Publishing Co., London., 1992.

[54] J. Cruz, “WEC Classes : Preliminary Studies,” *Proc. 11th Eur. Wave Tidal Energy Conf.*, pp. 1–8, 2015.

[55] A. Huyer, “Coastal Upwelling in the California Current System,” vol. 12, pp. 259–284, 1983.

[56] P. T. Strub and C. James, “The large-scale summer circulation of the California current,” vol. 22, no. 3, pp. 207–210, 1995.

[57] S. D. Pierce, R. L. Smith, P. M. Kosro, J. A. Barth, and C. D. Wilson, “Continuity of the poleward undercurrent along the eastern boundary of the mid-latitude north Paci " c,” vol. 47, pp. 811–829, 2000.

[58] J. A. Barth, S. D. Pierce, and R. L. Smith, “A separating coastal upwelling jet at Cape Blanco , Oregon and its connection to the California Current System,” vol. 47, pp. 783–810, 2000.

[59] R. M. Castelao and H. Luo, “Upwelling jet separation in the California Current System,” *Sci. Rep.*, no. August, pp. 1–8, 2018.

[60] C. B. Woodson, L. Washburn, J. A. Barth, D. J. Hoover, A. R. Kirincich, M. A. Mcmanus, J. P. Ryan, and J. Tyburczy, “Northern Monterey Bay upwelling shadow front : Observations of a coastally and surface-trapped buoyant plume,” vol. 114, pp. 1–15, 2009.

[61] R. K. Walter, M. Stastna, C. B. Woodson, and S. G. Monismith, “Observations of nonlinear internal waves at a persistent coastal upwelling front,” *Cont. Shelf Res.*, vol. 117, pp. 100–117, 2016.

[62] R. K. Walter, K. J. Armenta, B. Shearer, I. Robbins, and J. Steinbeck, “Coastal upwelling seasonality and variability of temperature and chlorophyll in a small coastal embayment,” *Cont. Shelf Res.*, vol. 154, no. May 2017, pp. 9–18, 2018.

[63] S. J. Lentz, “The Influence of Stratification on the Wind-Driven Cross-Shelf Circulation over the North Carolina Shelf*,” *J. Phys. Oceanogr.*, vol. 31, no. 9, pp. 2749–2760, 2001.

[64] A. R. Kirincich, J. A. Barth, B. A. Grantham, B. A. Menge, and J. Lubchenco, “Wind-driven inner-shelf circulation off central Oregon during summer,” *J. Geophys. Res. C Ocean.*, vol. 110, no. 10, pp. 1–17, 2005.

[65] C. E. Tilburg, “Across-Shelf Transport on a Continental Shelf: Do Across-Shelf Winds Matter?,” *J. Phys. Oceanogr.*, vol. 33, no. 12, pp. 2675–2688, 2003.

[66] Z. Li and R. H. Weisberg, “West Florida continental shelf response to upwelling

favorable wind forcing," *J. Geophys. Res.*, vol. 104, p. 23,427-23,442, 1999.

[67] M. Fewings, S. J. Lentz, and J. Fredericks, "Observations of Cross-Shelf Flow Driven by Cross-Shelf Winds on the Inner Continental Shelf," *J. Phys. Oceanogr.*, vol. 38, no. 11, pp. 2358–2378, 2008.

[68] P. S. Gay and T. K. Chereskin, "Mean structure and seasonal variability of the poleward undercurrent off southern California," *J. Geophys. Res.*, vol. 114, pp. 1–17, 2009.

[69] J. M. Huthnance, "Slope currents and ''JEBAR.pdf," *J. Phys. Oceanogr.*, vol. 14, pp. 795–810, 1984.

[70] M. J. P. and L. M. James, "A linear stratified ocean model of the coastal undercurrent," *Philos. Trans. R. Soc. London. Ser. A, Math. Phys. Sci.*, vol. 302, pp. 385–413, 1981.

[71] A. Apotsos, B. Raubenheimer, S. Elgar, and R. T. Guza, "Wave-driven setup and alongshore flows observed onshore of a submarine canyon," *J. Geophys. Res. Ocean.*, vol. 113, no. 7, pp. 1–9, 2008.

[72] J. W. Long and H. T. Özkan-Haller, "Offshore controls on nearshore rip currents," *J. Geophys. Res. Ocean.*, vol. 110, no. 12, pp. 1–21, 2005.

[73] J. E. Hansen, T. T. Janssen, B. Raubenheimer, F. Shi, P. L. Barnard, and I. S. Jones, "Observations of surfzone alongshore pressure gradients onshore of an ebb-tidal delta," *Coast. Eng.*, vol. 91, pp. 251–260, 2014.

[74] P. B. Smit, T. T. Janssen, and T. H. C. Herbers, "Stochastic modeling of coherent wave fields over variable depth," *J. Phys. Oceanogr.*, vol. 45, no. 4, pp. 1139–1154, 2015.

[75] K. Hasselmann, T. P. Barnett, E. Bouws, H. Carlson, D. E. Cartwright, K. Enke, J. A. Ewing, H. Gienapp, D. E. Hasselmann, P. Kruseman, A. Meerburg, P. Müller, D. J. Olbers, K. Richter, W. Sell, and H. Walden, "Measurements of wind-wave growth and swell decay during the Joint North Sea Wave Project (JONSWAP), Ergänzungsheft 13, No. A," 1973.

[76] Z. Xu and A. J. Bowen, "Wave- and Wind-Driven Flow in Water of Finite Depth,"

Journal of Physical Oceanography, vol. 24, no. 9. pp. 1850–1866, 1994.

[77] N. Kumar, G. Voulgaris, J. C. Warner, and M. Olabarrieta, “Implementation of the vortex force formalism in the coupled ocean-atmosphere-wave-sediment transport (COAWST) modeling system for inner shelf and surf zone applications,” *Ocean Model.*, vol. 47, pp. 65–95, 2012.

[78] A. R. Kirincich and J. A. Barth, “Alongshelf Variability of Inner-Shelf Circulation along the Central Oregon Coast during Summer,” *J. Phys. Oceanogr.*, vol. 39, no. 6, pp. 1380–1398, 2009.

[79] Q. Zou, A. J. Bowen, and A. E. Hay, “Vertical distribution of wave shear stress in variable water depth: Theory and field observations,” *J. Geophys. Res. Ocean.*, vol. 111, no. 9, pp. 1–17, 2006.

[80] Y. Uchiyama, J. C. McWilliams, and A. F. Shchepetkin, “Wave-current interaction in an oceanic circulation model with a vortex-force formalism: Application to the surf zone,” *Ocean Model.*, vol. 34, no. 1–2, pp. 16–35, 2010.

[81] X. J. Capet, P. Marchesiello, and J. C. Mcwilliams, “Upwelling response to coastal wind profiles,” vol. 31, no. May, pp. 1–4, 2004.

[82] M. G. Reyes and J. Largier, “Observations of increased wind - driven coastal upwelling off central California,” vol. 115, pp. 1–8, 2010.

[83] J. S. Allen, “MODELS OF WIND-DRIVEN CURRENTS ON THE CONTINENTAL SHELF,” *Annu. Rev. Fluid Mech.*, vol. 12, pp. 389–433, 1980.

[84] S. Saha, S. Moorthi, H. L. Pan, X. Wu, J. Wang, S. Nadiga, P. Tripp, R. Kistler, J. Woollen, D. Behringer, H. Liu, D. Stokes, R. Grumbine, G. Gayno, J. Wang, Y. T. Hou, H. Y. Chuang, H. M. H. Juang, J. Sela, M. Iredell, R. Treadon, D. Kleist, P. Van Delst, D. Keyser, J. Derber, M. Ek, J. Meng, H. Wei, R. Yang, S. Lord, H. Van Den Dool, A. Kumar, W. Wang, C. Long, M. Chelliah, Y. Xue, B. Huang, J. K. Schemm, W. Ebisuzaki, R. Lin, P. Xie, M. Chen, S. Zhou, W. Higgins, C. Z. Zou, Q. Liu, Y. Chen, Y. Han, L. Cucurull, R. W. Reynolds, G. Rutledge, and M. Goldberg, “The NCEP climate forecast system reanalysis,” *Bull. Am. Meteorol. Soc.*, vol. 91, no. 8, pp. 1015–1057, 2010.

[85] “WAVEWATCH III® Model,” *National Oceanic and Atmospheric Administration*. [Online]. Available: http://polar.ncep.noaa.gov/waves/wavewatch/.

[86] “WAVEWATCH III® Hindcast and Reanalysis Archives,” *National Oceanic and Atmospheric Administration*. [Online]. Available: http://polar.ncep.noaa.gov/waves/hindcasts/.

[87] L. Vincent and P. Soille, “Watersheds in digital spaces: an efficient algorithm based on immersion simulations,” *IEEE Trans. Pattern Anal. Mach. Intell.*, vol. 13, no. 6, pp. 583–598, Jun. 1991.

[88] J. L. Hanson and R. E. Jensen, “Wave system diagnostics for numerical wave models,” in *International Workshop on Wave Hindcasting and Forecasting*, 2004.

[89] J. L. Hanson and O. M. Phillips, “Automated Analysis of Ocean Surface Directional Wave Spectra,” *J. Atmos. Ocean. Technol.*, vol. 18, no. 2, pp. 277–293, Feb. 2001.

[90] D. N. Veritas, “Environmental conditions and environmental loads - The Pierson-Moskowize and JONSWAP spectra,” *Dnv*, no. October, pp. 33–39, 2010.

[91] S. Ahn, K. A. Haas, and V. S. Neary, “Wave energy resource classification system for US coastal waters,” *Renew. Sustain. Energy Rev.*, vol. 104, pp. 54–68, 2019.

[92] G. R. Miller, *Pacific Northwest Weather: But My Barometer Says Fair!* Frank Amato, 2002.

[93] M. Previsic and J. Epler, “The Future Potential of Wave Power in the United States,” 2012.

[94] B. G. Reguero, I. J. Losada, and F. J. Méndez, “A recent increase in global wave power as a consequence of oceanic warming,” *Nat. Commun.*, no. 10, pp. 1–14, 2019.

[95] H. J. Niebauer, “Effects of E1 Nino-Southern Oscillation and North Pacific Weather Patterns on Interannual Variability in the Subarctic Bering Sea,” vol. 93, pp. 5051–5068, 1988.

[96] A. J. Kennedy, M. L. Griffin, S. L. Morey, S. R. Smith, and J. J. O. Brien, “Effects of El Nin ˜ o – Southern Oscillation on sea level anomalies along the Gulf of Mexico coast,” vol. 112, pp. 1–16, 2007.

[97] D. S. Jenne, Y. Yu, and V. Neary, “Levelized Cost of Energy Analysis of Marine and Hydrokinetic Reference Models,” 2015.

[98] C. M. Risien and D. B. Chelton, “A Global Climatology of Surface Wind and Wind Stress Fields from Eight Years of,” no. 1989, pp. 2379–2413, 2008.

[99] Craig M. Risien, “The scatterometer Climatology of Ocean Winds (SCOW),” 2011. [Online]. Available: ftp://cioss.coas.oregonstate.edu/pub/scow/.

[100] L. Liberti, A. Carillo, and G. Sannino, “Wave energy resource assessment in the Mediterranean , the Italian perspective,” vol. 50, pp. 938–949, 2013.

[101] C. S. Nelson, “Wind Stress and Wind Stress Curl Over the California Current,” no. 1963, 1977.

[102] R. J. Lynn, “SEASONAL VARIATION OF TEMPERATURE AND SALINITY AT 10 METERS IN THE CALIFORNIA CURRENT,” 1965.

[103] A. F. Shchepetkin and J. C. Mcwilliams, “The regional oceanic modeling system (ROMS): oceanic model,” vol. 9, pp. 347–404, 2005.

[104] D. B. Haidvogel, H. Arango, W. P. Budgell, B. D. Cornuelle, E. Curchitser, E. Di Lorenzo, K. Fennel, W. R. Geyer, A. J. Hermann, L. Lanerolle, J. Levin, J. C. McWilliams, A. J. Miller, A. M. Moore, T. M. Powell, A. F. Shchepetkin, C. R. Sherwood, R. P. Signell, J. C. Warner, and J. Wilkin, “Ocean forecasting in terrain-following coordinates: Formulation and skill assessment of the Regional Ocean Modeling System,” *J. Comput. Phys.*, vol. 227, no. 7, pp. 3595–3624, 2008.

[105] A. F. Shchepetkin and J. C. McWilliams, “Correction and commentary for ‘Ocean forecasting in terrain-following coordinates: Formulation and skill assessment of the regional ocean modeling system’ by Haidvogel et al., J. Comp. Phys. 227, pp. 3595-3624,” *J. Comput. Phys.*, vol. 228, no. 24, pp. 8985–9000, 2009.

[106] J. C. Warner, B. Armstrong, R. He, and J. B. Zambon, “Development of a Coupled Ocean-Atmosphere-Wave-Sediment Transport (COAWST) Modeling System,” *Ocean Model.*, vol. 35, no. 3, pp. 230–244, 2010.

[107] E. Mason, J. Molemaker, A. F. Shchepetkin, F. Colas, J. C. Mcwilliams, and P. Sangrà, “Procedures for offline grid nesting in regional ocean models,” *Ocean*

Model., vol. 35, no. 1–2, pp. 1–15, 2010.

[108] D. C. Chapman, “Numerical treatment of cross-shelf open boundaries in a Barotropic Coastal Ocean Model,” *J. Phys. Oceanogr.*, vol. 15, pp. 1060–1075, 1985.

[109] P. Marchesiello, J. C. Mcwilliams, and A. Shchepetkin, “Open boundary conditions for long-term integration of regional oceanic models,” vol. 3, 2001.

[110] R. X. Hodur, J. Hong, J. Doyle, J. Pullen, P. M. Cummings, and M. A. Rennick, “The Coupled Ocean / Atmosphere Mesoscale Prediction System (COAMPS),” *Oceanography*, vol. 15, no. 1, pp. 88–98, 2002.

[111] N. Kumar, F. Feddersen, S. Suanda, Y. Uchiyama, and J. McWilliams, “Mid- to Inner-Shelf Coupled ROMS–SWAN Model–Data Comparison of Currents and Temperature: Diurnal and Semidiurnal Variability,” *J. Phys. Oceanogr.*, vol. 46, no. 3, pp. 841–862, 2016.

[112] C. E. Dorman and C. D. Winant, “The Structure and Variability of the Marine Atmosphere around the Santa Barbara Channel,” *Mon. Weather Rev.*, vol. 128, no. 2, pp. 261–282, 2000.

[113] C. D. Winant, E. P. Dever, and M. C. Hendershott, “Characteristic patterns of shelf circulation at the boundary between central and southern California,” vol. 108, no. Cc, 2003.

[114] C. Melton, L. Washburn, and C. Gotschalk, “Wind relaxations and poleward flow events in a coastal upwelling system on the central California coast,” vol. 114, pp. 1–18, 2009.

[115] J. A. COLOSI, N. KUMAR, S. H. SUANDA, T. M. FREISMUTH, and J. H. MACMAHAN, “Statistics of Internal Tide Bores and Internal Solitary Waves Observed on the Inner Continental Shelf off Point Sal , California,” *J. Phys. Oceanogr.*, vol. 48, pp. 123–143, 2018.

[116] R. M. Allen, J. A. Simeonov, J. Calantoni, M. T. Stacey, and E. A. Variano, “Turbulence in the presence of internal waves in the bottom boundary layer of the California inner shelf,” *Ocean Dyn.*, pp. 627–644, 2018.

[117] D. J. Mark, J. J. Westerink, E. A. Spargo, and R. A. Luettich, “ENPAC 2003 : A Tidal Constituent Database for Eastern North Pacific Ocean,” 2004.

[118] H. Yoon and H. Philander, “The Generation of Coastal Undercurrents,” *J. Oceanogr. Soc. Japan*, vol. 38, pp. 215–224, 1982.

[119] K. H. Brink, “Upwelling fronts : implications and unknowns,” vol. 7615, no. 1987, 2010.

[120] G. O. Marmorino, G. B. Smith, and W. D. Miller, “Infrared remote sensing of surf-zone eddies,” *IEEE J. Sel. Top. Appl. Earth Obs. Remote Sens.*, vol. 6, no. 3, pp. 1710–1718, 2013.

[121] E. L. Shroyer, J. N. Moum, and J. D. Nash, “Nonlinear internal waves over New Jersey’s continental shelf,” *J. Geophys. Res. Ocean.*, vol. 116, no. 3, pp. 1–16, 2011.

[122] R. K. Walter, C. Brock Woodson, R. S. Arthur, O. B. Fringer, and S. G. Monismith, “Nearshore internal bores and turbulent mixing in southern Monterey Bay,” *J. Geophys. Res. Ocean.*, vol. 117, no. 7, pp. 1–13, 2012.

[123] W. G. Zhang, G. G. Gawarkiewicz, D. J. McGillicuddy, and J. L. Wilkin, “Climatological Mean Circulation at the New England Shelf Break,” *J. Phys. Oceanogr.*, vol. 41, no. 10, pp. 1874–1893, 2011.

[124] J. A. Lerczak, “Observations of the semidiurnal internal tide on the southern California slope and shelf,” *J. Geophys. Res.*, vol. 108, no. C3, p. 3068, 2003.

[125] S. J. Lentz, M. Fewings, P. Howd, J. Fredericks, and K. Hathaway, “Observations and a Model of Undertow over the Inner Continental Shelf,” *J. Phys. Oceanogr.*, vol. 38, no. 11, pp. 2341–2357, 2008.

[126] J. Trowbridge and S. Elgar, “Turbulence Measurements in the Surf Zone*,” *J. Phys. Oceanogr.*, vol. 31, no. 8, pp. 2403–2417, 2001.

[127] F. Feddersen, J. H. Trowbridge, and A. J. Williams, “Vertical Structure of Dissipation in the Nearshore,” *J. Phys. Oceanogr.*, vol. 37, no. 7, pp. 1764–1777, 2007.

[128] F. Gómez-Valdivia, A. Parés-Sierra, and A. L. Flores-Morales, "Semiannual variability of the California Undercurrent along the Southern California Current System: A tropical generated phenomenon," *J. Geophys. Res. Ocean.*, pp. 1574–1589, 2017.

[129] T. P. CONNOLLY, B. M. HICKEY, I. SHULMAN, and R. E. THOMSON, "Coastal Trapped Waves , Alongshore Pressure Gradients , and the California Undercurrent," *J. Phys. Oceanogr.*, vol. 44, pp. 319–342, 2014.

[130] N. Kumar, G. Voulgaris, J. H. List, and J. C. Warner, "Alongshore momentum balance analysis on a cuspate foreland," vol. 118, no. October, pp. 5280–5295, 2013.

[131] C. D. WINANT, "Three-Dimensional Wind-Driven Coastal Circulation past a Headland," *J. Phys. Oceanogr.*, vol. 36, pp. 1430–1438, 2006.

[132] W. Hole and W. Hole, "Inner-Shelf Response to Cross-Shelf Wind Stress : The Importance of the Cross-Shelf Density Gradient in an Idealized Numerical Model and Field Observations," *J. Phys. Oceanogr.*, vol. 44, pp. 86–103, 2013.

[133] J. C. Warner, J. H. List, W. C. Schwab, G. Voulgaris, B. Armstrong, and N. Marshall, "Inner-shelf circulation and sediment dynamics on a series of shoreface-connected ridges offshore of Fire Island , NY," *Ocean Dyn.*, vol. 64, pp. 1767–1781, 2014.

[134] L. Kilcher and R. Thresher, "Marine Hydrokinetic Energy Site Identification and Ranking Methodology Part I : Wave Energy Marine Hydrokinetic Energy Site Identification and Ranking Methodology Part I : Wave Energy," 2016.

[135] V. S. Neary, R. G. Coe, J. Cruz, K. Haas, G. Bacelli, Y. Debruyne, and S. Ahn, "Classification Systems for Wave Energy Resources and WEC Technologies," *Int. Mar. Energy J.*, vol. 1, no. August 2017, pp. 71–79, 2018.